Federal University of São Carlos

Physics Graduate Program

Two-Dimensional Transition Metal Halides for Optical Applications: Impact of Excitons

Natan Moreira Regis

São Carlos - SP

2024

Federal University of São Carlos

Physics Graduate Program

Natan Moreira Regis

Two-Dimensional Transition Metal Halides for Optical Applications: Impact of Excitons

Dissertation presented to the Federal University of São Carlos as part of the requirements for obtaining the title of Master in Physics.

Advisor: Prof. Dr. Matheus Paes Lima

São Carlos - SP

2024

UNIVERSIDADE FEDERAL DE SÃO CARLOS

Centro de Ciências Exatas e de Tecnologia
Programa de Pós-Graduação em Física

Folha de Aprovação

Defesa de Dissertação de Mestrado do candidato Natan Moreira Regis, realizada em 01/08/2024.

Comissão Julgadora:

Prof. Dr. Matheus Paes Lima (UFSCar)

Profa. Dra. Vivian Vanessa França Henn (UNESP)

Prof. Dr. Celso Jorge Villas-Bôas (UFSCar)

O Relatório de Defesa assinado pelos membros da Comissão Julgadora encontra-se arquivado junto ao Programa de Pós-Graduação em Física.

Abstract

Two-dimensional materials have experienced rapid growth since the first exfoliation of graphene in 2004, which is an atomically thin sheet of carbon atoms exfoliated from graphite. Despite several unprecedented properties of graphene, induced by quantum confinement, it lacks a band gap that limits some optoelectronic applications. however, graphene motivates a new research field of two-dimensional materials, and their potential compositions and structures, ranging from insulators to semiconductors to conductors. The wide range of conductive behavior within the quantum confinement gives rise to distinct behaviors, including a large exciton binding energy. Excitons are quasi-particles formed by an electron-hole pair that interact through Coulomb attraction, a phenomenon present in semiconductors but more notable in low-dimensional materials due to quantum confinement, which changes the dielectric environment. However, single-particle theoretical methods, such as ground-state density functional theory, do not describe excitons because it is a many-body phenomenon. Thus, a complete characterization of the optical properties of two-dimensional materials requires going beyond a single-particle perspective. Motivated by the accomplishment of several two-dimensional materials and halide perovskites, this work explores a new class of two-dimensional materials, namely, transition metal halide (TMHs) monolayers. We initially selected potential TMHs for optoelectronics in the Computational 2D Materials Database (C2DB) and subsequently analyzed the structural, electronic, optical and excitonic properties using state-of-the-art theoretical methods to study materials such as Density Funcional Theory (DFT) calculations including relativistic and bandgap correction and the evaluation of optical properties including excitonic effect within Tight Binding (TB) Hamiltonian and by the solution of Bethe-Salpeter equation (BSE). Our calculations show that the equilibrium structure calculated by C2DB agrees with those obtained here and with other theoretical works. However, electronic properties exhibit important deviations that are not homogeneous among systems. For

instance, we observed deviations in the bandgap values up to 17 % when considering relativistic correction and for the corrected bandgap value computed applying the scissors operator methodology. We also computed optical and excitonic properties by solving the Bethe-Salpeter equations, showing isotropic and non-isotropic light absorption among the systems. The inclusion of excitonic effects decreased the maximum light absorption when compared to the absorption coefficient without these effects and also changes in the energy region of spectra. The compositions demonstrated considerable binding energy, highlighting the importance of studying this quasi-particle in theoretical calculations. The possible heterojunctions are hardly influenced by excitonic effects; thus, evaluating possible heterojunctions must take into account exctions. Finally, we found evidence of an excitonic insulator among the systems, where the excited state are preferable than the semiconducting ground state.

Keywords: Transition Metal Halides, Two Dimensional, Monolayer, Excitons.

Resumo

Os materiais bidimensionais têm experimentado um rápido crescimento desde a primeira esfoliação do grafeno em 2004, que é uma folha atomicamente fina de átomos de carbono esfoliada do grafite. Apesar de várias propriedades sem precedentes do grafeno, induzidas pelo confinamento quântico, ele carece de um gap de banda, o que limita algumas aplicações optoeletrônicas. porém o grapheno motivou um novo campo de pesquisa de materiais bidimensionais, com suas potenciais composições e estruturas, variando de isolantes a semicondutores e condutores. A ampla gama de comportamento condutivo dentro do confinamento quântico dá origem a comportamentos distintos, incluindo uma grande energia de ligação do exciton. Excitons são quasi-partículas formadas por um par elétron-buraco que interage através da atração de Coulomb, um fenômeno presente em semicondutores, mas mais notável em materiais de baixa dimensão devido ao confinamento quântico, que altera o ambiente dielétrico. No entanto, métodos teóricos de partículas individuais, como a teoria do funcional da densidade no estado fundamental, não descrevem excitons porque é um fenômeno de muitos corpos. Assim, uma caracterização completa das propriedades ópticas dos materiais bidimensionais requer ir além de uma perspectiva de partículas individuais. Motivado pelas conquistas de vários materiais bidimensionais e perovskitas halogenadas, este trabalho explora uma nova classe de materiais bidimensionais, a saber, monocamadas de haletos de metais de transição (TMHs). Inicialmente, selecionamos TMHs potenciais para optoeletrônica no Banco de Dados Computacional de Materiais 2D (C2DB) e, subsequentemente, analisamos as propriedades estruturais, eletrônicas, ópticas e excitônicas usando métodos teóricos de ponta como cálculos de Teoria do Funcional da Densidade (DFT) incluindo correções relativísticas e de gap de banda, e a avaliação de propriedades ópticas incluindo efeitos excitônicos dentro de Hamiltonianos de Ligação Forte (TB) e pela solução da equação de Bethe-Salpeter (BSE) para estudar esses materiais. Nossos cálculos mostram que a estrutura de equilíbrio calculada pelo C2DB concorda com

os cálculos realizados aqui. No entanto, as propriedades eletrônicas exibem desvios importantes que não são homogêneos entre os sistemas Por exemplo, observamos desvios nos valores de gap de banda de até 17 % ao considerar correções relativísticas e para o valor corrigido do gap de banda calculado aplicando a metodologia do operador tesoura. Também calculamos propriedades ópticas e excitônicas resolvendo as equações de Bethe-Salpeter, mostrando absorção de luz isotrópica e anisotrópica entre os sistemas. A inclusão de efeitos excitônicos diminuiu a máxima absorção de luz quando comparada ao coeficiente de absorção sem esses efeitos e também alterou a região de energia dos espectros de absorção máxima. As composições demonstraram considerável energia de ligação, destacando a importância de estudar esta quasi-partícula em cálculos teóricos. As possíveis heterojunções são fortemente influenciadas pelos efeitos excitônicos; portanto, a avaliação de possíveis heterojunções deve levar em consideração os excitons. Finalmente, encontramos evidências de um isolante excitônico entre os sistemas, onde os estados excitados são preferíveis ao estado fundamental semicondutor.

Palavras-chave: Haletos de Metais de Transição, Bi-dimensionais, Monocamada, Éxcitons.

Acknowledgments

First, I express my heartfelt gratitude to my family for their unwavering support throughout my life and my studies. To my father, Wellington, and my mother, Silvia, who have always believed in me and encouraged my studies despite the distance. To my younger sister, Maria Eduarda, whom I hope to inspire to follow her dreams.

I am deeply grateful to my advisor, Professor Matheus Paes Lima, for his invaluable guidance throughout my master's and for the privilege of working with him since my undergraduate studies. I also thank Professor Juarez L. F. da Silva for his continuous support in developing my skills and providing scientific and technical assistance. Thanks Professor Alexandre Cavalheiro Dias for technical support.

I appreciate the faculty and staff at UFSCar for their support throughout this journey. The companionship with fellow students from the Physics Department and the Federal University of São Carlos (UFSCar) made this process more enjoyable, through shared lunches, discussions, seminars, and social events. Special thanks to my lab colleagues João, Lucas, Marco, Mateus, Jean and Paulo, for the numerous conversations and gathering together that made the journey easier.

Gratitude extends to my colleagues from the Physics Week (SeFís) organizing committee, who worked tirelessly to promote physics and science to the public. I also thanks the QTNano group and CINE members for stimulating scientific discussions. My friends in São Carlos have enriched my life in this city, making it a memorable experience.

I am thankful to the teachers and staff at Influx English School for helping me improve my English, enabling me to better communicate with researchers around the world and to write this dissertation in English. Thanks to my PSTU colleagues for the many stimulating debates and fights and to my capoeira friends and masters, Ipê, Lirio, and Leo for their valuable lessons.

Finally, I acknowledge the support of FAPESP (São Paulo Research Foundation, Grant Numbers 2017/11631-2, 2018/21401-7), Shell, and the strategic importance of the support provided by ANP (Brazil's National Oil, Natural Gas and Biofuels Agency) through the R&D levy regulation. This study was partially funded by the National Council for Scientific and Technological Development (fellowships for Natan Moreira Regis).

"Workers of the world, unite!"

– The Communist Manifesto

Contents

List of Tables

List of Figures

Abbreviations

Abbreviations	**description**
2D	Two-dimensional
TMD	Transition-metal Dichalcogenide
PVK	Perovskite
TMH	Transition-metal halide
vdW	van der Waals
hBN	Hexagonal boron nitride
MXenes	Metal carbides and nitrides
PL	Photoluminescence
CBM	Conduction Band Minimum
VBM	Valence Band Maximum
DFT	Density Functional Theory
BSE	Bethe-Salpeter Equation
GW	Green's Function and the Screened Coulomb Interaction
CI	Configuration-Interaction
CVT	Chemical vapor transport
AIMD	*Ab initio* molecular dynamics
PBE	Perdew-Burke-Ernzerhof
HSE06	Heyd-Scuseria-Ernzerhof
C2DB	Computational 2D Materials Database
TB	Tight-Binding
BO	Born-Oppenheimer
IPA	Independent Particles Approximation
MB	Many-Body
HK	Hohenberg-Kohn
XC	Exchange-Correlation
KS	Kohn-Sham

LDA	Local Density Approximation
GGA	Generalized Gradient Approximation
HF	Hartree-Fock
SR	Short Range
LR	Long Range
BZ	Brillouin Zone
USPP	Ultra-Soft Pseudopotentials
LAPW	Linearized Augmented Plane Wave
PAW	Projector Augmented Wave Method
AE	All Electron
PS	Pseudo
SOC	Spin-Orbit Coupling
MLWF	Maximally Localized Wannier Functions
TDA	Tamm-Dancoff Approximation
re	real
img	imaginary
SQ	Shockley-Queisser
EI	Excitonic Insulator

Chapter 1

Introduction

This chapter begins by motivating the study of two-dimensional (2D) transition metal halides (TMHs) as promising new compositions for optoelectronic applications, drawing on promising research in graphene, transition metal dichalcogenides (TMDs), and halide perovskites (PVK). We then summarize excitonic effects, particularly in two-dimensional materials, to underscore the importance of studying these effects through many-body approaches compared to single-particle perspectives, which more effectively describe several properties of crystalline systems, such as the response of 2D materials to light. The subsequent section reviews the experimental and theoretical studies of TMHs and establishes the open problems. Finally, we present the goals of this dissertation, focusing on the impact of excitons on the optical properties of TMHs.

1.1 Motivations and Justifications

1.1.1 Two-Dimensional Layered Materials

During the past century, predictions suggested that 2D materials were not feasible due to thermodynamic instability, as pointed out by Peierls[3] and Landau[4]. However, the graphene structure, comprising a single layer of carbon atoms, was predicted as early as 1948[5], with its synthesis achieved in 2004 through the work of Geim and Novoselov[6]. This milestone paved the way for the 2D research field, that is, materials with quantum confinement in one of its directions. They employed the Scotch tape method to isolate graphene from graphite, exemplified in figure 1.1. This synthesis

mechanism is possible because of the layered structure of graphite, in which carbon atoms are bound by covalent interactions; nevertheless, van der Waals (vdW) forces are responsible for the inter-plane interaction. This type of material with a layered structure bound by vdW forces is called vdW crystals, and mechanical exfoliation can commonly be used for their production[7].

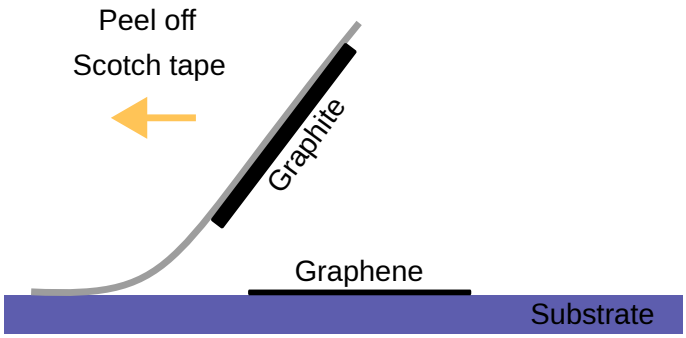

Figure 1.1: Simplified representation of Scotch tape method for producing graphene sheets. The method involves placing graphite in the Scotch tape and then peeling the tape several times in the substrate until the graphene sheets are archived. [source: own authorship]

The remarkable properties of graphene, including high charge carrier mobility at room temperature[8], exceptional mechanical strength[9], high thermal conductivity[10], and optical transparency and flexibility[11], enhance its potential for various applications, such as field-effect transistors[12,13] and biomolecule and gas sensing[14,15]. Although graphene exhibits these remarkable properties, it lacks a band gap, which restricts its potential applications. Nevertheless, the synthesis of graphene has motivated researchers to investigate other 2D materials, introducing a new research field. Among these 2D, hexagonal boron nitride[16] (h-BN), transition metal dichalcogenides[17] (TMDs), and metal carbides and nitrides[18] (MXenes) are promising materials. Notably, TMDs have garnered significant attention due to the stability and semiconducting behavior of several compounds within this family. The TMDs structures consist of a transition metal layer sandwiched between two layers of chalcogenides, as depicted in figure 1.2. Furthermore, multiple layers are held together by vdW interactions, with some stacking possibilities, including the most stable 2H configuration[1].

Among the 2H phase of TMDs, molybdenum disulfide (MoS_2), molybdenum diselenide ($MoSe_2$), tungsten disulfide (WS_2), and tungsten diselenide (WSe_2) have attracted significant interest due to their stability, favorable optical properties, and

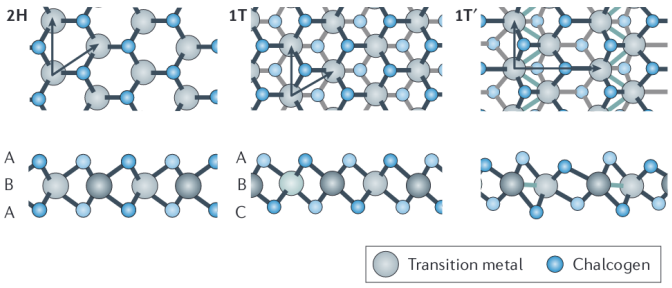

Figure 1.2: Posible structures of single layers of TMDs in top and side view. The arrows show the lattice vectors. [source: adapted from ref. 1.]

semiconducting behavior[1]. The properties of TMDs have been demonstrated to depend on the number of layers, with a notable effect of indirect-to-direct band gap transition from bulk to monolayer in MoS_2[19]. Moreover, TMDs based on tungsten (W) and molybdenum (Mo) exhibit notable photoluminescence (PL) effects dependent on the number of layers[20] and are orders of magnitude stronger than bulk structures[21,20]. These properties make TMDs suitable for various optoelectronic applications, including transistors, memory devices, valleytronics, and photovoltaics[22,23,24,25].

In addition, perovskite materials have emerged as promising candidates for photovoltaics in recent years. Specifically, halide-based PVKs[26] with devices capable of achieving efficiencies up to 25 %[27,28], comparable to the usual silicon-based solar cells[28] with an efficiency of approximately 26.7 %. These perovskite-based devices offer a significant advantage through their low-cost fabrication methods[29], despite the stability problems[30]. Fabrication techniques often involve solution-based synthesis of halide perovskites[31], characterized by their ionic bonding, allowing scalable and efficient production processes that can potentially be adapted for 2D transition metal halides.

Thus, Motivated by the syntheses of layered two-dimensional materials, such as graphene and hBN, by the accomplishments of transition metal transition metal dichalcogenides (TMDs) which is a family of materials with several semiconducting stable compounds with vast applications field and the potential of Halide PVK due to its low cost, this work proposes the investigation of transition metal halides (TMHs), a class of layered materials comprising a transition metal and a halide atom, which are chlorine (Cl), bromine (Br), and iodine (I). Several TMH structures have been experimentally studied, such as bismuth iodide (BiI_3)[32], germanium diiodide

(GeI_2)[33], chromium trichloride ($CrCl_3$)[34], and lead iodide (PbI_2)[35,36]. Most of these compounds have stoichiometries AB_2 and AB_3[37]. In addition, several theoretical works reports additional compositions that will be presented in detail in section 1.2.

1.1.2 Excitons in Two-dimensional Materials

The exciton is a quasiparticle formed by an electron-hole pair bound through Coulomb attraction, as exemplified in figure 1.3 a). It is essential to note that single-particle methods, such as Hartree-Fock (HF) and ground-state density functional theory[1] (DFT), cannot describe excitons because they are a many-body phenomenon. When contrasting single-particle and many-particle calculations, quasiparticle states emerge, denoted by $E_0, E_1, \ldots E_n$ (exemplified in figure 1.3 c)) situated above the bandgap, leading to alterations in the optical response of materials. Consequently, a complete characterization of the optical properties of crystalline systems requires going beyond the single-particle perspective. The excited state of the lowest energy (E_0) is known as the fundamental exciton, while the difference between E_0 and the conduction band minimum (CBM) is the exciton binding energy (E_b).

The dielectric constant plays a crucial role in determining excitonic properties, as its large value (as seen in semiconductors) diminishes the Coulomb interaction between electron-hole pairs. In contrast, smaller dielectric constants, such as those found in ionic crystals[17], lead to stronger interactions. This dichotomy gives rise to two distinct types of excitons: Wannier-Mott excitons[38], characterized by weakly bound electron-hole pairs with a large interaction radius spanning multiple unit cells; and Frenkel excitons[39], marked by tightly bound pairs, typically confined to the same or nearest-neighbor unit cells. Figure 1.3 b) illustrates these two types of excitation.

The exciton's properties also depend on the dimensionality of the material due to quantum confinement: in three-dimensional materials, the electron-hole pair experiences dielectric screening, whereas in two-dimensional materials, the confinement of the exciton in two dimensions leads to reduced dielectric screening due to interactions with the vacuum or substrate. This is exemplified in figure 1.3 d), which tends to increase the exciton binding energy[40]. As a result, despite being described since the 1930s by Frenkel's work[39], the interest in exciton properties has increased due to observations that single-particle theoretical models do not accurately describe

[1] In the most common implementations, such as the used here.

optical properties in two-dimensional materials, such as TMDs[41]. Another crucial aspect of excitonic physics is the distinction between bright and dark excitons, which are accessible (not accessible) via optical transitions.

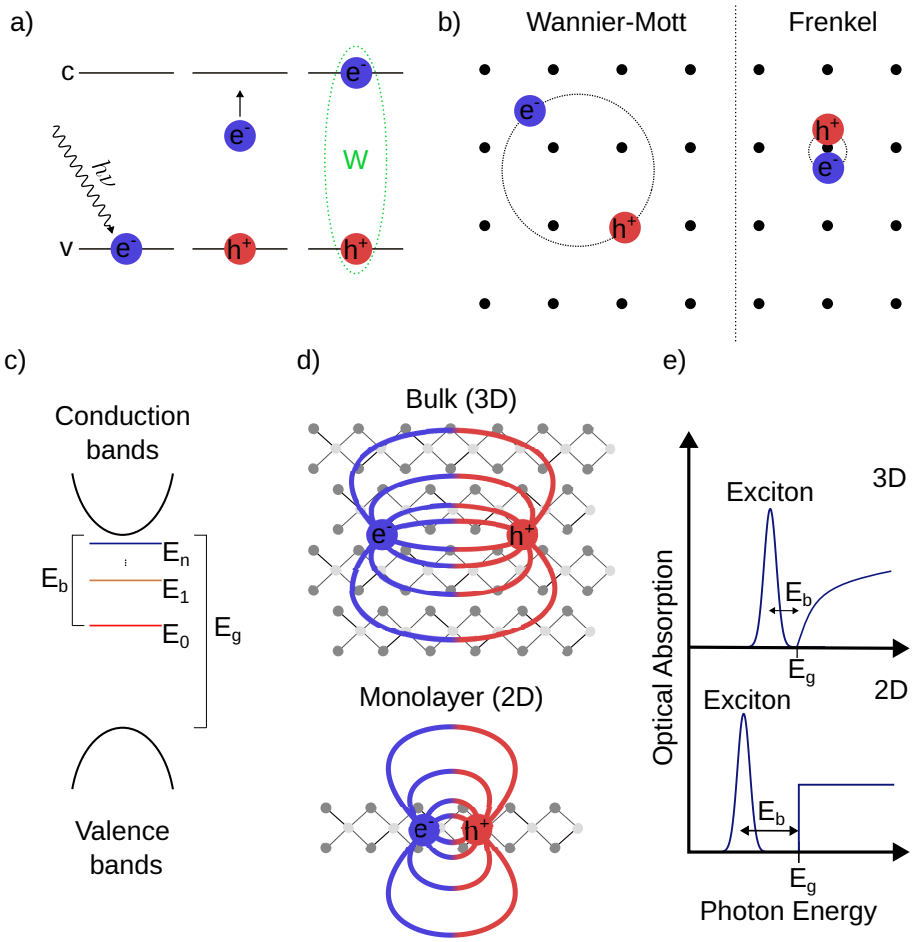

Figure 1.3: Summary of excitons properties. a) Simplified process of exciton formation by light radiation. b) Representation of Wannier-Mott and Frenkel excitons. c) Excitonic states and relation to electronic band structure. d) Difference of exciton in bulk (3D) and Monolayer (2D) structure. e) Effect of the dimensionality of the system in absorption coefficient considering excitonic effects. [source: own authorship]

Lastly, theoretical calculations offer various methods for describing excitons, as summarized below:

- The DFT+GW+ Bethe-Salpeter equation (BSE) approach, such as BerkeleyGW code[42,43,44] calculates the ground state using DFT, corrects the self-energy of electrons and holes with the GW method and describes two-particle correlations and excitonic effects through BSE. This approach provides an

accurate description of exciton levels and binding energy[45], however it is computationally expensive and complex to achieve convergence.

- The perturbation[46] and effective mass[47] methods calculates electronic and excitonic properties near band extremes using perturbation or effective mass. While these methods simplify exciton descriptions, they may not accurately describe complex band structures or high-order contributions.
- The Configuration-Interaction (CI) method[48,49] expands the interaction wavefunction based on multiple excitations. Although this approach generates a systematic treatment of multiple excitations, the Hilbert space increases quickly, rendering it computationally unaffordable.
- The BSE+TB approach[50,51] expands ground states in a set of discrete orbitals and solves many-body effects using BSE based on those orbitals. Generally, this method is less demanding than GW calculations but less accurate for predicting absolute energy levels.

1.2 Literature Review on 2D Transition Metal Halides

This section overviews experimental and theoretical works on two-dimensional transition metal halides (2D TMHs). Initially, we present the main synthesis methods and summarize the experimental studies of TMHs. Subsequently, we provide an overview of theoretical studies, focusing on stability and feasibility. Lastly, electronic and optical properties, including excitonic investigations, are presented in both theoretical and experimental works.

1.2.1 Experimental Synthesis Methods

Several transition-metal halide layered structures have been successfully synthesized via various methods. Notable examples of physical deposition techniques include bismuth triiodide thin films (BiI_3)[32] and nanoplates[52]. Wang *et al.*[36] reported the production of nanoflakes using confined physical vapor deposition, while Zhong *et al.*[35] fabricated PbI2 nanosheets via physical phase deposition.

Chemical vapor transport (CVT) methods have also been utilized for the production of TMHs. Gronke *et al.*[53] investigated α-$MoCl_3$ nanosheets by CVT. Similarly, Jiang *et al.*[54] provided a route for the synthesis of 2D magnetic transition metal di-

halides through the reduction of trihalide powders using chemical vapor deposition. McGuire *et al.*[34] reported the growth of single plate-like crystals of $CrCl_3$ by crystallization of commercial $CrCl_3$ using CVT and later studied the growth of α-$MoCl_3$ crystals employing the same technique[55]. Li *et al.*[56] synthesized BiI_3 nanoplates using chemical vapor transport and deposition methods.

Other alternatives for synthesizing TMHs include liquid-phase methods. For instance, Fan *et al.*[57] explored the synthesis of PbI_2 nanosheets via liquid exfoliation. Lin *et al.*[58] demonstrated the synthesis of micro and nano α-HgI_2 sheets using a liquid-phase mineral agent-assisted method. Tan *et al.*[59] synthesized PbI_2, PbFI, and $Pb_5F_8I_2$ nanosheets by recrystallization of aqueous solutions. Zheng *et al.*[60] described a method to produce 2D layered PbI_2 by a liquid phase method heated under atmospheric conditions. Furthermore, Lee *et al.*[61] achieved film thicknesses of approximately 150 nm using the spin-coating method and thermal annealing for the production of thin films of CuI. Ni *et al.*[62] employed high-pressure techniques to produce layered honeycomb IrI_3. Peng *et al.*[63] reported the synthesis of CrI_2 films grown on a graphite substrate. Sandoval *et al.*[64] utilized template-assisted growth of monolayers of CeI_3, $CeCl_3$, $TbCl_3$, and ZnI_2 within carbon nanotubes. Finally, Wang *et al.*[65] described the production of honeycomb RhI_3 flakes by mechanical exfoliation from bulk structures.

1.2.2 Theoretical Analysis of Stability and Feasibility

In addition to experimental works, numerous theoretical studies have explored other compositions that have not been synthesized or are complementary, establishing the stability and potential for synthesizing TMHs. These studies often employ phonon spectra analysis to determine vibrational stability and dynamic stability through ab initio molecular dynamics (AIMD). Using these methods, researchers have demonstrated the stability of mercury[66], hafnium[67,68], copper and silver[69], titanium[70,71], zirconium[72,73], gold[74], and palladium[75] based TMH monolayers, i.e., containing Cl, Br, and I.

Other studies have explored the stability at elevated temperatures. For example, Liu *et al.*[33] showed through first-principles calculations that monolayer GeI_2 is dynamically and thermally stable up to 600 K. Sun and Kioussis[76] predicted the properties of 2D MnX_3 (X = F, Cl, Br, and I) and demonstrated that these compositions are dynamically and thermodynamically stable up to high temperatures: up to 600 K

for $MnBr_3$ and up to 1200 K for MnF_3, $MnCl_3$, and MnI_3. Kadioglu *et al.*[77] showed that RhX_3 (X = Cl, Br, I) monolayers are stable at room and elevated temperatures, calculated by equilibrium molecular dynamics.

Alternatively, stability can also be assessed through energy calculations. Gao *et al.*[78] showed that for some structures of silver and copper monohalides, the cohesive energy is close to or greater than that of their bulk counterparts according to DFT simulations. Kulish and Huang[79] analyzed single-metal halide monolayers MX_2 (M = V, Cr, Mn, Fe, Co, Ni and X = Cl, Br, I) and demonstrated that these compounds are energetically and dynamically stable, with formation energies comparable to those of some TMDs that have already been synthesized.

The possibility of synthesis can be calculated by estimating the exfoliation energy. Huang *et al.*[72] focused on single-layer zirconium dihalides ZrX_2 (X = Cl, Br, and I) and determined a cleavage energy near 0.295 J/m^2. Yue *et al.*[80] suggested that the $ZnCl_2$ monolayer can be exfoliated from its bulk counterpart with an exfoliation energy of 0.1341 J/m^2. Both values are close to those of other 2D materials known to be produced by mechanical exfoliation, such as graphene (0.37 J/m^2), suggesting the feasibility of mechanical exfoliation.

1.2.3 Electronic, Optical and Excitonic Properties

The results presented in the previous two sections show the possibility of fabrication through several experimental methods and the potential stability of several TMH compounds through theoretical calculations. In addition, the electronic, optical, and excitonic properties were determined for several compositions of this family.

The band gaps of TMHs exhibit a diverse behavior. Specifically, Brandt *et al.*[32] determined the bandgap of BiI_3 to be 1.8 eV. Ersan[81] calculated indirect band gaps of 0.70 eV and 0.32 eV for $RuBr_3$ and RuI_3 monolayers, respectively, using DFT calculations with the PBE functional. CuBr, CuI, AgBr, and AgI monolayers have direct band gaps ranging from 3.12 to 3.36 eV[69] calculated using DFT with the HSE06 functional. GeI_2 is a wide-bandgap semiconductor with a band gap of 2.59 eV[33]. Xu *et al.*[82] showed that the HgI_2 monolayer exhibits a suitable direct band gap of 2.45 eV using DFT calculations with the HSE06 functional, which includes spin-orbit coupling. Sun *et al.*[76] demonstrated the properties of 2D MnX_3 (X = F, Cl, Br, I) as Dirac half-metals, where one spin channel has a large band gap and the other a Dirac cone.

These materials are also suitable for bandgap engineering, as demonstrated by Fang *et al.*[83], who studied RhI_3 crystals and showed a quasi-linear bandgap narrowing, including predictions of metallization at 19.9 GPa. Tang *et al.*[71] also demonstrated the effect of strain on electronic properties, which includes changes in the indirect band gap of a $TiCl_2$ single layer under strain, ranging from 2.72 eV to 3.14 eV for $-2\,\%$ and $6\,\%$. Yan *et al.*[84] showed that pressure-induced bandgap closure occurs for CdI_2 around 34.5 GPa, and the material undergoes insulator-to-semiconductor and semiconductor-to-metal transitions at 36 and 62 GPa, respectively. Yue *et al.*[80] noted a modulation of the bandgap for MX_2 (M = Zn, Cd, and X = Cl, I) monolayers, including indirect-to-direct bandgap transitions by application of strain. Furthermore, they reported that strain engineering can enhance light absorption in visible and near-ultraviolet regions.

Kuklin *et al.*[74] showed that AuBr (AuI) monolayers exhibit a tunable direct (indirect) band gap depending on the number of layers, using DFT calculations. Films of CrI_2 have a nearly thickness-independent bandgap of approximately 3.2 eV[63]. Sahoo *et al.*[85] have demonstrated that mercury-based halides are direct bandgap semiconductors in both bulk and monolayer forms. Wang *et al.*[65] showed that RhI_3 nanoflakes have a tunable optical bandgap ranging from 1.1 eV (18 layers) to 1.4 eV (2 layers).

Acharya *et al.*[86] studied bulk and monolayer chromium tri-halides CrX_3 (X = Cl, Br, I) using the Green function-based approach of many-body perturbation and BSE. They showed that the excitons in those compounds originate from bands rather than purely Frenkel (localized) character. In addition, the hybridization between the Cr d and halide p orbitals enhances as the halogen atom becomes heavier, increasing the exciton intensity and decreasing the binding energy.

Regarding excitonic effects, Grzeszczyk *et al.*[87] investigated excitons in 2D ferromagnetic systems, specifically $CrBr_3$ and CrI_3. They demonstrated that the sign of the hole-magnetization coupling is opposite for both $CrBr_3$ and CrI_3 between their ground and excited exciton states. In $CrBr_3$, excitonic spins can be pumped through a spin-dependent absorption process, which does not occur in CrI_3 due to the recovery of its antiferromagnetic state in the excited state, characterized by Wannier–Mott physics. Other work[74] showed that gold-based TMHs exhibit dark excitons with a binding energy of nearly 1.3 eV. Zhao *et al.*[88] studied the Janus monolayer based on titanium, which exhibits a giant magnetic proximity effect that

alters the excitonic character (bright/dark) in TiBrI. Acharya *et al.*[86] investigated bulk and monolayer chromium trihalides, CrX_3 (X = Cl, Br, I), using the Green function-based approach of many-body perturbation theory and BSE. They demonstrated that excitons in these compounds originate from bands rather than from purely Frenkel characters. Also, the hybridization between Cr d and I p orbitals increases as the halogen atom becomes heavier, enhancing the exciton intensity and decreasing the binding energy.

Finally, other works demonstrate the ability to absorb and transmit light, such as PbI_2 nanosheets, which exhibit efficient femto- and nanosecond-pulse excitations in the visible region[57]. Another work reveals a light absorption coefficient of 10×10^5 cm^{-1} in visible spectral regions, accompanied by a power conversion efficiency of approximately 12 % for $TiBr_2/TiCl_2$ heterojunctions[70]. In conclusion, the findings presented in this section highlight interest in 2D transition-metal halides, which have been experimentally explored, whereas several studies indicate stability and feasibility through theoretical calculations. Additionally, several compounds within this family display favorable electronic, optical, and excitonic properties for opto-electronic applications, showcasing promising potential for electronic and excitonic engineering.

Table 1.1: Summary of electronic, optical, and excitonic Properties of TMH Compounds found in literature.

Material	**Property**	**Method**	**Ref.**
BiI_3	Bandgap: 1.8 eV	Experimental	32
$RuBr_3$	Bandgap: 0.70 eV (indirect)	DFT (PBE)	81
RuI_3	Bandgap: 0.32 eV (indirect)	DFT (PBE)	81
CuBr, CuI, AgBr, AgI	Bandgap: 3.12 to 3.36 eV (direct)	DFT (HSE06)	69
GeI_2	Bandgap: 2.59 eV	Experimental	33

Continued on next page

Material	**Property**	**Method**	**Ref.**
HgI_2	Bandgap: 2.45 eV (direct)	DFT (HSE06 + SOC)	82
MnX_3 (X = F, Cl, Br, I)	Dirac half-metals	Theoretical	76
RhI_3	Bandgap narrowing under pressure	Experimental	83
$TiCl_2$	Bandgap: 2.72 to 3.14 eV (under strain)	Theoretical	71
CdI_2	Pressure-induced bandgap closure	Experimental	84
MX_2 (M = Zn, Cd; X = Cl, I)	Indirect-to-direct bandgap transition	Theoretical	80
AuBr, AuI	Tunable bandgap (layer-dependent)	DFT	74
CrI_2	Thickness-independent bandgap: 3.2 eV	Experimental	63
RhI_3	Tunable optical bandgap: 1.1 to 1.4 eV	Experimental	65
CrX_3 (X = Cl, Br, I)	Excitons from band hybridization	Theoretical	86
$CrBr_3$, CrI_3	Excitonic spins, hole-magnetization coupling	Experimental	87

Continued on next page

Material	Property	Method	Ref.
TiBrI	Magnetic proximity effect on excitons	Theoretical	88
PbI_2	Efficient light absorption (fem-to/nanosecond pulses)	Experimental	57
$TiBr_2/TiCl_2$ heterojunctions	Light absorption coefficient, PCE 12 %	Theoretical	70

1.3 Open Problems

Numerous experimental and theoretical studies on 2D transition metal halides address several problems on this materials family. However, several problems remains open. Initially, a comprehensive characterization of the optoelectronic properties using theoretical calculations need to include excitonic properties in the calculations due to the large excitonic effect in the optical response of these materials, as stated in section 1.1.2 and as showed in the previous section. Secondly, several methods for calculating excitons only explore part of the excitonic physics, such as the calculation of the optical bandgap, whereas the calculations of full optical properties considering those effects are not considered. Thirdly, an affordable computational methodology allows the exploration of larger and diverse systems. Finally, standardizing employing state-of-the-art theoretical methods can help explore the full potential of several compositions.

1.4 Goals

This work aims to screen promising 2D TMHs for optoelectronic applications, including the impact of excitons on their properties. Initially, promising compositions were selected in the Computational 2D Materials Database[89,90] (C2DB), which possesses more than 16.000 two-dimensional materials, including several properties studied by a high-throughput workflow. Next, state-of-the-art ab initio simulations were performed using density functional theory (DFT), while optical properties were based

on the tight-binding Hamiltonian (TB) obtained from electronic structure calculations. The Bethe-Salpeter equation was solved to characterize excitonic properties. The following specific goals were defined for this study:

1. **System Selection:** Select promising 2D TMHs on C2DB, including AB, AB_2, and AB_3 stoichiometries; materials with bandgaps that correspond to efficiency above 20 % in the Shockley–Queisser limit; stable materials; and non-magnetic compositions.
2. **Density Functional Calculations:**
   - Perform structural optimizations and compare them with C2DB structures and other articles in the literature.
   - Calculate the density of states to characterize the main atomic and orbital contributions near the Fermi level.
   - Calculate the electronic band structure, characterizing the band gap, and including the effects of relativistic corrections.
   - Calculate the band-gap correction to accurately describe the electronic transitions for the single-particle electronic structure.
3. **Wannierization:** The DFT electronic structure will be parameterized using Maximum Localized Wannier Functions, which will extract the TB Hamiltonian.
4. **Optical and quasi-particle calculations:**
   - Based on the electronic TB Hamiltonian, excitonic properties will be calculated by solving the Bethe-Salpeter Equation.
   - Calculate optical properties in both single-particle and quasi-particle perspectives.
5. **Determining the excitonic properties:** Here, the effect of excitonic properties will be contrasted with a single-particle perspective, including band alignment to show possible heterojunctions.

The detailed workflow of this dissertation is presented in figure 1.4, with the methodology discussed in chapter 2 and the results in chapter 3.

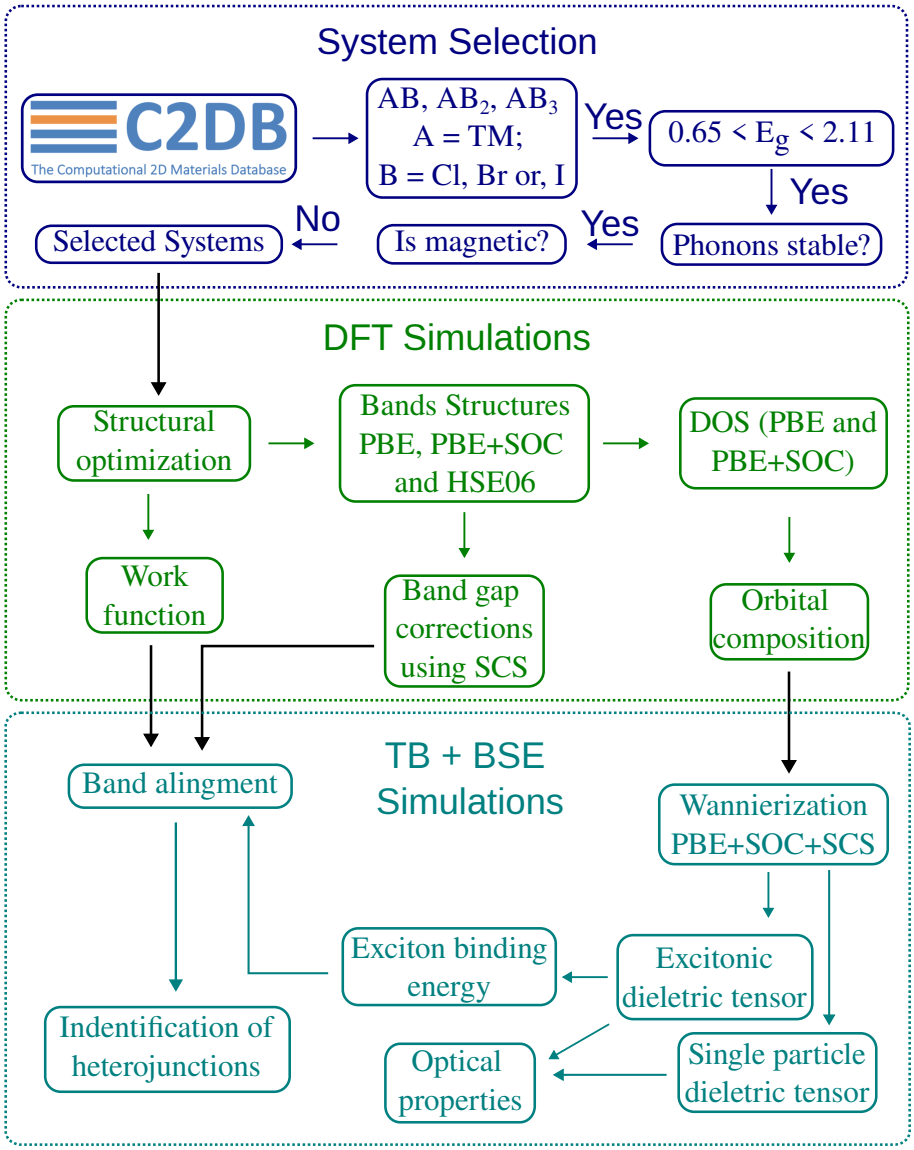

Figure 1.4: Workflow of this dissertation. The first panel (blue) depicts the system selection procedure in C2DB. The second panel (green) details the DFT simulations. The bottom panel (green water) shows the TB and quasi-particle calculations. [source: own authorship]

Chapter 2

Theoretical and Computational Methods

This chapter outlines the theoretical framework and computational methodologies used in this study. Section 2.1 introduces the many-body (MB) quantum problem. Subsequently, section 2.2 presents density functional theory (DFT), including the approximations for exchange-correlation functionals (XC) and spin-orbit coupling, to characterize structural and electronic properties. Section 2.3 presents the formalism for periodic systems, including the Bloch theorem. Section 2.6 shows the calculation of optical properties from the perspective of a single particle and considers excitonic properties by solving the Bethe-Salpeter equations using a Hamiltonian parameterized with tight binding (TB) using maximally localized Wannier functions, as detailed in section 2.5. Finally, appendix C presents the computational tools and parameters used throughout this work.

2.1 Many Body Quantum Problem

On an atomic scale, electrons and nuclei constitute the building blocks of atoms, molecules, and crystals. Despite the presence of other forces, such as gravitational and nuclear forces, the Coulomb interaction predominates in determining structural, electronic, and optical properties. The dominance of the Coulomb interaction stems from the significant difference in magnitude between the gravitational potentials and the Coulomb for nuclei and electrons (at least 10^{-9}) and the limited range of interaction of the nuclear forces (10^{-15} m), which confines the nucleus without

affecting the properties of our interest.

In non-relativistic cases, the time-independent Hamiltonian for these systems, in Hartree units, is:

$$\hat{H} = -\overbrace{\sum_{i=1}^{N} \frac{\nabla_i^2}{2}}^{T_e} - \overbrace{\sum_{A=1}^{M} \frac{\nabla_A^2}{2M_A}}^{T_n} - \overbrace{\sum_{i=1}^{N}\sum_{A=1}^{M} \frac{Z_A}{r_{iA}}}^{V_{ne}} + \overbrace{\sum_{i=1}^{N}\sum_{j\neq i}^{N} \frac{1}{r_{ij}}}^{U_{ee}} + \overbrace{\sum_{A=1}^{M}\sum_{B\neq A}^{M} \frac{Z_A Z_B}{R_{AB}}}^{V_{nn}} \ , \quad (2.1)$$

This Hamiltonian operator consists of the sum of the kinetic energy of electrons (T_e) and nuclei (T_n), the electrostatic interaction between electrons and nuclei (V_{ne}), and the interactions between electrons (U_{ee}) and nuclei (V_{nn}). Here, M_A and Z_A represent the mass and atomic number of the nuclei, r_{iA} indicates the distance between the electrons and the nuclei, r_{ij} denotes the distance between the electrons, R_{AB} represents the distance between the nuclei, and ∇_i^2 (∇_A^2) is the kinetic operator for the electrons (nuclei). As the Hamiltonian in equation 2.1 does not depend on time, determining the quantum states involves finding the stationary states by solving the MB time-independent Schrödinger equation:

$$\hat{H}\Psi(\mathbf{r}_1 \dots \mathbf{r}_N, \mathbf{R}_1 \dots \mathbf{R}_M) = E\Psi(\mathbf{r}_1 \dots \mathbf{r}_N, \mathbf{R}_1 \dots \mathbf{R}_M) \ , \quad (2.2)$$

where Ψ is the wave function and E is the total energy. The set $\mathbf{r}$ represents the electrons' positions and $\mathbf{R}$ represents the positions of the nuclei.

Although equation 2.2 completely determines the quantum problem stated above, solving this equation is rather prohibitive and generally increases exponentially[91,92]. The first simplification involves noting that the dynamics of the nuclei are slower than that of the electrons. So, the electron dynamics can be considered to occur with fixed nuclei. This is known as the Born-Oppenheimer (BO) approximation[93], which allows the decoupling of the dynamics of the electrons and nuclei. The use of BO separation allows the identification of the electronic Hamiltonian in the MB Hamiltonian (equation 2.1):

$$H_{ele} = -\sum_{i=1}^{N} \frac{\nabla_i^2}{2} - \sum_{i=1}^{N}\sum_{A=1}^{M} \frac{Z_a}{r_{iA}} + \sum_{i=1}^{N}\sum_{j\neq i}^{N} \frac{1}{r_{ij}} \ , \quad (2.3)$$

that gives rise to the Schrödinger equation for electrons:

$$\hat{H}_{ele}\psi(\mathbf{r}_1,\dots\mathbf{r}_N;\mathbf{R}_1\dots\mathbf{R}_M) = \psi(\mathbf{r}_1,\dots\mathbf{r}_N;\mathbf{R}_1\dots\mathbf{R}_M)\ . \tag{2.4}$$

Here, the electronic wave functions depend parametrically on the nuclear coordinates, as the Hamiltonian $\hat{H}_{ele}$ includes an electron-nuclei Coulomb potential. Employing the BO approximation, the nuclear motion will be determined by Coulomb repulsion and the energy surface generated by the electrons, as solving Equation 2.4. In this work, the classical conjugate gradient algorithm[94] governs the dynamics of the nuclei.

2.1.1 Independent Electrons Approximation

As mentioned in the previous section, the wave function of the electronic Schrödinger equation (equation 2.4) depends on all electrons and nuclear coordinates, represented as $\psi = \psi(\mathbf{r}_N;\mathbf{R}_M)$, for N electrons and M nuclei. It worth noting that the Hamiltonian in equation 2.3 resembles that of independent electrons with an external potential when electron-electron repulsion is ignored. By temporarily neglecting the Coulomb interaction between electrons, we obtain the following Schrödinger equation:

$$\left[\sum_{i=1}^{N}\frac{\nabla_i^2}{2} - \sum_{i=1}^{N}\sum_{A=1}^{M}\frac{Z_a}{r_{iA}}\right]\psi = \epsilon\psi\ . \tag{2.5}$$

Such a drastic simplification allows us to write the MB wave function (ψ) as a combination of individual electrons orbitals ($\phi_i(\mathbf{r}_i;\mathbf{R}_M)$) in form of Slater determinant, which takes into account the Fermi exclusion principle:

$$\psi(\mathbf{r}_1,\dots\mathbf{r}_N;\mathbf{R}_M) = \frac{1}{\sqrt{N!}}\begin{vmatrix}\phi_1(\mathbf{r}_1;\mathbf{R}_M) & \dots & \phi_N(\mathbf{r}_1;\mathbf{R}_M)\\ \vdots & \ddots & \vdots\\ \phi_1(\mathbf{r}_N;\mathbf{R}_M) & \dots & \phi_N(\mathbf{r}_N;\mathbf{R}_M)\end{vmatrix}\ . \tag{2.6}$$

Consequently, the approximation introduced in Equation 2.6 allows mapping an MB problem to a single-body problem. Computing the electron density at each space coordinate ($\mathbf{r}$) is straightforward, as it is obtained as the probability that each orbital

is in this coordinate. That is,

$$n(\mathbf{r}) = \sum_{i=1}^{N} |\phi_i(\mathbf{r}; \mathbf{R}_M)|^2 \ . \tag{2.7}$$

2.1.2 Mean Field Approximation

The independent electrons approximation (IPA) introduced in the last section does not correspond to a real situation where the electronic repulsion cannot be discarded. However, the IPA allows us to write the electronic problem in terms of individual electrons, which simplifies the problem. To address the issue of discarding the electronic repulsion but keeping the single-particle perspective, we can introduce the mean-field approximation, where each electron perceives the repulsion of other electrons as the mean electrostatic potential. Thus, we introduce the Hartree potential:

$$V_H(\mathbf{r}) = \int d\mathbf{r}^{'} \frac{n(\mathbf{r}^{'})}{|\mathbf{r} - \mathbf{r}^{'}|} \ , \tag{2.8}$$

that describes the classical Coulomb interaction between the electron density in two different points of space. So, the equation 2.5, which discards the electron-electron interaction, can berewritten as:

$$\left[\sum_{i=1}^{N} \frac{\nabla_i^2}{2} - \sum_{i=1}^{N} \sum_{A=1}^{M} \frac{Z_a}{r_{iA}} + \int d\mathbf{r}^{'} \frac{n(\mathbf{r}^{'})}{|\mathbf{r} - \mathbf{r}^{'}|} \right] \phi_i(\mathbf{r}) = \epsilon_i \phi_i(\mathbf{r}) \ , \tag{2.9}$$

which maintains the single-particle perspective while taking into account the Coulomb repulsion between electrons.

2.2 Density Functional Theory

In previous sections, we have described the quantum many problem and some possible simplifications, such as the Born-Oppenheimer approximation, where we could identify the electronic Hamiltonian from the many-body Hamiltonian, we introduce the independent particle approximation and mean-field approximation that enable a more simple description of a many-body quantum problem. Despite the simplifications presented in previous sections, density functional theory (DFT) has emerged as a successful tool to describe several properties of atoms, solids, and extended systems at reasonable computational cost[95].

The theory is based on the Hohenberg-Kohn (HK) theorems and the Kohn-Sham equations (KS), as presented in sections 2.2.1 and 2.2.2, respectively. It allows for the description of a many-body problem in terms of electronic density instead of the wave function. This perspective change allows for the mapping of a problem of N electrons in three spatial coordinates, i.e., the 3N problem, into a density problem, which is a single-coordinate problem that depends on three coordinates.

The density functional theory (DFT) aims to define a wavefunction (ϕ) from the perspective of a single particle in the fundamental state, such that it is a function of the density. Similarly, the value of an observable (O) in the fundamental state will also be a function of the density. That is:

$$\phi_0(\mathbf{r}) = \phi_0[\rho_0(\mathbf{r})] \ , \tag{2.10}$$

$$O[\rho_0] = \int \phi_0^*[\rho_0(\mathbf{r})]\hat{O}\phi_0[\rho_0(\mathbf{r})]d\mathbf{r} \ . \tag{2.11}$$

In section 2.1.2, the term for electronic repulsion between two particles is defined in terms of electronic density. Therefore, to proceed, we also need to define the terms for single-particle kinetic energy and the external potential of nuclei to electrons in terms of density. This transition is guaranteed by the Hohenberg-Kohn Theorems presented in the next section.

2.2.1 Hohenberg-Kohn Theorems

The Hohenberg-Kohn (HK) theorems, as stated above, offer the possibility of describing the electronic MB problem in terms of density and obtaining the exact energy in the fundamental state[96].

Theorem 1. *The external potential felt by electrons is a unique functional of the electron density.*

Proof. Suppose that we have an electronic Hamiltonian $\hat{H} = \hat{T} + \hat{U} + \hat{V}$ defined by the sum of kinetic energy ($\hat{T}$), two-electron potential (U), and external potential ($\hat{V}$), leading to the wavefunction $\phi_0 = \phi_0[\rho(\mathbf{r})]$ in the fundamental state. Now, we introduce the Hamiltonian $\hat{H}' = \hat{T} + \hat{U} + \hat{V}'$, which has a different external potential ($\hat{V}'$). The Hamiltonian $\hat{H}'$ has the wave function $\phi_0' = \phi_0'[\rho(\mathbf{r})]$ with the same density as the first Hamiltonian.Considering that the fundamental state is not degenerate,

according to the variational principle:

$$E_0 = \int \phi_0^* \hat{H} \phi_0 d\mathbf{r} < \int \phi_0^{'*} \hat{H} \phi_0^{'} d\mathbf{r} \ ,$$
$$E_0^{'} = \int \phi_0^{*'} \hat{H}^{'} \phi_0^{'} d\mathbf{r} < \int \phi_0^* \hat{H}^{'} \phi_0 d\mathbf{r} \ . \tag{2.12}$$

Combining equation 2.12 we get:

$$\int \phi_0^* \hat{H} \phi_0 d\mathbf{r} < \int \phi_0^{'*} \hat{H} \phi_0^{'} d\mathbf{r} = \int \phi_0^{'*} \hat{H}^{'} \phi_0^{'} d\mathbf{r} + \int \phi_0^{'*} [\hat{V} - \hat{V}^{'}] \phi_0^{'} d\mathbf{r} \ . \tag{2.13}$$

Write the expected value of the external potential as $\int \phi_0^* \hat{V} \phi_0^{'} d\mathbf{r} = \int \rho(\mathbf{r}) v(\mathbf{r}) d\mathbf{r}$, where $v(\mathbf{r})$ represents the Coulomb potential at each point. From equations 2.13 and 2.12:

$$E_0 < E_0^{'} + \int [v(\mathbf{r}) - v^{'}(\mathbf{r})] \rho_0(\mathbf{r}) d\mathbf{r} \ , \tag{2.14}$$

$$E_0^{'} < E_0 + \int [v^{'}(\mathbf{r}) - v(\mathbf{r})] \rho_0(\mathbf{r}) d\mathbf{r} \ , \tag{2.15}$$

then:

$$E_0 + E_0^{'} < E_0^{'} + E_0 \ , \tag{2.16}$$

this presents a contradiction. Since the two wave functions ϕ_0 and $\phi_0^{'}$ are generated by the same density ρ_0, they must be equal to avoid this contradiction. Then, determining the density of the system is equivalent to minimizing the energy as a function of the density.

□

Theorem 2. *The energy in the ground state $E[\rho]$ is minimum for the exact electron $\rho(\mathbf{r})$ density,*

$$E[\rho] = \int \phi^*(\mathbf{r}) \hat{H} \phi(\mathbf{r}) d\mathbf{r} \ . \tag{2.17}$$

Proof. Consider that in the ground state we have density ρ_0 and wave function ϕ_0 generated by the Hamiltonian $\hat{H} = \hat{T} + \hat{U} + \hat{V}$, and there is another state with density ρ and wave function ϕ not generated by the Hamiltonian $\hat{H}$. Hence, the

following relations hold:

$$\begin{aligned} &\rho \neq \rho_0 \Rightarrow \phi \neq \phi_0 \ , \ \text{i.e.} \ , E > E_0 \ , \\ &\rho = \rho_0 \Rightarrow \phi = \phi_0 \ , \ \text{i.e.} \ , E = E_0 \ . \end{aligned} \tag{2.18}$$

Separating the external potential in equation 2.20, we can define a universal functional $F[\rho]$ that is valid for any electronic system:

$$E[\rho] = \overbrace{\int \phi^*(\mathbf{r})[\hat{T} + \hat{U}]\phi(\mathbf{r})d\mathbf{r}}^{F[\rho]} + \int \phi^*(\mathbf{r})\hat{V}\phi(\mathbf{r})d\mathbf{r} \ , \tag{2.19}$$

such that the external energy depends on the system. Analogously, for the ground state, the total energy is given by:

$$E[\rho_0] = F[\rho_0] + \int \phi_0^*(\mathbf{r})\hat{V}\phi_0(\mathbf{r})d\mathbf{r} \ . \tag{2.20}$$

Applying the variational principle to equations 2.19 and 2.20 and taking into account the relations (2.18), we get:

$$\begin{aligned} E[\phi_0] &< E[\phi] \\ F[\rho_0] + \int \phi_0^*(\mathbf{r})\hat{V}\phi_0(\mathbf{r})d\mathbf{r} &< F[\rho] + \int \phi^*(\mathbf{r})\hat{V}\phi(\mathbf{r})d\mathbf{r} \ . \end{aligned} \tag{2.21}$$

As the electronic density defines the expected value of the external potential, then:

$$E[\rho_0] < E[\rho] \ . \tag{2.22}$$

□

Theorem 1 emphasizes that the external potential defines the density of the system, and theorem 2 introduces the uniqueness of the electronic density in the ground state.

2.2.2 Kohn-Sham Equations

The HK theorems state the possibility of describing the energy in the ground state as a functional of the density. Despite the Hartree potential presented in equation 2.8,

the other terms are not yet defined in terms of electronic density. The Kohn-Sham (KS) equations provide a way to solve the electronic problem in terms of density. The KS formulation of DFT is based on an *ansatz* that allows the replacement of the original interacting system with an auxiliary system of independent particles while maintaining the density of the interacting density.

From the universal functional defined in equation 2.19, it is useful to separate the classical Coulomb interaction:

$$F[\rho] = \frac{1}{2}\int\int \frac{\rho(\mathbf{r})\rho(\mathbf{r}')}{|\mathbf{r}-\mathbf{r}'|}d\mathbf{r}d\mathbf{r}' + G[\rho] \ , \tag{2.23}$$

thus, the total energy is given by:

$$E[\rho] = \int v(\mathbf{r})\rho(\mathbf{r})d\mathbf{r} + \frac{1}{2}\int\int \frac{\rho(\mathbf{r})\rho(\mathbf{r}')}{|\mathbf{r}-\mathbf{r}'|}d\mathbf{r}d\mathbf{r}' + G[\rho] \ , \tag{2.24}$$

where $G[\rho]$ is also a universal functional valid for any electronic system. Kohn and Sham proposed a form for this universal functional written as equation 2.25.

$$G[\rho] \equiv T_0[\rho] + E_{xc}[\rho] \ , \tag{2.25}$$

where T_0 represents the non-interaction kinetic energy and E_{xc} denotes the exchange-correlation energy, encompassing all quantum contributions neglected in previous terms in equations 2.24 and 2.25. Then, the functional of energy is given by:

$$E[\rho] = \int v(\mathbf{r})\rho(\mathbf{r})d\mathbf{r} + \frac{1}{2}\int\int \frac{\rho(\mathbf{r})\rho(\mathbf{r}')}{|\mathbf{r}-\mathbf{r}'|}d\mathbf{r}d\mathbf{r}' + T_0 + \int \rho(\mathbf{r})E_{xc}[\rho(\mathbf{r})]d\mathbf{r} \ . \tag{2.26}$$

From theorem 2, we can apply the HK variational principle with the constraint of the total number of electrons (N),

$$\int \rho(\mathbf{r})d\mathbf{r} = N, \rho(\mathbf{r}) = \sum_i |\phi_i(\mathbf{r})|^2 \ . \tag{2.27}$$

Thus:

$$\delta\left(E[\rho]-\mu\left[\int\rho(\mathbf{r})d\mathbf{r}-N\right]\right)=0\ ,$$
$$\int\delta\rho(\mathbf{r})\left\{\frac{\delta T_0}{\delta\rho}+v(\mathbf{r})+\int\frac{\rho(\mathbf{r}')}{|\mathbf{r}-\mathbf{r}'|}d\mathbf{r}'+V_{XC}[\rho]-\mu\right\}d\mathbf{r}=0\ , \tag{2.28}$$

where $V_{xc}[\rho]$ is given by:

$$V_{xc}[\rho]=\frac{\delta E_{xc}[\rho]}{\delta\rho}\ . \tag{2.29}$$

Evaluating T_0 using:

$$T_0=\sum_i\int\phi_i^*(\mathbf{r})\frac{\nabla^2}{2}\phi_i(\mathbf{r})d\mathbf{r}, \tag{2.30}$$

where ϕ_i represents the Kohn-Sham orbitals, it is possible to solve the single-particle Schrödinger equation:

$$\overbrace{\left(-\frac{\nabla^2}{2}+v^{KS}[\rho]\right)}^{\hat{H}KS}\phi i(\mathbf{r})=\epsilon_i\phi_i(\mathbf{r}), \tag{2.31}$$

where $v^{KS}[\rho]$ is the Kohn-Sham effective potential given by:

$$v^{KS}(\mathbf{r})=v(\mathbf{x})+\int\frac{\rho(\mathbf{r}')}{|\mathbf{r}-\mathbf{r}'|}d\mathbf{r}'+V_{XC}[\rho(\mathbf{r})]\ . \tag{2.32}$$

Equations 2.31 need to be solved using a self-consistent KS cycle method, as shown in Figure 2.1. The Kohn-Sham equations are solved as follows:

1. The cycle starts with the overlap of free-atom electronic ($\rho_i=\rho_0$) densities. During the non-self-consistent steps, the KS equations were solved without changing the initial electronic densities to give a good initial kick-start for KS wavefunctions.
2. During self-consistent steps, the electronic density of the previous step (ρ_i) mixes with a new (random) electronic density that generates ρ_{i+1}.
3. This electronic density determines the Kohn-Sham potential, using equation 2.32, which is used to solve the KS equation (equation 2.31).

4. The cycle continues until the convergence criteria of the cycle are reached, comparing the energy generated by the density at steps i and $i+1$

5. The cycle stops if the convergence is reached. The observables are calculated with the electronic density and wave function that minimizes the total energy. Steps 2 and 4 are repeated during structural optimization until the optimized structure is reached.

Figure 2.1 displays the KS self-consistent cycle, illustrating the steps mentioned above.

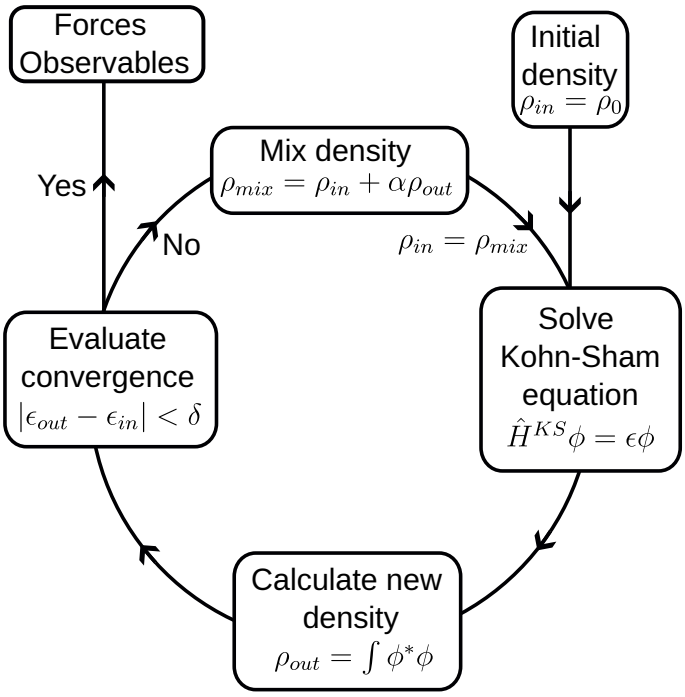

Figure 2.1: Kohn-Sham self-consistent cycle which is used for solving the Kohn-Sham equations iteratively [source: own authorship].

2.2.3 Approximations to the Exchange-Correlation Functional

In principle, the Kohn-Sham formulation of the DFT is formally equivalent to the Schrödinger equation for an electronic system[97]. However, the analytical form of the XC functional in equation 2.26 is unknown, thus, defining a form for this term has several important contributions and is a subject of study ultil now. A simple approximation called the local density approximation[98] (LDA) defines this term as

for a homogeneous electron gas in each site:

$$E_{XC}^{\mathrm{LDA}} = \int \epsilon_{XC}^{LDA}[\rho(\mathbf{r})]d\mathbf{r} \ , \tag{2.33}$$

where $\epsilon_{XC}^{\mathrm{LDA}}$ represents the XC energy for a homogeneous electron gas with density ρ. From equation 2.29:

$$V_{XC}^{\mathrm{LDA}} \equiv \frac{d}{d\rho(\mathbf{r})}\left(\rho(\mathbf{r})\epsilon_{XC}^{\mathrm{LDA}}[\rho(\mathbf{r})]\right) \ . \tag{2.34}$$

In LDA, $\epsilon_{XC}^{\mathrm{LDA}}$ can be decomposed as the sum of exchange and correlation contributions, where the exchange energy for a uniform gas is analytically known:

$$\epsilon_{X}^{\mathrm{LDA}}(\rho(\mathbf{r})) = -\frac{3k_F(\rho(\mathbf{r}))}{4\pi}, \tag{2.35}$$

where $k_F(\rho(\mathbf{r})) = (3\pi^2\rho(\mathbf{r}))^{1/3}$ represents the Fermi wave number. Different parameterizations define the correlation part, based on quantum Monte Carlo simulations, such as the one proposed by Perdew and Wang[99].

Despite the simplicity of the XC energy given by equation 2.33, it fails to describe systems with a larger non-uniform electronic density. A refinement of LDA considers the XC energy not only by the local density but also by considering the gradient of the density. This is called the Generalized Gradient Approximation (GGA). The general form of the GGA is:

$$E_{XC}^{\mathrm{GGA}}[\rho] = \int f(\rho(\mathbf{r}), \nabla\rho(\mathbf{r}))d\mathbf{r} \ . \tag{2.36}$$

In this work, we use the parametrization of the GGA functional proposed by Perdew, Burke, and Ernzerhof (PBE)[100]. In the PBE, the exchange energy calculates as:

$$E_{X}^{\mathrm{PBE}} = \int \rho(\mathbf{r})\epsilon_{X}^{\mathrm{LDA}}(\rho(\mathbf{r}))F_X(s)d\mathbf{r} \ , \tag{2.37}$$

where equation 2.35 calculates the term $\epsilon_{X}^{\mathrm{LDA}}(\rho(\mathbf{r}))$, $s = \frac{|\nabla\rho(\mathbf{r})|}{2\rho(\mathbf{r})k_F(\rho(\mathbf{r}))}$ is a dimensionless gradient of density, and F_X is calculates as

$$F_X(s) = 1 + \kappa - \frac{\kappa}{1 + \mu s^2/\kappa} \ . \tag{2.38}$$

PBE functional defines the coefficients as $\kappa = 0.804$ and $\mu = 0.21951$. The parameter F_X scales the exchange energy given by the LDA XC energy, which was obtained by evaluating the asymptotic limits.

Now, the correlation part of PBE is written as:

$$E_C^{\mathrm{PBE}} = \int \rho(\mathbf{r})[\epsilon_c^{\mathrm{LDA}}(r_s) + H(r_s, t)]d\mathbf{r} \ , \tag{2.39}$$

where,

$$H(r_s, t) = \gamma \ln\left[1 + \frac{\beta}{\gamma}t^2\left(\frac{1 + At^2}{1 + At^2 + A^2t^4}\right)\right] \ . \tag{2.40}$$

In the preceding equation, r_s is the Wigner-Seitz radius, $t = \frac{|\nabla\rho(\mathbf{r})|}{2\rho(\mathbf{r})r_s(\rho(\mathbf{r}))}$ and,

$$A = \frac{\beta}{\gamma}\left[\exp\{\frac{-\epsilon_c^{\mathrm{LDA}}}{\gamma}\} - 1\right]^{-1}, \gamma = \frac{(1 - \ln(2))}{\pi^2} \ , \tag{2.41}$$

with the parameters β and $\epsilon_c^{\mathrm{LDA}}$ given by Perdew and Wang for LDA correlation.

The so-called local (LDA) or semilocal (GGA) suffers from a problem called self-interaction error (SIE). The SIE becomes apparent when analyzing the Hartree energy:

$$E_H = \frac{1}{2}\int\int \frac{\rho(\mathbf{r})\rho(\mathbf{r}')}{|\mathbf{r} - \mathbf{r}'|}d\mathbf{r}d\mathbf{r}' \ . \tag{2.42}$$

When solving the KS equations, the density given by $\rho(\mathbf{r}) = \sum_n \phi_n^*(\mathbf{r})\phi_n(\mathbf{r})$ can be replaced in previous equation resulting in:

$$E_H = \frac{1}{2}\sum_n\sum_m\int\int \frac{\phi_n^*(\mathbf{r})\phi_n(\mathbf{r})\phi_m^*(\mathbf{r}')\phi_m(\mathbf{r}')}{|\mathbf{r} - \mathbf{r}'|}d\mathbf{r}d\mathbf{r}' \ , \tag{2.43}$$

where n and m index the KS eingenstate. We note that if $n = m$, the contribution is:

$$E_H = \frac{1}{2}\int\int \frac{\rho(\mathbf{r})\rho(\mathbf{r}')}{|\mathbf{r} - \mathbf{r}'|} \ . \tag{2.44}$$

The equation 2.44 shows the self-interaction, that is, the interaction of the electron

with itself. For correct XC energy the energy in equation 2.44 should cancel exactly,

$$E_{XC} - E_H = 0 \ , \tag{2.45}$$

however, for the local and semilocal XC functionals, as in the case of PBE and LDA, the previous equation is not zero, this is the self-interaction error.

Although the PBE approximation to the XC energy can provide several properties, such as structural properties and binding energies, it tends to underestimate the band gap compared to experimental results[101]. Thus, since this work focuses on semiconductor applications, accurately describing the band gap is essential. One proposal to reduce the SIE includes incorporating part of the exact exchange energy from the Hartree-Fock (HF) theory,

$$E_X^{\mathrm{HF}} = \frac{-1}{2} \int\int \sum_{n,m} \frac{\phi_n^*(\mathbf{r})\phi_m^*(\mathbf{r}')\phi_n(\mathbf{r}')\phi_m(\mathbf{r})}{|\mathbf{r}-\mathbf{r}'|} d\mathbf{r}d\mathbf{r}' \ , \tag{2.46}$$

on the KS total energy, which is called a hybrid functional. Here, we choose the proposal of Heyd, Scuseria, and Ernzerhof (HSE06) that includes only the short range of E_X^{HF}, that is, splitting the bare Coulomb operator into short- (SR) and long-range (LR)

$$\frac{1}{|\mathbf{r}-\mathbf{r}'|} = \frac{\overbrace{erfc(\omega|\mathbf{r}-\mathbf{r}'|)}^{SR}}{\mathbf{r}-\mathbf{r}'} + \frac{\overbrace{erf(\omega|\mathbf{r}-\mathbf{r}'|)}^{LR}}{\mathbf{r}-\mathbf{r}'} \ , \tag{2.47}$$

where ω is an adjustable parameter that gives the range of interaction. Then, the mix of the short- and long-range exchange energy of PBE and HSE06 is as follows.

$$E_{XC}^{\mathrm{HSE06}} = \alpha E_X^{\mathrm{HF,\ SR}}(\omega) + (1-\alpha)E_{XC}^{\mathrm{PBE,\ SR}}(\omega) + E_X^{\mathrm{PBE,\ LR}}(\omega) + E_C^{PBE} \ , \tag{2.48}$$

with the constants $\alpha = 1/4$ and $\omega = 0.2\mathring{\mathrm{A}}^{-1}$. HSE06 provides an accurate band gap compared to other approximations to the XC term, with a reliable computational cost, and will be used to correct the band gap of the systems, as explained in section 3.4.2.

2.3 Crystalline Periodic Systems

This dissertation investigates crystalline systems, that is, structures that are repeated periodically in space. The set of points that repeat periodically in space is called a Bravais lattice, where each point can have an atom, a molecule, or, generically, a basis where the crystal structure can be represented by the symbolic formula: Crystal = Bravais lattice + Basis, as depicts in figure 2.2. The Bravais lattice consists of all points that follow the condition:

$$\mathbf{R} = n_1\mathbf{a}_1 + n_2\mathbf{a}_2 + n_3\mathbf{a}_3 \ , \tag{2.49}$$

with $n_{1,2,3}$ integers and $\mathbf{a}_1$, $\mathbf{a}_2$ and $\mathbf{a}_3$ been the direct lattice vectors of structure.

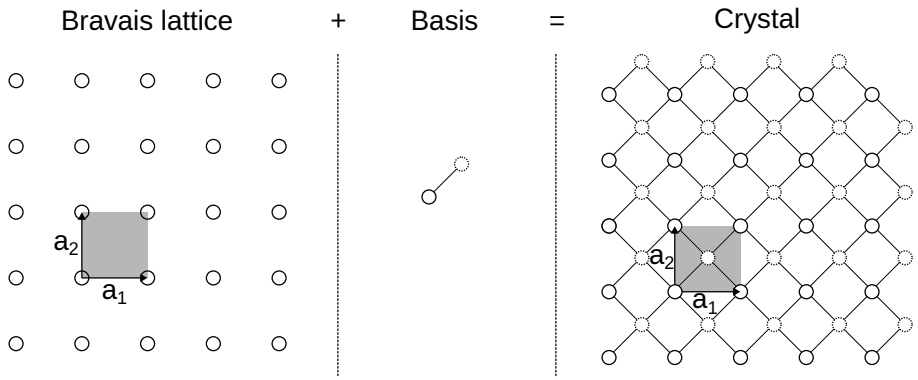

Figure 2.2: Simplified representation of a Crystal in 2D. The left panel represents a represents a Bravais lattice defined by the lattice parameters $\mathbf{a}_1$ and $\mathbf{a}_2$. The gray area represents the unit cell. When a basis (center panel) is positioned in each point of the Bravais lattice the crystal is constructed (right panel). [source: own authorship]

In these crystalline systems, the basic repetition unit is the **unit cell**, where, by translation of the unit cell, the crystal is constructed. There is no unique definition of unit cell, as depicted in figure 2.3. So, we can define the **primitive unit cell** (for simplicity referred to here as the unit cell) as *the volume defined by the lattice vectors that contains only one Bravais lattice point*[1] which is a basic repeat structure in a Bravais lattice. Furthermore, the **Wigner-Seitz** cell is a possible choice of the primitive cell and is defined by Voronoi decomposition, as depicted in figure 2.3.

[1]It seems that in the left panel of figure 2.2 contains more than one point, but each point is shared with neighboring cells; thus, each point contributes to $\frac{1}{4}$ totaling 1.

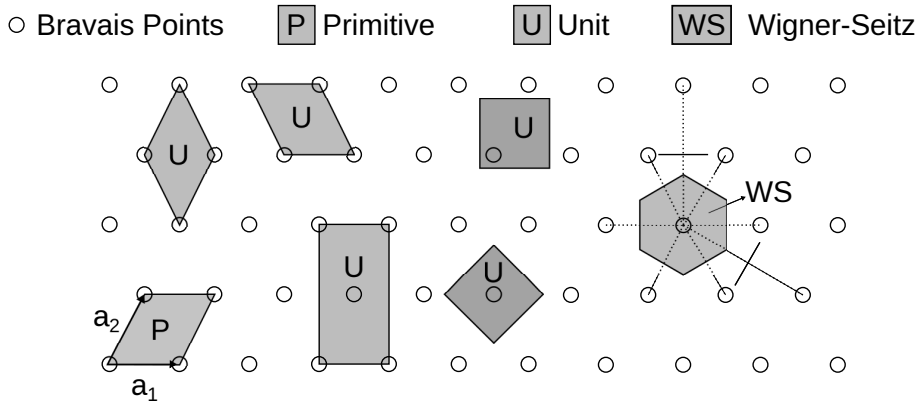

Figure 2.3: Different Definitions of zones in the real space. [source: own authorship]

Translation symmetry follows the condition that all points in the crystal can be generated through $\mathbf{r}' = \mathbf{r} + \mathbf{R}$, where $\mathbf{r}$ is a position in the unit cell. At the crystal periodicity, an observable also needs to have this periodicity. Consider, for example, the electronic density $\rho(\mathbf{r})$ in the unit cell,

$$\rho(\mathbf{r} + \mathbf{R}) = \rho(\mathbf{r}) \ , \tag{2.50}$$

with $\mathbf{R}_n$ given by equation 2.49. This periodicity ensures the possibility of using plane-wave expansions via Fourier analysis, that is,

$$\rho(\mathbf{r}) = \sum_{\mathbf{G}} \rho_{\mathbf{G}} e^{i\mathbf{G}\cdot\mathbf{r}} \tag{2.51}$$

and, as required by equation 2.50 we must have,

$$\sum_{\mathbf{G}} \rho_{\mathbf{G}} e^{i\mathbf{G}\cdot\mathbf{r}} = \sum_{\mathbf{G}} \rho_{\mathbf{G}} e^{i\mathbf{G}\cdot(\mathbf{r}+\mathbf{R})} = \sum_{\mathbf{G}} \rho_{\mathbf{G}} e^{i\mathbf{G}\cdot\mathbf{R}} e^{i\mathbf{G}\cdot\mathbf{r}} \ , \tag{2.52}$$

which is satisfied if $e^{i\mathbf{G}\cdot\mathbf{R}} = 1$, thus, $\mathbf{G}\cdot\mathbf{R} = 2\pi N$, with N integer. The vector $\mathbf{G}$ can be chosen as a combination of reciprocal lattice vectors ($\mathbf{b}_1$, $\mathbf{b}_2$ and $\mathbf{b}_3$), that is,

$$\mathbf{G} = m_1\mathbf{b}_1 + m_2\mathbf{b}_2 + m_3\mathbf{b}_3 \ , \ m_1, \ m_2, \text{ and } m_3 \text{ integers} \ , \tag{2.53}$$

where,

$$\mathbf{b}_1 = 2\pi \frac{\mathbf{a}_2 \times \mathbf{a}_3}{\mathbf{a}_1 \cdot (\mathbf{a}_2 \times \mathbf{a}_3)} \ , \mathbf{b}_2 = 2\pi \frac{\mathbf{a}_3 \times \mathbf{a}_1}{\mathbf{a}_1 \cdot (\mathbf{a}_2 \times \mathbf{a}_3)} \ , \mathbf{b}_3 = 2\pi \frac{\mathbf{a}_1 \times \mathbf{a}_2}{\mathbf{a}_1 \cdot (\mathbf{a}_2 \times \mathbf{a}_3)} \ . \tag{2.54}$$

The coefficients in equation 2.51 expands as taking the inverse Fourier transform as

$$\rho_{\mathbf{G}} = \frac{1}{\Omega_{cell}} \int_{cell} dV \rho(\mathbf{r}) e^{-i\mathbf{G}\cdot\mathbf{r}} \ , \tag{2.55}$$

where *cell* stands for the cell defined by the lattice vectors in real space while Ω_{cell} is the volume, calculated as:

$$\Omega_{cell} = \mathbf{a}_1 \cdot (\mathbf{a}_2 \times \mathbf{a}_3) \ . \tag{2.56}$$

Another important concept is the Brillouin Zone (BZ), which is defined as the Wigner-Seitz cell in reciprocal space, with the construction exemplified in the figure 2.3. Then, we denote a vector inside the BZ by $\mathbf{k}$.

In crystalline systems, the nuclei generate a periodic potential that electrons are subject to the form

$$V(\mathbf{r} + \mathbf{R}) = V(\mathbf{r}) \ , \tag{2.57}$$

with $\mathbf{r}$ been a coordinate and $\mathbf{R}$ a translation with respect of lattice vectors. The goal here is thus to solve a Schrodinger equation with potential subject to the condition in equation 2.57, that is,

$$\left[-\frac{\nabla^2}{2} + V(\mathbf{r}) \right] \psi = \epsilon \psi \ . \tag{2.58}$$

The Bloch theorem[102,103] give the solutions for those systems:

Theorem 3. *The eigenstates ψ of the one-electron Hamiltonian in equation 2.58 subject to the condition 2.57 far all $\mathbf{R}$ in a Bravais lattice, can be chosen to have the form of a plane wave times the periodicity of the Bravais lattice:*

$$\psi_{n\mathbf{k}}(\mathbf{r}) = e^{i\mathbf{k}\cdot\mathbf{r}} u_{n\mathbf{k}}(\mathbf{r}) \ , \tag{2.59}$$

$$u_{n\mathbf{k}}(\mathbf{r} + \mathbf{R}) = u_{n\mathbf{k}}(\mathbf{r}) \tag{2.60}$$

where, n indexes the band and $\mathbf{k}$ is a vector within the BZ.

In DFT, we can apply the Bloch theorem, such as the KS orbitals written as:

$$\phi_{n\mathbf{k}}(\mathbf{r}) = e^{i\mathbf{k}\cdot\mathbf{r}} u_{n\mathbf{k}}(\mathbf{r}) \tag{2.61}$$

and, as $u_{n\mathbf{k}}(\mathbf{r})$ must have the same periodicity of the lattice, this suggests the possibility of employing plane wave expansion,

$$u_{n\mathbf{k}}(\mathbf{r}) = \sum_{\mathbf{G}} c_{n\mathbf{k}}(\mathbf{G}) e^{i\mathbf{G}\cdot\mathbf{r}} \ , \tag{2.62}$$

where, the sum goes for a set of $\mathbf{G}$ satisfying the relation,

$$\frac{1}{2}|\mathbf{k}+\mathbf{G}|^2 < E_{cutoff} \ . \tag{2.63}$$

In the previous equation, E_{cutoff} is the cut-off energy for the set of plane waves. When using the Bloch orbitals in the KS equation, the effective potential (equation 2.32) can be described in terms of the Fourier transform,

$$v_{eff}(r) = \sum_{\mathbf{G}} e^{i\mathbf{G}\cdot\mathbf{r}} \tilde{v}_{eff}(\mathbf{G}) \ , \tag{2.64}$$

where the effective potential in reciprocal space transforms from real space as,

$$\tilde{v}_{eff}(\mathbf{G}) = \frac{1}{\Omega}\int_{\Omega} v_{eff}(\mathbf{r}) e^{-i\mathbf{G}\cdot\mathbf{r}} d\mathbf{r} \ . \tag{2.65}$$

Finally, the coefficients of equation 2.62 and the energy bands ($\epsilon_{n\mathbf{k}}$) are obtained by solving the Kohn-Sham equation in reciprocal space,

$$\sum_{\mathbf{G}'} \left[\frac{1}{2}|\mathbf{k}+\mathbf{G}|^2 \delta_{\mathbf{G}\mathbf{G}'} + \tilde{v}_{eff}(\mathbf{G}-\mathbf{G}')\right] c_{n\mathbf{k}}(\mathbf{G}') = \epsilon_{n\mathbf{k}} c_{n\mathbf{k}}(\mathbf{G}) \ . \tag{2.66}$$

2.3.1 Projector Augmented Wave Method

The description of core electrons using plane-wave expansion, as shown in the previous section, is computationally expensive because of the rapid oscillations of wave functions near the nuclei. Moreover, in many solid calculations, the core electrons have little influence on some properties, such as atomic binding and the interaction with light with matter. The Projector Augmented Wave Method (PAW) method emerges as an approximation, motivated by ultra-soft pseudopotentials [104,105] (USPP) and linearized augmented plane wave [106] (LAPW), as an approximation to a computationally efficient evaluation of electronic states of valence without computational cost to describe core electrons.

In the PAW method, all electron (AE) wave functions $\psi_{n\mathbf{k}}$ are constructed by a linear transformation (T) based on smooth pseudo functions (PS) $\tilde{\psi}_{n\mathbf{k}}$ that act only within a spherical augmented region (Ω_α) centered on each atomic site (α). Outside of those augmented regions (interstitial), both AE and PS wave functions must coincide. A transformation satisfying these conditions can be written as:

$$\begin{aligned} |\psi_{n\mathbf{k}}\rangle &= \mathrm{T}|\tilde{\psi}_{n\mathbf{k}}\rangle \ , \\ \mathrm{T} &= \mathbb{1} + \sum_i (|\phi_i\rangle - |\tilde{\phi}_i\rangle)\langle\tilde{p}_i| \ , \end{aligned} \tag{2.67}$$

where ϕ_i is the AE partial wave function which is solutions for an isolated atom, and $\tilde{\phi}_i$ is the PS partial wave function which is equal to the AE partial wave function in the interstitial region and matches continuously with ϕ_i inside the augmented regions. The projection functions $\tilde{p}_i$ are dual of the partial wave function outside of the augmented region:

$$\langle\tilde{p}_i|\tilde{\phi}_j\rangle = \delta_{ij} \ . \tag{2.68}$$

Then, the all-electron wavefunction is written as:

$$|\psi_{n\mathbf{k}}\rangle = |\tilde{\psi}_{n\mathbf{k}}\rangle + \sum_i (|\phi_i\rangle - |\tilde{\phi}_i\rangle)\langle\tilde{p}_i|\tilde{\psi}_{n\mathbf{k}}\rangle \ . \tag{2.69}$$

Here, we also explore the frozen core approximation, where the core electrons are kept frozen from the generated PAW projector. Figure 2.4 presents a schematic representation of the PAW method.

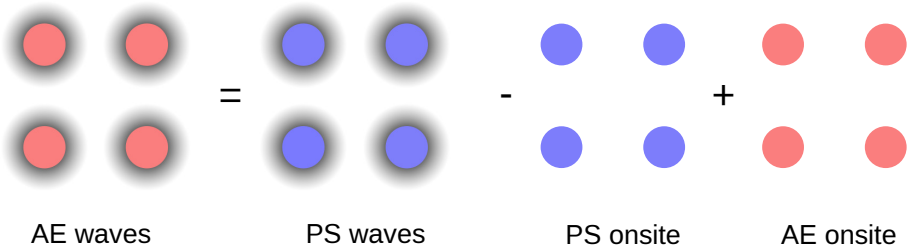

Figure 2.4: Schematic representation of the PAW method. [source: own authorship]

2.4 Spin-Orbit Coupling

In the preceding sections of this chapter, relativistic effects were neglected. Relativity is of fundamental importance for describing heavy elements in the crystal structure, notably in the vicinity of the nuclei[97]. This work employs spin-orbit coupling (SOC) to include relativistic effects in the study of electronic properties and their impact on excitonic properties, as pointed out in other works[107,108]. We did not include SOC effects in the calculation of structural properties due to their low impact on determining the optimized structure[109].

In our treatment, using the PAW method, SOC is included through perturbation theory, with SOC energy given by[110]:

$$H_{\mathrm{SOC}}^{\alpha\beta} = \frac{\hbar}{(2m_e c)^2} \frac{K(r)}{r} \frac{dV(r)}{dr} \vec{\sigma}^{\alpha\beta} \cdot \mathbf{L}, \tag{2.70}$$

where $\mathbf{L} = \mathbf{r} \times \mathbf{p}$, $\vec{\sigma}$ are the Pauli matrices, $V(r)$ describes the spherical part of the effective all-electron potential inside the PAW spheres, and

$$K(r) = \left(1 - \frac{V(r)}{2m_e c^2}\right)^{-2}, \tag{2.71}$$

with m_e being the electron mass and c the speed of light in the vacuum. The inclusion of SOC causes splitting in the band structure due to the break of degeneracy in some parts of the band structure caused by the effect of nuclei on electrons. Its inclusion possibly impacts the band gap and will be taken into account to correct the band gap.

2.5 Tight Binding Calculations

The tight-binding (TB) method consists of describing the electronic structure by overlapping the individual atomic orbitals to describe the electronic states in a crystal. For an insulating material, the overlap between atomic states is low, which is opposite to the case for an insulating material, where the overlap is large and tends to drastically modify the individual atomic levels. However, semiconductor materials have localized atomic levels with low overlap of valence states. Thus, the TB method is reliable for describing semiconductors, where the overlap of atomic orbitals is not big enough to require dramatic change in individual atomic levels,

but corrections are needed to better describe the interaction of valence states with neighboring atoms.

We start constructing a linear combination of localized atomic orbitals $\chi_\mu(\mathbf{r}-\mathbf{R})$, satisfying the Bloch theorem (theorem 3):

$$\phi_\mu(\mathbf{k},\mathbf{r}) = \frac{1}{\sqrt{N}}\sum_{\mathbf{R}} e^{i\mathbf{k}\cdot\mathbf{R}}\chi_\mu(\mathbf{r}-\mathbf{R}-\tau_\alpha) \ , \tag{2.72}$$

where, R indexes the atomic site and τ_α the atomic site for systems with more than one atom per unit cell. For simplicity, let us consider only one atom per unit cell, in this case previous equation is written as:

$$\phi_\mu(\mathbf{k},\mathbf{r}) = \frac{1}{\sqrt{N}}\sum_{R} e^{i\mathbf{k}\cdot\mathbf{R}}\chi_\mu(\mathbf{r}-\mathbf{R}) \ , \tag{2.73}$$

The elements of a given Hamiltonian $\hat{H}(\mathbf{r}) = \hat{H}(\mathbf{r}+\mathbf{R})$, using the previous function are evaluated as:

$$\begin{aligned} H_{\mu\nu}(\mathbf{k}) &= \int \phi^*_\mu(\mathbf{k},\mathbf{r})\hat{H}\phi_\nu(\mathbf{k},\mathbf{r})d\mathbf{r} \ , \\ &= \frac{1}{N}\sum_{\mathbf{R},\mathbf{R}'} e^{i\mathbf{k}\cdot(\mathbf{R}-\mathbf{R}')}\int \chi^*_\mu(\mathbf{r}-\mathbf{R})\hat{H}\chi_\nu(\mathbf{r}-\mathbf{R}')d\mathbf{r} \ , \end{aligned} \tag{2.74}$$

and, by translation symmetry:

$$H_{\mu\nu}(\mathbf{k}) = \sum_{\mathbf{R}''} e^{i\mathbf{k}\cdot\mathbf{R}''} \overbrace{\int \chi^*_\mu(\mathbf{r})\hat{H}\chi_\nu(\mathbf{r}-\mathbf{R}'')d\mathbf{r}}^{h_{\mu\nu}(\mathbf{R}'')} \ . \tag{2.75}$$

Since the atomic wave functions ϕ are not orthogonals[111], the matrix elements of overlap between wave functions are constructed as follows:

$$S_{\mu\nu}(\mathbf{k}) = \sum_{\mathbf{R}''} e^{i\mathbf{k}\cdot\mathbf{R}''}\int \chi^*_\mu(\mathbf{r})\chi_\nu(\mathbf{r}-\mathbf{R}'')d\mathbf{r} \ . \tag{2.76}$$

If we construct the Bloch wave functions as a linear combination of atomic wave

functions, as they respect the Bloch theorem, as:

$$\psi_n(\mathbf{k},\mathbf{r}) = \sum_{\mu} C_{n\mu}(\mathbf{k})\phi_{\mu}(\mathbf{k},\mathbf{r}) \ , \tag{2.77}$$

The energy of n-th eigenstate is calculated as:

$$E_n(\mathbf{k}) = \frac{\int \psi_n^*(\mathbf{k},\mathbf{r})\hat{H}\psi_{n'}(\mathbf{k},\mathbf{r})d\mathbf{r}}{\int \psi_n^*(\mathbf{k},\mathbf{r})\psi_{n'}(\mathbf{k},\mathbf{r})d\mathbf{r}} \ . \tag{2.78}$$

Now, replacing the eingenstates 2.77 in 2.78,

$$\begin{aligned} E_n(\mathbf{k}) &= \frac{\int \sum_{\mu,\nu} C_{n\mu}^*(\mathbf{k})C_{n\nu}(\mathbf{k})\phi_{\mu}^*(\mathbf{k},\mathbf{r})\hat{H}\phi_{\nu}(\mathbf{k},\mathbf{r})d\mathbf{r}}{\int \sum_{\mu,\nu} C_{n\mu}^*(\mathbf{k})C_{n\nu}(\mathbf{k})\phi_{\mu}^*(\mathbf{k},\mathbf{r})\phi_{\nu}(\mathbf{k},\mathbf{r})d\mathbf{r}} \ , \\ &= \frac{\sum_{\mu,\nu} C_{n\mu}^*(\mathbf{k})C_{n\nu}(\mathbf{k})H_{\mu\nu}(\mathbf{k})}{\sum_{\mu,\nu} C_{n\mu}^*(\mathbf{k})C_{n\nu}(\mathbf{k})S_{\mu\nu}(\mathbf{k})} \end{aligned} \tag{2.79}$$

as defined in equations 2.75 and 2.76. These equations are fixed, since they were constructed based on atomic orbitals, then the solution of equation 2.79 is given by the equation:

$$\sum_{\nu} \left[H_{\mu\nu}(\mathbf{k}) - E_n(\mathbf{k})S_{\mu\nu}(\mathbf{k})\right] C_{n\nu}(\mathbf{k}) = 0 \ . \tag{2.80}$$

2.5.1 Wannier Interpolation

The Wannier functions[38] are an orthogonal complete basis set of localized functions in the real space for crystalline systems. The study of excitonic and optical properties of the present work employs the tight-binding model, where, the electronic structure is obtained by employing density functional theory and further parameterized using Maximally Localized Wannier functions[112] (MLWF).

A set of N isolated Bloch bands $\psi_{n\mathbf{k}}(\mathbf{r})$, as presented in theorem 3, can be linked to a set of N Wannier functions $w_{n\mathbf{R}}(\mathbf{r}) = w_n(\mathbf{r}-\mathbf{R})$ by the transformation:

$$|n\mathbf{R}\rangle = |w_{n\mathbf{R}}\rangle = \frac{V}{(2\pi)^3}\int_{BZ}\left[\sum_{m=1}^{N} U_{mn}^{(\mathbf{k})}|\psi_{m\mathbf{k}}\rangle\right] e^{-i\mathbf{k}\cdot\mathbf{R}}d\mathbf{k} \ , \tag{2.81}$$

where, V is the volume of the unit cell in real space, and the integration is taken in the Brillouin Zone in reciprocal space. Similarly, the transformation of a set of

entangled bands is written as:

$$|n\mathbf{R}\rangle = |w_{n\mathbf{R}}\rangle = \frac{V}{(2\pi)^3}\int_{BZ}\left[\sum_{m=1}^{N} U_{mn}^{(\mathbf{k})}|\psi_{m\mathbf{k}}\rangle\right] e^{-i\mathbf{k}\cdot\mathbf{R}} d\mathbf{k} \ . \tag{2.82}$$

In the above equations, $U_{mn}^{(\mathbf{k})}$ ($U_{mn}^{dis(\mathbf{k})}$) is a unitary transformation that mixes several bands in the wave vector $\mathbf{k}$. Because of the freedom in the choice of the unitary transformation $U_{mn}^{(\mathbf{k})}$ ($U_{mn}^{dis(\mathbf{k})}$), the Wannier functions for a set of Bloch states in non-unique with leaves to a different spread of Wannier states. The MLWF approach consists of choosing this unitary transformation that minimizes the sum of the quadratic spread of the Wannier states about its centers, that is,

$$\Omega = \sum_{n}\left[\langle \mathbf{0}n|r^2|\mathbf{0}n\rangle - \langle \mathbf{0}n|\mathbf{r}|\mathbf{0}n\rangle^2\right] \tag{2.83}$$

Now, having determined the set of Wannier states for the band structure, the representation of a Hamiltonian operator in these states is written as:

$$H^{(w)}(\mathbf{k}) = (U^{(\mathbf{k})})^{\dagger}(U^{dis(\mathbf{k})})^{\dagger}H(\mathbf{k})U^{(\mathbf{k})}U^{dis(\mathbf{k})} \ , \tag{2.84}$$

where, $H_{nm}(\mathbf{k}) = \epsilon_{n\mathbf{k}}\delta_{nm}$.

2.6 Excitonic and optical Properties

The excitonic and optical properties in this work were calculated using the TB Hamiltonian parameterized by the MLWF based on the electronic structure obtained by the DFT. This section presents the Bethe-Salpeter equation (BSE) formalism to calculate the excitonic properties as the optical calculation in both, IPA and BSE frameworks.

2.6.1 Bethe-Salpeter Equation

We start the derivation of the Bethe-Salpeter equation with a description of the excitations in semiconducting systems considering a two-band model. The ground

state constructs as:

$$|\phi_0\rangle = \sum_{\mathbf{k}} \prod_{v=1}^{N} c^{\dagger}_{\mathbf{k}v}|0\rangle \ = |FS\rangle \ , \tag{2.85}$$

with $\mathbf{k}$ sum over the first BZ, v runs over the number of electrons, where $|0\rangle$ is the vacuum state. Then, a single-particle excitation is created annihilating an electron in valence (v) and creating in the conduction (c) band, that is:

$$|\phi_X\rangle = c^{\dagger}_{\mathbf{k}c} c_{\mathbf{k}v}|FS\rangle \otimes |0\rangle^{\otimes M} \ , \tag{2.86}$$

where, $b^{\dagger}_{\mathbf{k},cv}$ is the creation operator of a single particle excitation in a specific $\mathbf{k}-$point. Similarly, $b_{\mathbf{k},cv}$ annihilates a single-particle excitation. Throughout this dissertation, we do not consider indirect (phonon-assisted) transitions because we want to describe optically excited states. In addition to that, other possible exciton complexes, such as biexcitons and trions, are not described.

From equation 2.86, we construct a basis of single excitation, in Tamm-Dancoff approximation (TDA) as:

$$\{|\phi_X\rangle\} = \sum_{v=1}^{N} \sum_{c=1}^{M} \sum_{\mathbf{k}} c^{\dagger}_{\mathbf{k}c} c_{\mathbf{k}v}|FS\rangle \otimes |0\rangle^{\otimes M} \ , \tag{2.87}$$

for N valence and M conduction states. We use this basis of single excitations for expanding the exciton eigenstates:

$$|X_{\mathbf{k}cv}\rangle = |\mathbf{k}cv\rangle = A^{(n)}_{\mathbf{k}cv} c^{\dagger}_{\mathbf{k}c} c_{\mathbf{k}v}|FS\rangle \otimes |0\rangle^{\otimes M} \ . \tag{2.88}$$

where, n is the n-th excitonc states in $\mathbf{k}-$point.

After defining a basis for such excited states, we need to solve the eigenvalue problem:

$$\langle \mathbf{k}' c' v'|\hat{H}_e|\mathbf{k}cv\rangle A^{(n)}_{\mathbf{k},cv} = A^{(n)}_{\mathbf{k},cv} E^{(n)}_{cv} \ , \tag{2.89}$$

with $E^{(n)}_{cv}$ being the n-th exciton eigenvalue between band v and c, and $\hat{H}_X$ the excitonic Hamiltonian, that we construct as containing the electrons and holes one-

particle operator and the Coulomb between both:

$$\hat{H}_e = \sum_{\mathbf{k}} \left[\overbrace{\epsilon_{\mathbf{k}v} c^{\dagger}_{\mathbf{k}v} c_{\mathbf{k}v} + \epsilon_{\mathbf{k}c} c^{\dagger}_{\mathbf{k}c} c_{\mathbf{k}c}}^{\hat{H}^{(1)}_X} + \overbrace{\sum_{\mathbf{k}'} V^{\mathbf{k},\mathbf{k}'}_{vcv'c'}}^{\hat{H}^{(2)}_X} \right] , \tag{2.90}$$

where, $\epsilon_{\mathbf{k}v(c)}$ is the eigenvalue in the valence (conduction) band, and $V^{\mathbf{k},\mathbf{k}'}_{c,v}$ is the Coulomb interaction term. The equation 2.89 evaluated with the Hamiltonian 2.90 leads to the Bethe-Salpeter equation[113] (BSE):

$$(E_{c,\mathbf{k}} - E_{v,\mathbf{k}}) A^{(n)}_{\mathbf{k}cv} + \frac{1}{\Omega_{BZ}} \sum_{\mathbf{k}'v'c'} W_{(\mathbf{k},v,c),(\mathbf{k}',v',c')} A^{(n)}_{\mathbf{k}'c'v'} = E^{(n)}_{cv} A^{(n)}_{\mathbf{k}cv} \, . \tag{2.91}$$

2.6.2 Light-Matter Interaction

The optical properties are studied through the real (re) and imaginary (img) parts of dielectric tensor[51], which in the scope of independent particle approximation (IPA) writes as:

$$\epsilon_{(\mathrm{re}),\alpha,\beta}(\omega) = \delta_{\alpha,\beta} + \frac{e^2}{\epsilon_0 \Omega N_{\mathbf{k}}} \sum_{\mathbf{k},c,v} F^{c,v,\mathbf{k}}_{\alpha,\beta} \frac{(E_{c,\mathbf{k}} - E_{v,\mathbf{k}}) - \hbar\omega}{(\hbar\omega - (E_{c,\mathbf{k}} - E_{v,\mathbf{k}}))^2 + \eta^2} \, , \tag{2.92}$$

$$\epsilon_{(\mathrm{img}),\alpha,\beta}(\omega) = \frac{e^2}{\epsilon_0 \Omega N_{\mathbf{k}}} \sum_{\mathbf{k},c,v} F^{c,v,\mathbf{k}}_{\alpha,\beta} \frac{\eta}{(\hbar\omega - (E_{c,\mathbf{k}} - E_{v,\mathbf{k}}))^2 + \eta^2} \, , \tag{2.93}$$

where, α (β) is the direction of incident radiation (x, y or z), ϵ_0 the dielectric constant in vacuum, Ω the volume of the unit cell, $N_{\mathbf{k}}$ the number of $\mathbf{k}$-points in reciprocal space, η a smooth factor and $F^{c,v,\mathbf{k}}_{\alpha,\beta}$ the oscillator force defined as,

$$F^{c,v,\mathbf{k}}_{\alpha,\beta} = \frac{\langle c,\mathbf{k}|P_\alpha|v,\mathbf{k}\rangle \langle v,\mathbf{k}|P_\beta|c,\mathbf{k}\rangle}{(E_{c,\mathbf{k}} - E_{v,\mathbf{k}} - i\eta)(E_{c,\mathbf{k}} - E_{v,\mathbf{k}} + i\eta)} \, , \tag{2.94}$$

with $P_{\alpha(\beta)}$ been the light-matter operator given by: $P_\alpha = \frac{\partial H(\mathbf{k})}{\partial k_\alpha}$.

In the context of BSE, the real and imaginary parts of the dielectric tensor are

calculated as:

$$\epsilon_{(\mathrm{re}),\alpha,\beta}(\omega) = \delta_{\alpha,\beta} + \frac{e^2}{\epsilon_0 \Omega N_{\mathbf{k}}} \sum_n F^n_{\alpha,\beta} \frac{E^{(n)}_{cv} - \hbar\omega}{(\hbar\omega - E^{(n)}_{cv})^2 + \eta^2} \ , \tag{2.95}$$

$$\epsilon_{(\mathrm{img}),\alpha,\beta}(\omega) = \frac{e^2}{\epsilon_0 \Omega N_{\mathbf{k}}} \sum_n F^n_{\alpha,\beta} \frac{\eta}{(\hbar\omega - E^{(n)}_{cv})^2 + \eta^2} \ , \tag{2.96}$$

with the oscillator force given by:

$$F^{(n)}_{\alpha,\beta} = \left[\sum_{c,v,\mathbf{k}} \frac{A^{(n)}_{\mathbf{k}cv} \langle c, \mathbf{k} | P_\alpha | v, \mathbf{k} \rangle}{(E_{c,\mathbf{k}} - E_{v,\mathbf{k}} + i\eta)} \right] \left[\sum_{c',v',\mathbf{k}'} \frac{A^{(n^*)}_{\mathbf{k}'c'v'} \langle v', \mathbf{k}' | P_\beta | c', \mathbf{k}' \rangle}{(E_{c',\mathbf{k}'} - E_{v',\mathbf{k}'} + i\eta)} \right] \ . \tag{2.97}$$

From expressions for the dielectric tensor shown above, the absorption coefficient is calculated as:

$$A_{\alpha,\beta}(\omega) = \frac{\sqrt{2}\omega}{c} \left[\sqrt{\epsilon^2_{(re),\alpha,\beta}(\omega) + \epsilon^2_{(img),\alpha,\beta}(\omega)} - \epsilon_{(re),\alpha,\beta}(\omega) \right]^{1/2} \ . \tag{2.98}$$

2.7 Computational Implementations and Parameters

In the work, density functional theory calculations where performed using the Vienna *ab initio* Simulation Package[114,115]. We employ the exchange-correlation funcional proposed by Perdew-Burke-Ernzerhof[100] (PBE) for total energy calculations and structural optimizations while the electronic properties where calculated within the PBE including Spin-Orbit coupling (SOC). The single-particle bandgap where corrected using the HSE06[116,117] XC functional. Further details on DFT calculations where presented in appendix C.1. The optical and excitonic properties were studied using the WanTiBEXOS software[51] based on the single particle Tight-Binding Hamiltonian parametrized with Wannier90 software[118,119,120]. Appendix C.2 and C.3 presents other details on the Wannier90 calculation and optical and excitonic properties.

Chapter 3

Results

This chapter presents the results of applying the methodology described in Chapter 2 as the selection procedure for 2D Transition Metal Halides (TMHs). Section 3.1 details the selection procedure and summarizes the selected systems. Subsequently, structural optimization will be performed. Sections 3.3, 3.4, and 3.5 highlight the electronic and optical properties, and the excitonic properties of the systems, respectively. The tight-binding (TB) Hamiltonian is used to study these optical and excitonic properties, with the TB Hamiltonian obtained from DFT electronic structures parameterized using the maximum localized Wannier functions approach.

3.1 Systems Selection Procedure

This section outlines the procedure for selecting the systems studied by searching for promising 2D TMHs for optical applications in the Computational 2D Materials Database[89,90] (C2DB). The C2DB contains several 2D materials that are constructed using combinatorial lattice decoration based on existing structural prototypes known experimentally. Up to this date, there are more than 16.000 compounds with a description of structural, thermodynamic, elastic, electronic, and optical properties calculated using the GPAW program[121]. Additionally, some systems in C2DB include the study of excitonic properties by BSE solution and the G_0W_0 method for approximately 300 materials. The C2DB publications have been cited a total of 1.100 times (837 times[89] and 263 times[90])[1], demonstrating its potential as a starting point for the search for 2D systems.

[1]Data extract from Google Scholar on May 23, 2024.

The Web interface allows for navigation through the materials, accessible via URL `https://cmr.fysik.dtu.dk/c2db/c2db.html`. This access was facilitated using the Atomic Simulation Environment[122] (ASE) with a database file. The Python code used to query the compounds and an example of use is presented in appendix A. The search for promising 2D THMs for photovoltaic applications is guided by the following criteria.

1. Compounds with stoichiometries AB, AB_2, and AB_3 were selected, where A is a transition metal and B is the Halide, i.e., Cl, Br, or I. This selection was based on a literature review in which many materials with these stoichiometries were found.

2. Materials with band gaps using the HSE06 functional, including spin-orbit coupling between 0.65 and 2.12 eV, were chosen. The HSE06+SOC value was selected due to its ability to provide a more realistic description of the band gap[123]. This energy interval ensures maximum efficiency above 20 % in the Shockley-Queisser (SQ) limit[124], as shown in figure 3.1.

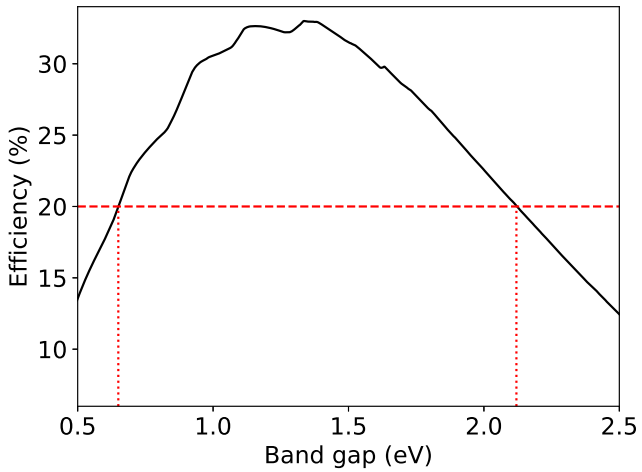

Figure 3.1: Shockley-Queisser limit for p-n junctions. The black solid line shows the SQ limit according to the band gap of the semiconductor. The red dotted lines depict band gaps that correspond to an efficiency of 20 %, according to the red dashed line. [source: own authorship]

3. Compounds with high stability to photons, characterized by phonon bands without imaginary frequencies, were selected. This indicates systems with structural stability[125].

4. Non-magnetic compounds were chosen. The scissors-operator methodology (presented in section 3.4.2) was shown not to work well for magnetic systems[41] due to different spin-channel corrections.

Table 3.1 presents the number of selected systems in each step cited above. Additional data on the selected structures is presented in appendix B and throughout the next sections.

Step	***AB***			***AB_2***			***AB_3***			**Total**
	Cl	Br	I	Cl	Br	I	Cl	Br	I	
1: composition	55	57	54	97	95	99	49	45	46	597
2: band gap	1	2	3	15	13	14	9	5	6	68
3: Phonon stability	0	0	1	14	12	10	8	3	5	53
4: Non-Magnetic	0	0	1	6	5	7	3	0	2	24

Table 3.1: The number of systems found in C2*D*B in each step is grouped according to stoichiometry and halide atom.

For the AB stoichiometry, only one system, Hg_2I_2, was found with space group $P\bar{3}m1$. The AB_2 stoichiometry presents the largest number of systems (18), featuring space groups $P2_1|m$, $P\bar{6}m2$, $P2_1|c$, and $P\bar{3}m1$. For the AB_3 stoichiometry, five systems were found with space groups $P\bar{3}1m$ and $P\bar{6}2m$. Figure 3.2 shows a stick-and-ball representation of these structures grouped according to their space groups and the transition metals they contain. The Bravais lattices presented can be categorized as tetragonal and hexagonal. The space group $P\bar{3}m1$ appears twice; to distinguish between the two structures with different stoichiometries, we denote the AB_2 structure as $P\bar{3}m1$-α and the AB structure as $P\bar{3}m1$-β. Additionally, the space groups $P2_1|c$, $P2_1|m$, and $P\bar{6}m2$ correspond to the AB_2 stoichiometry, while $P\bar{6}2m$ and $P\bar{3}1m$ are associated with the AB_3 stoichiometry. Transition metal halides (TMHs) based on group 2 metals (titanium, zirconium, and hafnium) appear in the space groups $P2_1|m$ (tetragonal) and $P\bar{6}m2$ (hexagonal). Metals from groups 4 and 7 appear in a hexagonal lattice, specifically $P\bar{6}2m$ and $P\bar{3}1m$. The palladium metal halide Pd_4I_8 features a v-shaped tetragonal structure in the space group $P2_1|c$.

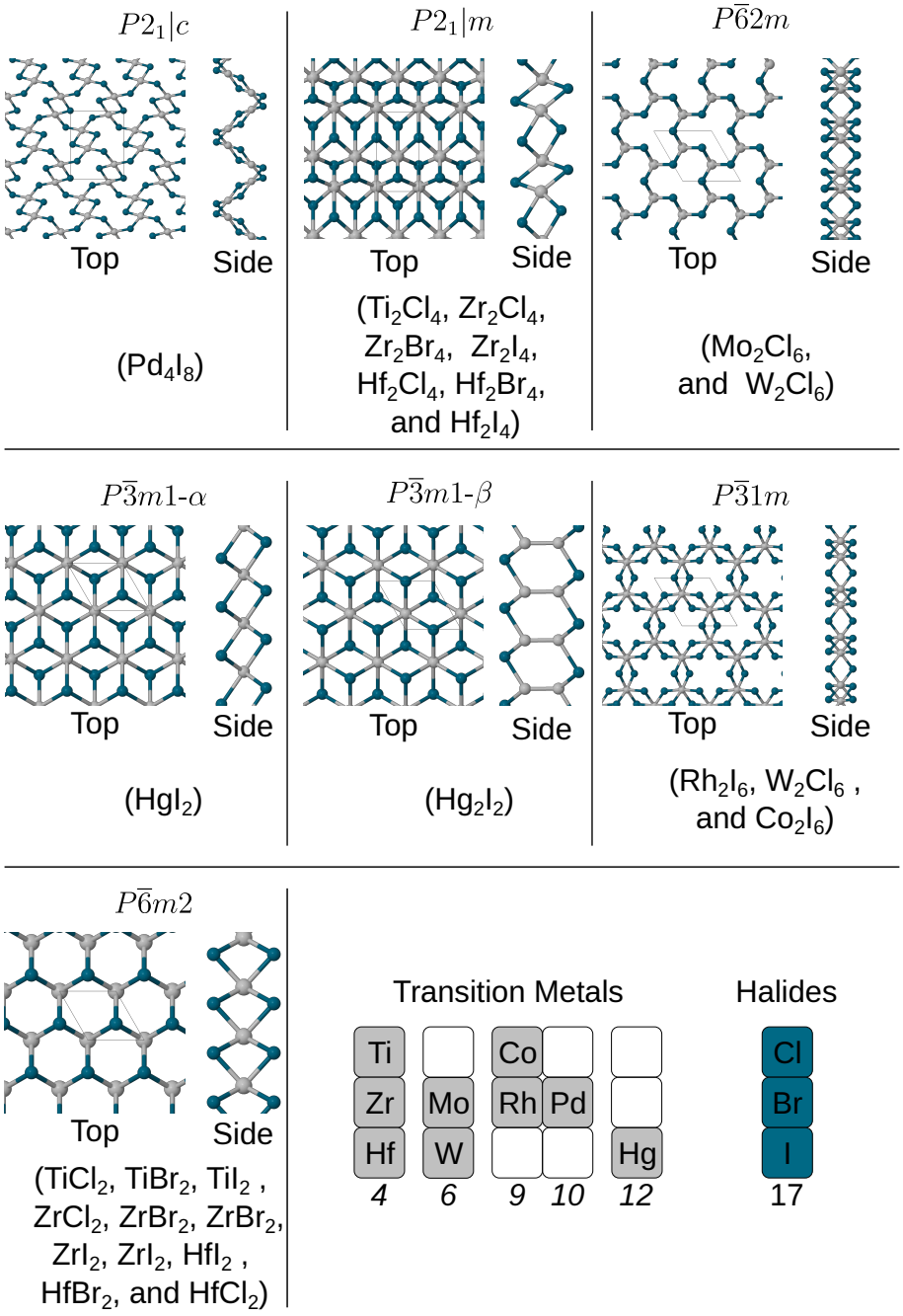

Figure 3.2: Summary of the structures of selected systems in C2*D*B is presented in this figure. Each panel displays the top and side view of a structure corresponding to each space group, with a $5 \times 5 \times 1$ supercell. The final panel shows the transition metals and halides found in our search organized by family group number.

Moreover, since the halide atoms, namely chlorine (Cl), bromine (Br), and iodine (I), share a common oxidation state of -1, we compare their oxidation states concerning

the metal atoms in the structures. Titanium-based TMHs exhibit a common oxidation state of 2 for the metal in AB_2 stoichiometry. Cobalt-based compounds display a common oxidation state of 3 in Co_2I_6. Mercury-based TMHs show a common oxidation state of 1 in Hg_2I_2 and 2 in HgI_2. Pd_4I_8 exhibits a usual oxidation state of 2. However, zirconium-based TMHs deviate from the norm with an unusual oxidation state of 2 for the metal atom. The same anomaly is observed in Mo_2Cl_6 with an oxidation state of 3, while hafnium and tungsten-based TMHs exhibit uncommon oxidation states of 2 and 3 for their respective metal atoms.

3.2 Structural Optimization

Our simulations begin by optimizing the lattice parameter and the internal coordinates of the atoms, where the initial structure was obtained from C2DB. The simulations constrain the lattice vector perpendicular to the monolayer, just like the C2DB structure, with optimized lattice parameters in the in-plane directions. Table 3.2 shows the main lattice parameters and those found in the literature and C2DB.

The optimized structures calculated here maintain the same space group and lattice angles as those of C2DB. Moreover, our lattice parameters agree with those of C2DB, with a maximum deviation of 0.8 %, as presented in table D.1 of the appendix. Several compositions of the TMH monolayers studied here have also been investigated in other works, as shown in table 3.2, which are all theoretical studies. Most of these works found that their lattice parameters deviate less than 0.02 Å from our own. The exceptions are Co_2I_6 ($P\bar{3}1m$) presented by Yekta *et al.*[127], which deviates by 0.09 Å, and Pd_4I_8 ($P2_1|c$) presented by Zhang *et al.*[75], with a deviation of 0.08 Å from our results.

Thus, a comparison with the C2DB and several other works in literature that used the same theoretical level allows to show the reliability of our structural parameters. Some differences, such as for Pd_4I_8 might be justified by different interlayer spacing, different cutoff energy for plane waves expansion or different points for Brillouin-Zone integrations, which is know for affect sensibly the simulation. Though, the same procedure and computation parameters used in this dissertation had also successfully been used to study other 2D systems[131,132,133,134].

Section C.1 of the appendix presents a discussion of complementary parameters used

Table 3.2: In-plane lattice parameters (a_0 and b_0) for optimized structures, including those from C2DB and the literature. The formula is displayed along with the total number of atoms in the structure. The space group is denoted as SG.

Formula (SG)	This work		C2DB		Literature		
	a_0 (Å)	b_0 (Å)	a_0 (Å)	b_0 (Å)	Ref.	a_0 (Å)	b_0 (Å)
Ti_2Cl_4 ($P2_1\|m$)	3.25	5.91	3.25	5.91	70	3.24	5.90
$TiCl_2$ ($P\bar{6}m2$)	3.28	3.28	3.28	3.28	126	3.29	3.29
$TiBr_2$ ($P\bar{6}m2$)	3.47	3.47	3.47	3.47	-	-	-
TiI_2 ($P\bar{6}m2$)	3.76	3.77	3.77	3.76	-	-	-
Co_2I_6 ($P\bar{3}1m$)	6.72	6.74	6.74	6.72	127	6.81	6.81
Zr_2Cl_4 ($P2_1\|m$)	3.33	6.23	3.33	6.24	72,128	3.34	6.23
$ZrCl_2$ ($P\bar{6}m2$)	3.41	3.41	3.41	3.41	-	-	-
Zr_2Br_4 ($P2_1\|m$)	3.49	6.50	3.49	6.50	72	3.49	6.48
$ZrBr_2$ ($P\bar{6}m2$)	3.56	3.56	3.56	3.56	-	-	-
Zr_2I_4 ($P2_1\|m$)	3.76	6.91	3.77	6.91	72	3.76	6.91
ZrI_2 ($P\bar{6}m2$)	3.82	3.83	3.83	3.82	-	-	-
Mo_2Cl_6 ($P\bar{6}2m$)	5.59	5.59	5.59	5.59	-	-	-
Rh_2I_6 ($P\bar{3}1m$)	6.90	6.93	6.93	6.90	129	6.92	6.92
Pd_4I_8 ($P2_1\|c$)	7.13	9.10	7.17	9.03	75	7.14	9.02
Hf_2Cl_4 ($P2_1\|m$)	3.27	6.16	3.28	6.16	130	3.26	6.13
					67	3.27	6.14
$HfCl_2$ ($P\bar{6}m2$)	3.35	3.35	3.35	3.35	-	-	-
Hf_2Br_4 ($P2_1\|m$)	3.43	6.43	3.44	6.42	67	3.43	6.42
					68	3.43	6.41
$HfBr_2$ ($P\bar{6}m2$)	3.49	3.50	3.50	3.49	-	-	-
Hf_2I_4 ($P2_1\|m$)	3.70	6.83	3.72	6.81	67	3.71	6.81
HfI_2 ($P\bar{6}m2$)	3.76	3.77	3.77	3.76	-	-	-
W_2Cl_6 ($P\bar{3}1m$)	5.56	5.56	5.56	5.56	-	-	-
W_2Cl_6 ($P\bar{6}2m$)	5.52	5.52	5.52	5.52	-	-	-
HgI_2 ($P\bar{3}m1$-α)	4.37	4.39	4.39	4.37	-	-	-
Hg_2I_2 ($P\bar{3}m1$-β)	4.46	4.48	4.46	4.47	-	-	-

for structural optimizations. From these optimized structures, all other simulations will be conducted keeping the structures frozen in their equilibrium geometry.

3.3 Density of States

To further analyze the electronic properties of the systems, we calculate the density of states (DOS) using the PBE functional and including spin-orbit coupling

(PBE+SOC). Figures E.1, E.2, E.3, and E.4 of the appendix show the total density of states (TDOS), the local density of states (LDOS) according to element (A and B, where A is the transition metal and B is the halide), and LDOS projected on atomic orbitals (A(s, p, d) and B(s, p, d, f)). The local density of states (LDOS) considers the DOS contribution on spherical shells centered on each element. The orbital composition is calculated by projecting Kohn-Sham eigenstates onto those spherical shells into atomic orbitals; thus it is important to emphasize that these analyses are only qualitative because they do not describe contributions in the interstitial regions between atoms.

Firstly, it should be noted that the density of states calculated with PBE and PBE+SOC deviates little in the atomic states near the Fermi level, which lies within an energy interval of 4 eV above and below the Fermi level[2]. Some changes in the density of states were observed for TiI_2 ($P\bar{6}m2$), where spin-orbit coupling causes splits in states below -2.5 eV. The Co_2I_6 and Rh_2I_6 (both with space group $P\bar{3}1m$) exhibit a reduction in the number of states, whereas changes occur in the conduction band minimum for Pd_4I_8 ($P2_1|c$) and W_2Cl_6 ($P\bar{6}2m$). In contrast, other systems display only slight changes. The effects of spin-orbit coupling on electronic structure will be highlighted in Section 3.4.1. Regarding the orbital compositions of DOS, the inclusion of spin-orbit coupling does not significantly alter the composition near the Fermi level; however, we note that the main changes in LDOS according to the composition arise from the p orbitals in halides and the d orbitals in transition metals, as exemplified by Rh_2I_6 in figure 3.3.

We observed that for almost all systems, the metal states predominantly feature d orbitals, whereas the halide states are characterized by p orbitals in the region near the Fermi level. A notable exception is mercury-based TMHs, where HgI_2 ($P\bar{3}m1$-α) exhibits halide states with p character in both valence and conduction bands near the Fermi level, whereas Hg_2I_2 ($P\bar{3}m1$-β) features halide p orbitals in the valence band and metal s orbitals in the conduction band. Other systems also display significant states s, p, or d of the halides and p of the transition metals.

In addition to our findings, previous studies have also reported the significant presence of metal d and halide p states near the Fermi level. For instance, Tang *et al.*[71] observed this behavior for $TiCl_2$ using the HSE06 functional. Similarly, Huang *et al.*[70] noted the major presence of metallic d states in their study on

[2]This range of energy was chosen because we are interested here in potential optoelectronic applications, and this range covers transitions from the infrared to ultraviolet.

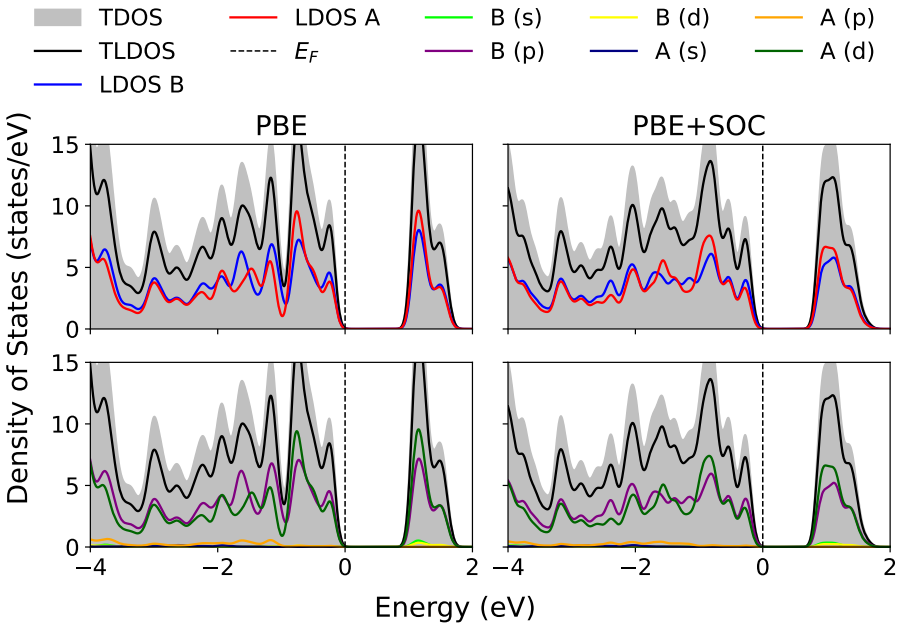

Figure 3.3: Total density of states (DOS), total local density of states (TLDOS), local densities of states for metal (LDOS A) and halide (LDOS B) atoms, as well as their orbital compositions (A(s, p, d) and B(s, p, d, f)), calculated for Rh2I6 ($P\bar{3}1m$) using both PBE and PBE+SOC.

Ti_2Cl_4. In zirconium-based TMHs, Huang *et al.*[72] reported that both metallic d orbitals and p orbitals are present from Cl, Br and I. According to Zhang *et al.*[75], the valence states in Pd_4I_8 are dominated by the d states of palladium and the p states of iodine. Furthermore, for Hafnium-based TMHs in the space group $P2_1|m$, both the p and d orbitals of the halide and Hf, respectively, also feature prominently near the Fermi level, as reported by Huang *et al.*[67]. These comparisons with other results ensure the reliability of our electronic structure calculations. The discussion of the states in DOS will also be taken into account when performing the wannierization as discussed in sections 2.6 and C.2.

3.4 Electronic Band Structures

This section presents the electronic band structures calculated using three distinct approaches: first, with the PBE functional; second, incorporating spin-orbit coupling (PBE+SOC); and third, employing the HSE06 functional. To correct the bandgap, it is necessary to calculate the electronic band structure using these three functionals, as discussed in section 3.4.2. Although PBE+SOC calculations are more accurate

in predicting electronic levels compared to PBE, the HSE06 approach provides a more accurate value of the band gap. The TMHs studied here exhibit hexagonal or tetragonal symmetry, with two possible Brillouin zones (BZ), depicted in figure 3.4. Figure 3.5 illustrates the band gap values obtained using these approaches as the differences from PBE+SOC and HSE06 to PBE. Section E.2 of Appendix E presents complementary details of electronic band structures.

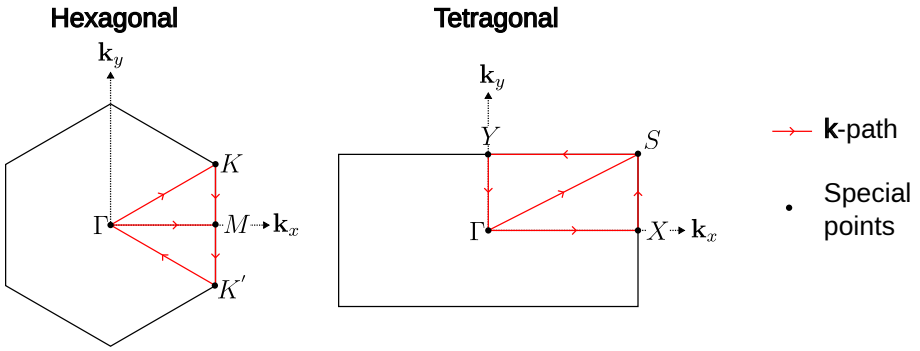

Figure 3.4: Brillouin zones for both hexagonal and tetragonal structures. The dashed arrow illustrates the primitive vectors in **k**-space. Special points are denoted by black dots, and the red line represents the path used to generate the band structures.

The PBE band structure features fundamental band gaps, which represent the energy difference between the valence maximum band (VBM) and the conduction band minimum (CBM), values range from 0.32 to 1.41 eV, while the direct band gaps, defined as the minimum energy difference at a specific **k**-point, range from 0.38 to 1.80 eV. Six systems exhibit direct fundamental bandgaps, where the VBM and CBM are located at the same **k**-point. These systems include TiI_2 ($P\bar{6}m2$) in the Γ point, Co_2I_6 ($P\bar{3}1m$) between the Γ and K points, Zr_2Cl_4 ($P2_1|m$) between the Γ and X points, Mo_2Cl_6 ($P\bar{6}2m$) in the Γ point, and W_2Cl_6 in both $P\bar{3}1m$ and $P\bar{6}2m$ space groups, also located at the Γ point. In total, 18 systems exhibited indirect fundamental band gaps. Notably, all structures with the $P\bar{6}m2$ space group (excluding TiI2) have their VBM located at the K point and their CBM situated between the Γ and K points. Similarly, structures with the $P2_1|m$ space group (except Zr_2Cl_4) also exhibit indirect fundamental band gaps, which have its VBM between the Γ and X points and its CBM between the Γ and S points. In addition, Rh_2I_6, Pd_4I_8, mercury-based, and all bromide-based TMHs also present indirect fundamental band gaps.

Concerning the PBE+SOC band structures, the fundamental and direct band gaps

exhibit values ranging from 0.32 to 1.26 eV and 0.38 to 1.74 eV, respectively. The number of systems with indirect band gaps increases to 20 compared to the PBE calculation, as detailed in section 3.4.1. The PBE+SOC calculations also lead to a reduction in the band gap for several systems. For instance, notable changes were observed for Co_2I_6, Rh_2I_6, HfI_2, and tungsten- and mercury-based TMHs, all featuring hexagonal lattices. Although the order of the systems in figure 3.5 is based on the atomic number of the metal atom, and even though spin-orbit coupling affects heavier metals more significantly, we do not observe an increase in band gap changes, suggesting that the halide atoms and their structural arrangement also contribute to these values.

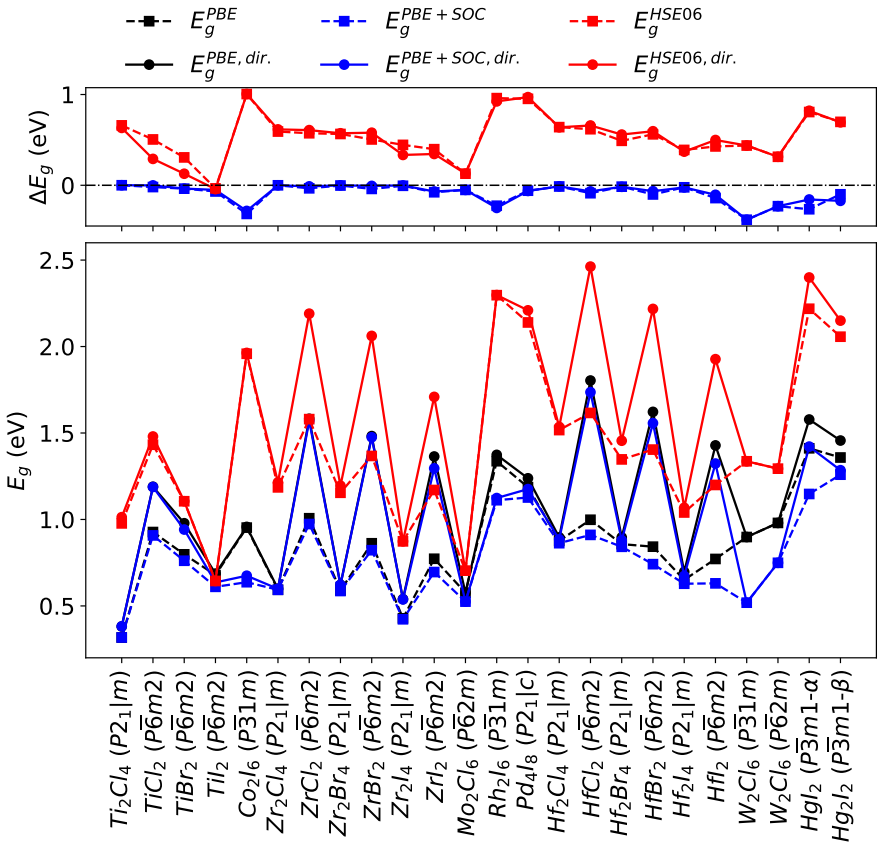

Figure 3.5: Fundamental (dashed lines with squares) and direct (solid lines with circles) band gaps using three functionals: PBE (black), PBE+SOC (blue), and HSE06 (red). The upper panel illustrates the changes in band gaps calculated using PBE+SOC and HSE06, compared to those obtained with PBE. The lower panel displays the corresponding band gap values.

The band structures calculated with the HSE06 functional exhibit an increase of up

to 1 eV in the band gaps, where the direct and fundamental band gaps increase for almost all systems, except TiI_2 ($P\bar{6}m2$), where the direct band gap is lower than the fundamental PBE band gap, and $HfBr_2$ ($P\bar{6}m2$), where the direct band gap is lower than the fundamental PBE and PBE+SOC band gaps. Notably, significant absolute changes were observed for Co_2I_6, Rh_2I_6, and Pd_4I_8 (depicts in figure 3.6), featuring localized (flat) states in the PBE, because the Hartree-Fock exchange term, the HSE06 functional is known to have more effect [135]. In total, eight systems exhibit a direct fundamental band gap in the HSE06 calculations. Beyond those observed in the PBE calculations, $TiBr_2$ ($P\bar{6}m2$) and Rh_2I_6 ($P\bar{3}1m$) also features a direct fundamental band gap.

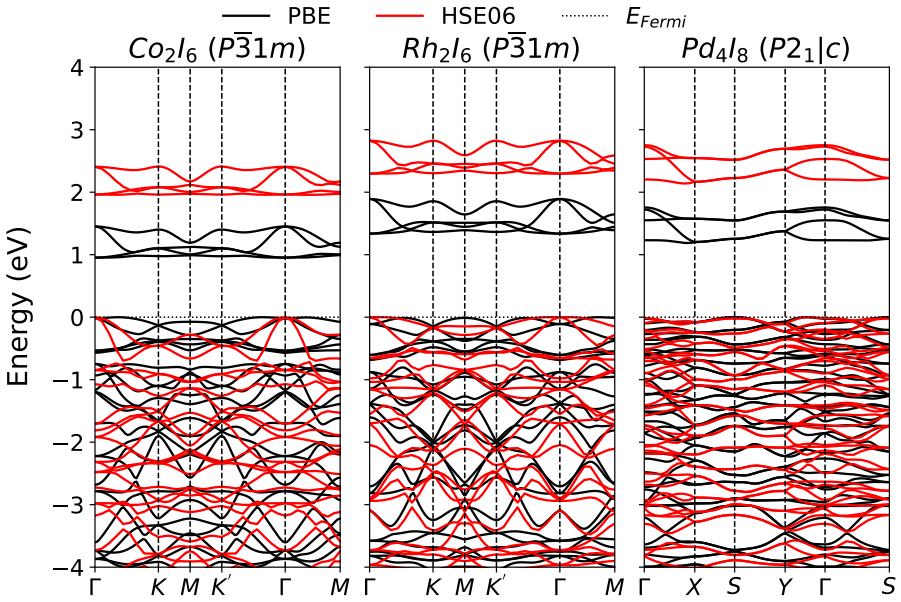

Figure 3.6: Band structures for Co_2I_6, Rh_2I_6, and Pd_4I_8 calculated using both the PBE (black lines) and HSE06 (red lines) functionals. In both cases, the Fermi level was shifted to zero.

Figure 3.7 presents the perceptual difference between C2DB and our results for the fundamental and direct band gaps using the PBE and PBE+SOC approaches. Initially, it should be noted that the difference is more pronounced in the PBE+SOC calculations compared to the PBE for most systems, with a maximum deviation of up to 9.20 % observed when using PBE and 17.4 % when using PBE+SOC. The fundamental and direct band gap differences are also substantial across the systems; for instance, for titanium, zirconium, and hafnium-based TMHs, the deviations re-

main below 3.2 % in both the PBE and PBE+SOC calculations compared to those observed in other systems. In contrast, for Co_2I_6 and Rh_2I_6, the deviation exceeds 10 %. Ultimately, the deviations exhibit different behavior between the fundamental and direct band gaps, with larger deviations observed for the fundamental band gap when using PBE and vice versa when using PBE+SOC.

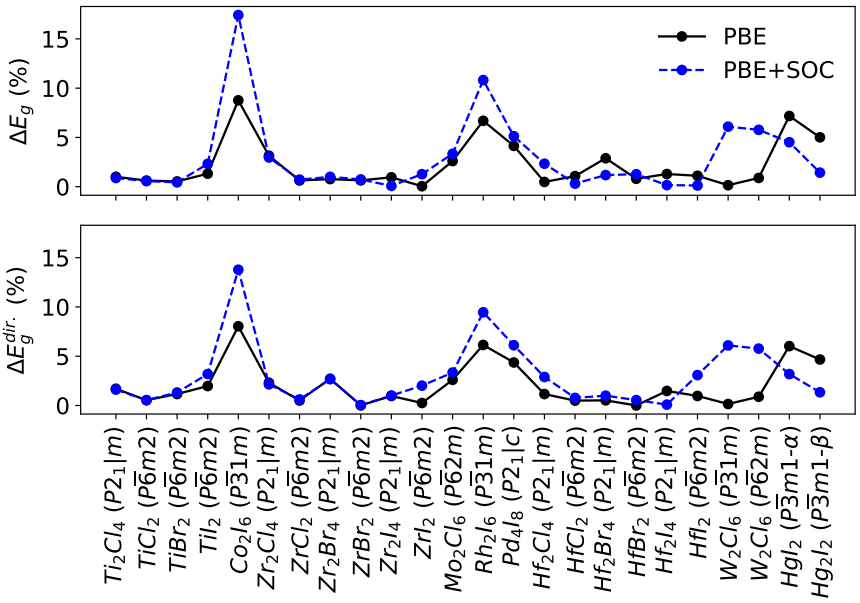

Figure 3.7: Perceptual difference, calculated with equation 3.1, between the band gaps calculated in this work and those presented in C2DB for PBE (black lines) and PBE+SOC (blue lines). The top panel shows the difference in the fundamental band gap (ΔE_g), while the bottom panel presents the difference in the direct band gap ($\Delta E_g^{dir.}$).

$$\Delta_X = \left(\frac{|X_{\text{C2DB}} - X_{\text{This work}}|}{X_{\text{This Work}}} \right) 100\% \ . \tag{3.1}$$

The literature contains several works that have studied electronic properties, allowing for some comparisons to be made. For instance, Huang *et al.*[70] found a fundamental band gap of 0.989 eV using the HSE06 functional, close to our value of 0.98 eV for Ti_2Cl_4. Huang *et al.*[72] reported band gaps of 1.152, 1.139, and 0.848 eV for Zr_2Cl_4, Zr_2Br_4, and Zr_2I_4, respectively, while our results are 1.19, 1.15, and 0.87 eV using the HSE06 functional. Wang *et al.*[128] obtained a direct fundamental band gap of 0.62 eV with the PBE functional for Zr_2Cl_4 in the Γ–X path, which

aligns with our findings. However, there is a discrepancy in the HSE06 values: we obtained an indirect fundamental band gap of 1.19 eV, whereas they reported a direct fundamental gap of 1.27 eV. For Rh_2I_6, Wu *et al.*[129] reported a band gap of 1.33 eV with the PBE functional, which is consistent with our result of 1.34 eV. For Pd_4I_8, Zhang *et al.*[75] obtained band gaps of 2.15 (HSE06) and 1.18 eV (PBE), comparable to our values of 2.14 (HSE06) and 1.19 eV (PBE). Li *et al.*[130] reported band gaps for Hf_2Cl_4 of 0.87 (PBE) and 1.48 eV (HSE06), which aligns with our findings of 0.88 (PBE) and 1.52 eV (HSE06). For Hf_2Cl_4, Hf_2Br_4, and Hf_2I_4, Huang *et al.*[67] found band gaps of 1.475, 1.337, and 1.033 eV, while our results are 1.52, 1.35, and 1.04 eV, respectively, all using the HSE06 functional. Lastly, Fan *et al.*[68] reported a band gap value of 1.31 eV for Hf_2Br_4 using the HSE06 functional.

3.4.1 Effect of Spin Orbit Coupling in the Electronic Structure

As stated in the methodology, the spin-orbit coupling breaks the degeneracy in the **k**-points, which can cause splits in the band structure, potentially changing the bandgap and electronic levels, as noted in graphene[136] where spin-orbit coupling opens a tiny band gap. In addition to that, spin-orbit coupling in TMDs[137,138], breaks the degeneracy in the wave functions, giving rise to valley selection when considering circularly polarized light. Thus, to obtain a more detailed description of electronic bands, we proceed to investigate the effect of spin-orbit coupling in comparison with that of PBE without spin-orbit coupling. In our systems, the changes were categorized into three distinct behaviors, observing the energy from -4 to 4 eV below and above the Fermi level:

1. **Systems with slight changes:** We observed only small changes between PBE and PBE+SOC in systems such as Ti_2Cl_4 ($P2_1|m$), $TiCl_2$ ($P\bar{6}m2$), Zr_2Cl_4 ($P2_1|m$), $ZrCl_2$ ($P\bar{6}m2$), and Mo_2Cl_6 ($P\bar{6}2m$).

2. **Systems with band splits but without changes in bandgap:** These systems exhibit changing electronic states, yet their bandgaps remain unaltered. Examples of such systems include $TiBr_2$ ($P\bar{6}m2$), TiI_2 ($P\bar{6}m2$), Zr_2Br_4 ($P2_1|m$), $ZrBr_2$ ($P\bar{6}m2$), Zr_2I_4 ($P2_1|m$), ZrI_2 ($P\bar{6}m2$), Hf_2Cl_4 ($P2_1|m$), $HfCl_2$ ($P\bar{6}m2$), Hf_2Br_4 ($P2_1|m$), $HfBr_2$ ($P\bar{6}m2$), and Hf_2I_4 ($P2_1|m$) and HfI_2 ($P\bar{6}m2$).

3. **Changes in the band gap and bands split:** The splitting of bands causes changes in the bandgap. Specifically, this is observed in systems such as Co_2I_6 ($P\bar{3}1m$), Rh$_2$I6 ($P\bar{3}1m$), Pd_4I_8 ($P2_1|c$), W_2Cl_6 ($P\bar{3}1m$), W_2Cl_6 ($P\bar{6}\bar{2}m$), HgI_2

($P\bar{3}m1$-α), and Hg_2I_2 ($P\bar{3}m1$-β).

Figure 3.8 depicts the systems with significant changes in the valence band maximum (VBM) and conduction band minimum (CBM). For Co_2I_6, the VBM changes from the Γ-K points to the gamma point and we note an important change in the states in the region between the K-M points, while the conduction states suffer a reduction with splits in states at the Γ point and the VBM is now located in the K point, where the band gap of this material remains indirect, however, changes the points of VBM and CBM. The same is observed for Rh_2I_6. For Pd_4I_8, W_2Cl_6 (in both space groups), HgI_2 and Hg_2I_2, we observed bands splits at some points and reduction of bandgap; however, the points of VBM and CBM remain the same. The complete band structure for the other systems, as well as additional details of the band split, are shown in figure E.5 of appendix E.

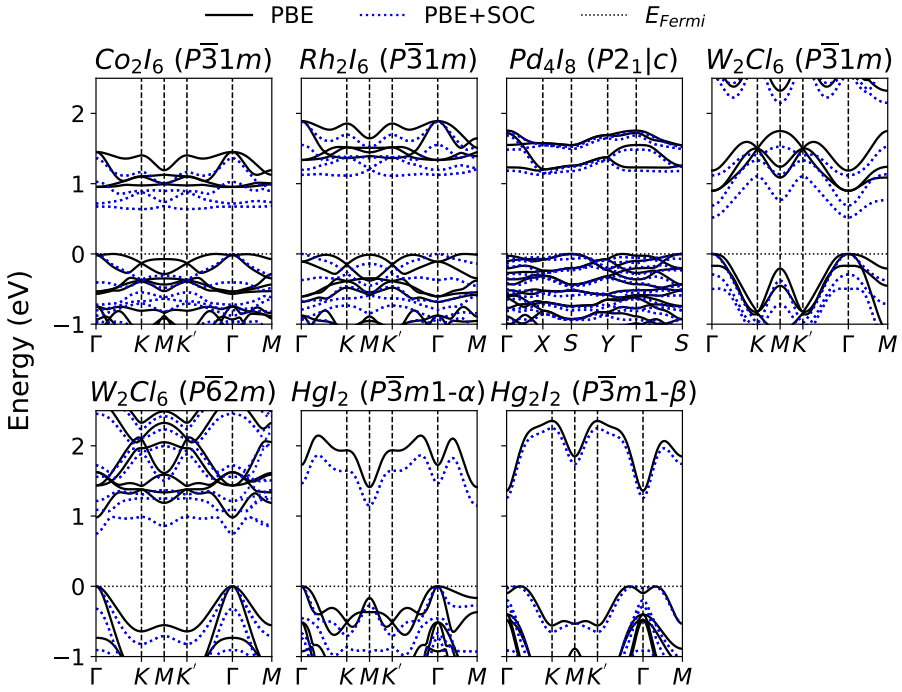

Figure 3.8: PBE (black solid line) and PBE+SOC (blue dotted line) band structures for selected compounds. The Fermi level is shifted to zero (black dotted line).

Figure 3.8 depicts systems exhibiting significant changes in the valence band maximum (VBM) and conduction band minimum (CBM). For Co_2I_6, the VBM shifts from the Γ-K points to the Γ point, accompanied by notable changes in states be-

tween the K-M points. Meanwhile, conduction states experience a reduction with splits occurring at the Γ point, and the VBM relocates to the K point, leaving the indirect band gap unchanged but altering its points of VBM and CBM. The same phenomenon is observed for Rh_2I_6. For Pd_4I_8, W_2Cl_6 (in both space groups), HgI_2 and Hg_2I_2, band splits occur at some points, accompanied by a reduction in the bandgap; however, the VBM and the CBM remain unchanged.

3.4.2 Bandgap Corrections

This section outlines the procedure for calculating the corrected band gap of materials. The significance of this calculation arises when studying electrical and optical properties to accurately describe electronic transitions. In this approach, a scissors operator approximation is employed, where conduction bands are rigidly translated to correct the single-particle band gap. Equation 3.2 provides the corrected bandgap, which involves the scissors operator (χ) performing a rigid translation in all conduction states. This methodology has previously been applied to describe various semiconductor systems, including perovskites[139] and 2D systems[140,41].

$$E_g^{\text{HSE06+SOC}} = E_g^{PBE+SOC} + (\overbrace{E_g^{HSE06} - E_g^{PBE}}^{\chi}) \ , \tag{3.2}$$

where, $E_g^{\text{HSE06+SOC}}$ represents the corrected band gap, and $E_g^{\text{x,dir}}$, x = PBE+SOC, HSE06, PBE, represents the direct band gap using the functionals PBE+SOC, HSE06, and PBE, respectively. This equation defines also the scissors operator (χ) as the difference between the HSE06 and PBE band gaps, which is then added to the PBE+SOC band gap.

Figure 3.9 presents the PBE, PBE+SOC, and HSE06 band gaps, along with the corrected band gap, and compares them to C2DB (also presented in table E.4 of the appendix). We chose to calculate the corrected bandgap from direct band gaps because our interest lies in optical properties, which are dominated by direct transitions due to the low momentum carried by photons.

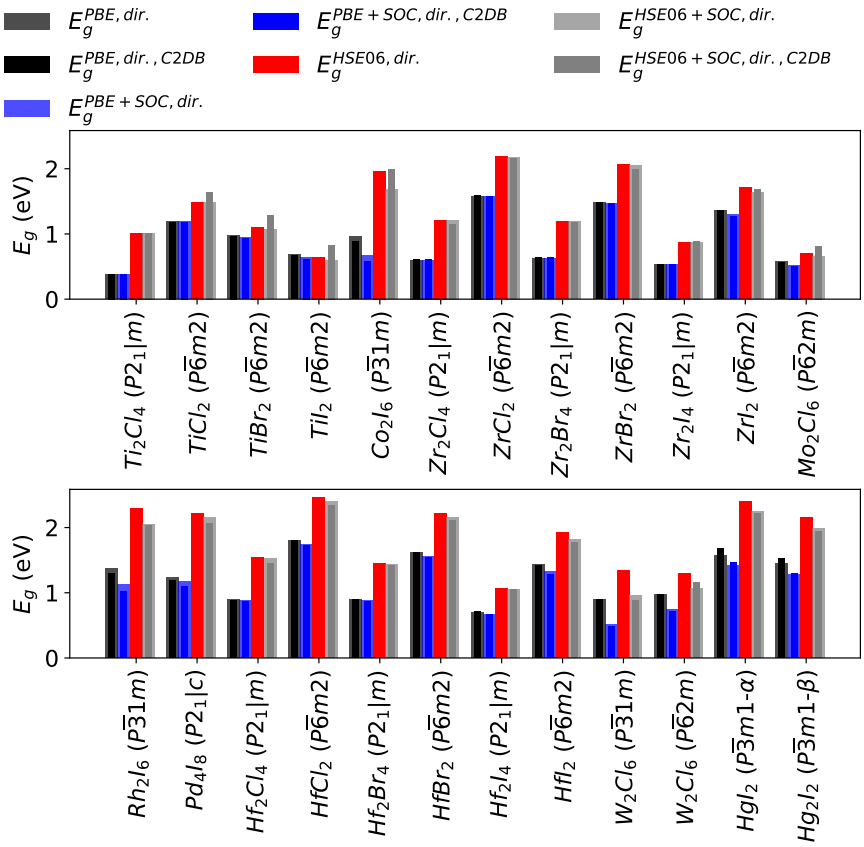

Figure 3.9: Comparations between PBE, PBE+SOC and HSE06 direct band gaps, the corrected HSE06+SOC bandgap using the scissors operator and the value presented in C2DB.

Four systems exhibit HSE06 + SOC band gaps that deviate less than 1 % from our calculated values, specifically Ti_2Cl_4, $ZrCl_2$, Hf_2I_4, and HgI_2. In seven systems, the HSE06+SOC bandgap obtained from C2DB exceeds ours, while in the remaining cases, it falls below ours. The systems with larger deviations are $TiCl_2$, $TiBr_2$, TiI_2, and Co_2I_6, where we found that the HSE06 correction is primarily responsible for these discrepancies due to the PBE and PBE + SOC values being very close, despite the C2DB not provide the HSE06 band gap value. This difference may arise from distinct parameters and implementations used in C2DB and our work.

3.5 Excitonic and Optical Properties

The excitonic and optical properties are investigated using the tight-binding Hamiltonian parametrized from the PBE+SOC band structure. The appendix (Sec-

tion C.2) provides details on the wannierization procedure, including the energy window for disentangling bands, the atomic orbitals considered for each system, the number of target Wannier bands, and the number of DFT bands used to construct hopping and overlap matrices. The atomic orbitals employed were based on the density of states with PBE+SOC functional, as depicted in figure E.4 (appendix). In most systems, the orbitals s, p, and d are considered for both metal and halide atoms. Exceptions include Co_2I_6 ($P\bar{3}1m$), Mo_2Cl_6 ($P\bar{6}2m$), and W_2Cl_6 ($P\bar{6}2m$), where only p and d orbitals are considered for the metal atom; in W_2Cl_6 ($P\bar{3}1m$), s, p, d, and f orbitals are employed. Figure F.1 (appendix) illustrates the interpolated Wannier bands and their comparison with the PBE+SOC band structures, which exhibit excellent agreement, confirming the quality of the tight binding Hamiltonian obtained.

The appendix C.3 and table G.1 present the parameters and methods used for optical and excitonic calculations. As Wannier parameterization was performed using the PBE+SOC functional, we applied the scissors operator (discussed in section 3.4.2) to correct the band gap. The number of valence bands considered was calculated to be all bands within the interval $\delta E = 4 - E_g$ below the conduction band minimum (CBM) and all bands within the energy interval δE above the valence band maximum (VBM). This ensures the correct choice of electronic transitions for calculating the dielectric tensor and optical properties in the independent particle approximation (IPA) and by solving the Bethe-Salpeter equation (BSE).

Figure 3.12 depicts the absorption coefficient, showing both the IPA and the BSE results. The figure also illustrates the fundamental and bright (accessible) excitonic states, as well as the single-particle direct bandgap.

Firstly, we note that for some systems the absorption coefficient obtained from the IPA perspective Presents isotropic light absorption between the x-y in-plane directions, whereas others are non-isotropic. For instance, all the tetragonal systems are non-isotropic and the hexagonal structures have space groups $P\bar{3}1m$ and $P\bar{6}2m$. The systems with isotropic light absorption are those with space groups $P\bar{6}m2$ and HgI_2 ($P\bar{3}m1$-α).

The maximum absorption values span a range of 3.66×10^6 to 8.84×10^6, averaging at $6.25 \times 10^6\,\mathrm{cm}^{-1}$, as shown in figure 3.11. In MoS_2[141], the observed value is $2.8 \times 10^6\,\mathrm{cm}^{-1}$. For silicon at 300 K, the maximum absorption coefficient is $1.5 \times 10^6\,\mathrm{cm}^{-1}$, according to Green and Keevers[142]. On average, the highest absorption coefficient

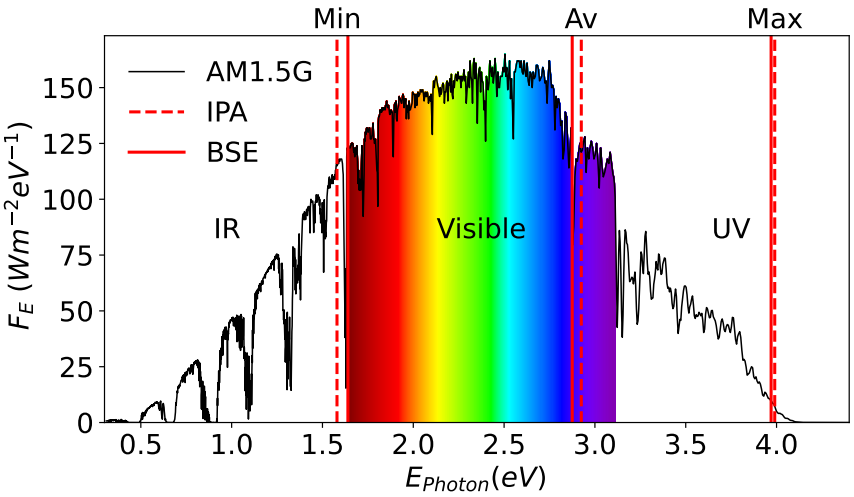

Figure 3.10: The standard global Solar spectrum AM1.5G[2] (black solid line) alongside the corresponding photon energy ranges for maximum light absorption for IPA (vertical red dashed line) and BSE (vertical red solid line). The figure also illustrates the colors associated with the visible spectrum.

occurs for a photon energy of approximately 2.93 eV, corresponding to the violet spectrum (Figure3.10) with a maximum absorption coefficient ranging from infrared to ultraviolet. Among the structures studied, 24 in total, eight exhibit the highest absorption coefficient in the visible spectrum, one in the infrared ($TiBr_2$), and 15 in the ultraviolet, considering the independent particle approximation.

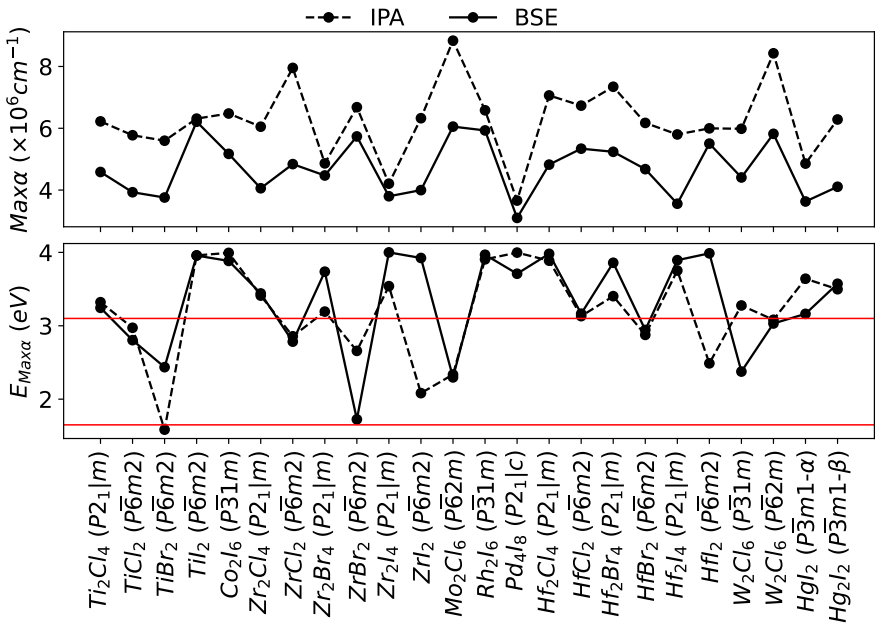

Figure 3.11: Max absorption coefficient value for each system and correspondent photon energy for IPA (dotted lines) and BSE (solid lines). The red lines in the bottom plot represent the photon energy of visible spectra.

We also observed that systems with the same chemical composition have different trends in the maximum absorption coefficients. For example, in zirconium-based TMHS, the maximum absorption coefficient is greater for hexagonal structures than for tetragonal structures. The opposite holds for hafnium-based TMHs with chloride and bromide, while for iodine both values are close. For tungsten and mercury halides, the maximum absorption values also change. We also observed some differences in the spectrum; for Zirconium-based TMHs, the maximum light absorption occurs in the ultraviolet for tetragonal structures, while for hexagonal structures, it occurs in the visible region. This behavior also applies to chloride, bromide, and iodine hafnium TMHs and for Ti_2Cl_4 (tetragonal) and $TiCl_2$ (hexagonal).

When excitons are considered, they drastically affect light absorption. First, all systems have an exciton bright state above the single-particle bandgap, then the optical activity starts for photon energy up to 0.83 eV before the IPA absorption spectrum. Some systems, have a clear exciton signature, i.e. we observed isolated peaks before the electronic single-particle band gap except in Co_2I_6, Rh_2I_6, Pd_4I_8, and HgI_2. The structures feature excitons binding energies from 0.23 eV to 1.68 eV. The fundamental state of excitons can be classified as bright or dark, where the

bright excitons have optical activity, whereas the dark ones do not. In almost all systems, the fundamental state is bright, except Ti_2Cl_4 ($P2_1|m$), where the exciton bright energy is 0.15 eV above the fundamental exciton state. Here, we also found a system, specifically TiI_2 ($P\bar{6}m2$), which has evidence of being an excitonic insulator, that is, a system in which the exciton binding energy exceeds the band gap[143]. In this case, the fundamental state is not the semiconductor, but the excited state.

In addition to that, we observed that the maximum light absorption from the BSE calculation is lower than the IPA for all systems. The inclusion of excitonic effects reduces the spectra regions with maximum absorption energy, generally the TMHs with chloride and iodine, which occurs for ten systems, whereas in others it increases or remains almost unchanged. It is of interest to note that for some systems the exciton effect changes the spectral region of maximum light absorption. For instance, in $TiBr_2$ where in IPA it is in the infrared while in BSE it is in the visible spectra, in $ZrBr_2$ where the maximum absorption suffuses a blue shift, in ZrI_2 and HfI_2 the maximum absorption goes from the visible region to the ultraviolet, while the opposite occurs with W_2Cl_6 ($P\bar{3}1m$), where this system, except for W_2Cl_6, the exciton has a large binding energy.

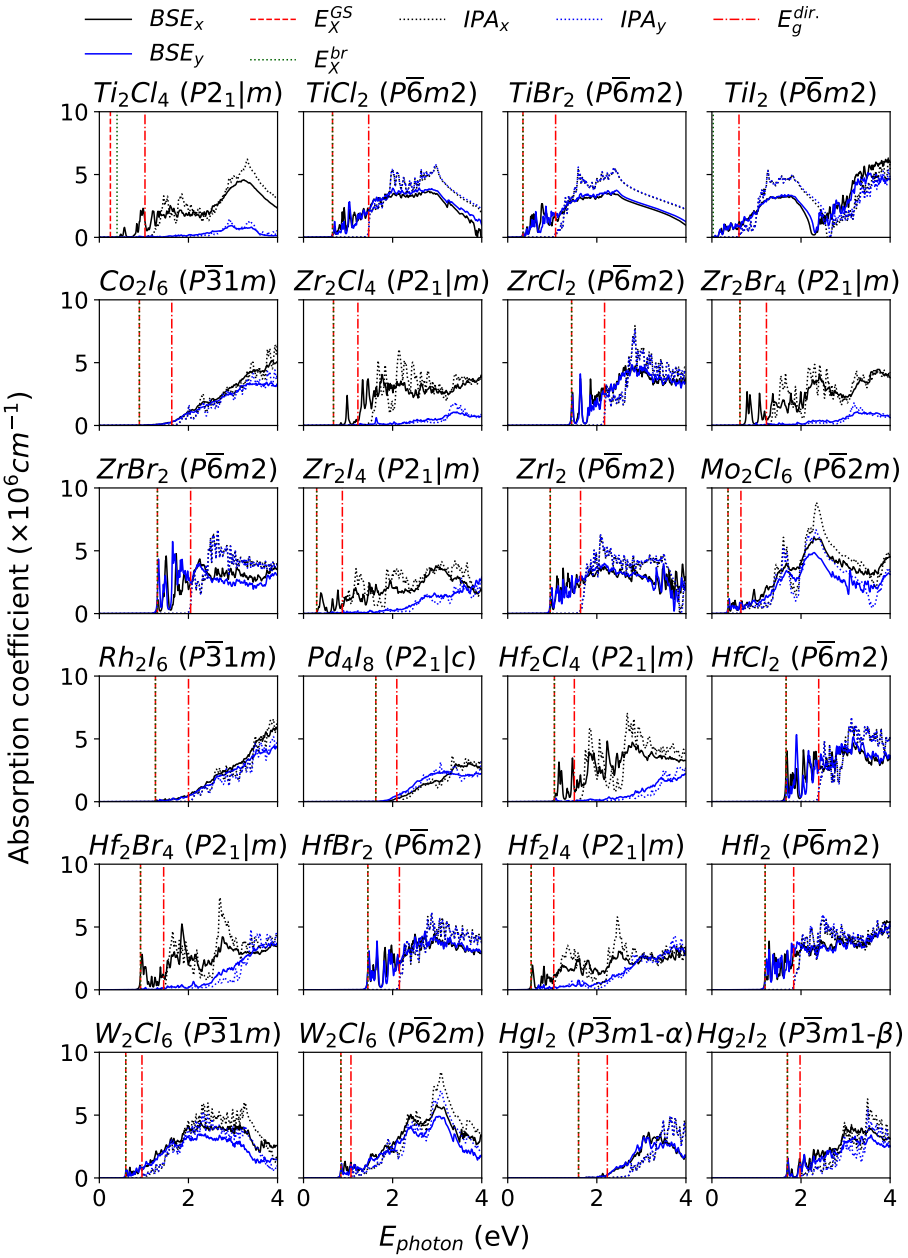

Figure 3.12: Absorption coefficient in IPA (dashed lines) and BSE (solid lines) frameworks along x (black lines) and y (blue lines), fundamental exciton state (vertical red dashed line), fundamental bright excitonic state (vertical green line) and direct bandgap (vertical red dot-dashed line). The bright excitons were considered as the first energy where the absorption coefficient is above $10 \times 10^3\,\mathrm{cm}^{-1}$.

To explore potential semiconducting applications, we calculate the possible heterojunctions, which comprise combinations of two or more distinct materials that enable

control over optical and electronic properties, including electronic transport. We begin by calculating the valence band maximum (VBM), conduction band minimum (CBM), and the fundamental bright exciton state with vacuum as a reference, calculated as the electrostatic potential value in the vacuum region of the systems (presented in section E.4 of appendix), as depicted in the upper panel of figure 3.14. We subsequently calculate the possible heterojunctions by applying Anderson's rule[144], which describes three types of heterojunctions based on their alignment relative to the vacuum:

- **Type I (Straddling Gap):** In this case the VBM of a semiconductor A is lower than the semiconductor B, while the opposite holds for CBM (and fundamental excitonic state).
- **Type II (Staggered Gap):** Both VBM and CBM (and fundamental excitonic state) of semiconductor A are higher than those from semiconductor B.
- **Type III (Broken Gap):** The CBM (and fundamental excitonic state) of one semiconductor is lower than the VBM of another semiconductor.

Figure 3.13 illustrates examples of possible heterojunctions. We focus on identifying type II heterojunctions, which possess properties enabling applications such as photovoltaic devices[145], photodetectors[146], light-emitting diodes[147], transistors[148], memory devices[149], and Photoelectrochemical Cells[150].

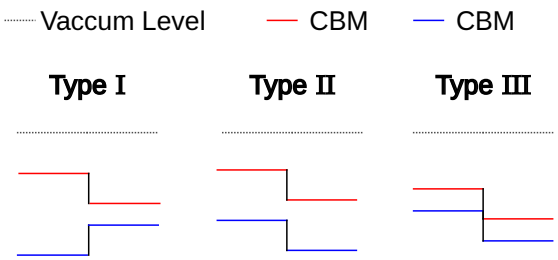

Figure 3.13: Possible types of heterojunctions.

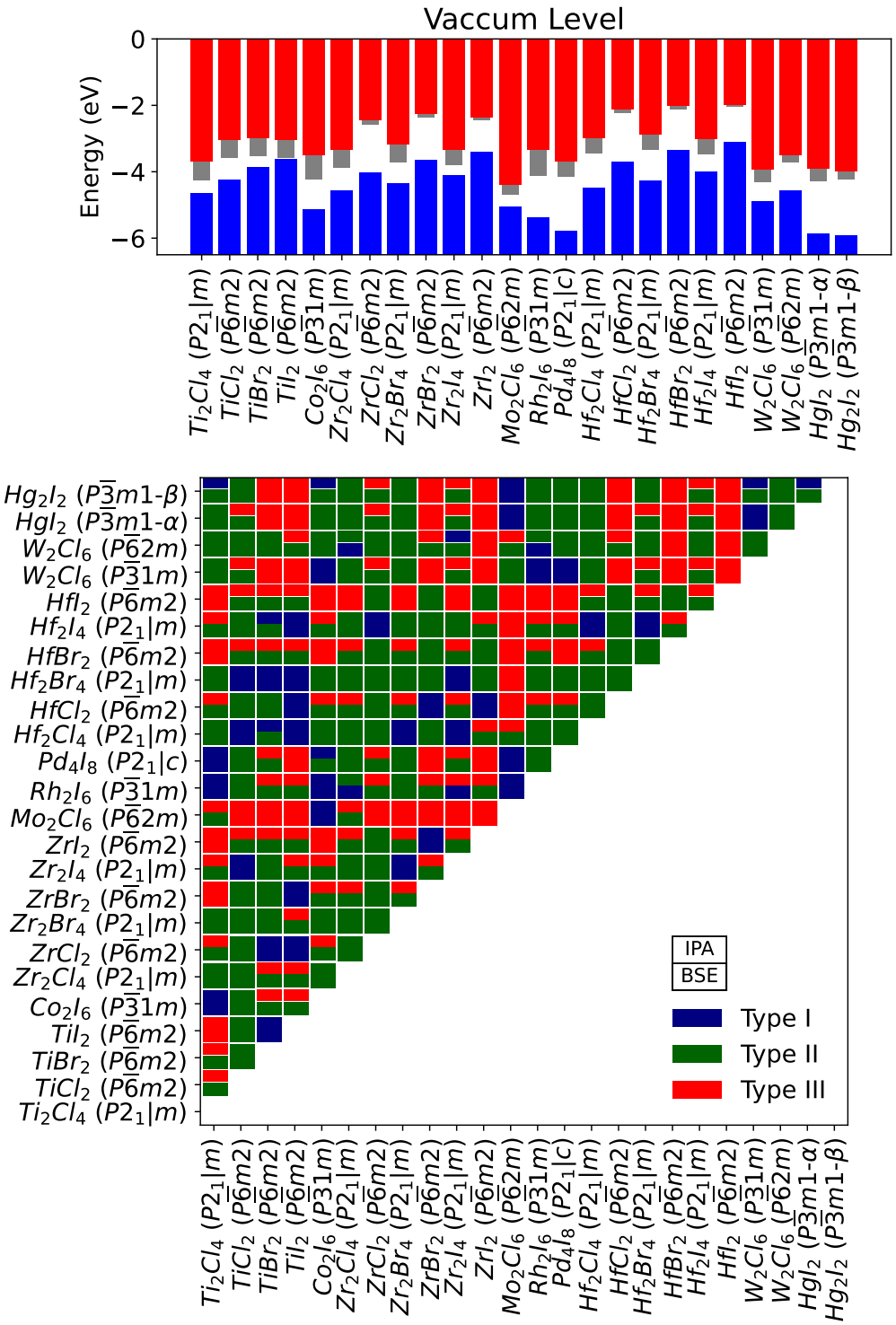

Figure 3.14: Bands alignment (top panel) and possible types of heterojunctions (bottom) panel. The possible types of heterojunctions are calculated from both, IPA and BSE perspectives.

In the lower panel of figure 3.14, we show possible heterojunctions, totaling 276 possible heterojunctions, which are classified according to the IPA and BSE approaches. From the IPA perspective, there are heterojunctions of type 183 type II, 54 type III, and 39 type I. When excitonic effects are taken into account, the type II heterojunctions decrease to 100, while types I and III increase to 133 and 43, respectively. Overall, 90 possible heterojunctions change their characteristics when considering excitonic effects. For instance, we observe 3 systems that transform from type I to II, none transition from III to II, whereas eight systems shift from type II to I and 78 from type II to III. Finally, our results indicate that 35, 97, and 54 are type I, II, and III heterojunctions, respectively, in both IPA and BSE. These findings demonstrate the importance of considering excitonic effects for the correct identification of heterojunctions.

Chapter 4

Discussion and Conclusions

This section presents the main findings of the present dissertation. Initially, we utilized a protocol for searching promising materials for photovoltaic applications within the C2DB database, which contains a vast number of two-dimensional materials with various properties studied through theoretical methods. In total, 24 materials were selected, showcasing diverse crystalline structures and compositions. Notably, TMHs based on titanium, cobalt, zirconium, molybdenum, rhodium, palladium, hafnium, tungsten, and mercury were identified, covering a wide range of transition metals. Our analysis revealed that some structures exhibit the metal atom in common oxidation states, whereas others display unusual oxidation states.

The structural optimizations conducted are in agreement with the structures presented in the C2DB and other theoretical works that employed similar methodology. Based on the optimized structures, we analyzed the electronic properties, which revealed that for most systems, the main contributions came from p orbitals of halide atoms and d orbitals of metal atoms, exceptip for mercury-based TMHs. The electronic band structures exhibit a wide range of band gaps and their behaviors, with most materials analyzed using the PBE exchange-correlation functional in DFT calculations possessing indirect band gaps, all featuring hexagonal structures. The inclusion of relativistic effects with spin-orbit coupling (SOC) modifies the electronic states compared to PBE calculations without SOC, where notable changes were observed for 7 systems containing Co, Rh, Pd, W, and Hg metal atoms at specific **k**-points in the VBM, CBM, and their values. Comparison with C2DB showed that the results band gaps (PBE and including relativistic effects) has large deviations for some systems, particularly when considering relativistic effects rather than without

them.

The bandgap corrections considering both relativistic effects and hybrid exchange-correlation functionals deviate substantially from those presented in C2DB, primarily due to the hybrid functional effect, which may arise from different parameters and procedures used for calculating these corrections. Consequently, we conclude that while C2DB can serve as a good starting point for identifying promising compositions for optoelectronic applications, careful evaluation of electronic properties is still necessary.

The optical properties reveal that, in the independent particle approximation, the systems exhibit varying isotropic behavior with respect to their in-plane absorption coefficient. For instance, all tetragonal structures display non-isotropic absorption coefficients in both the independent particle approximation and the BSE, as well as hexagonal structures featuring space groups $P\bar{3}1m$ and $P\bar{6}2m$. Systems with space groups $P\bar{6}m2$ and Hg_2I_2in the space group $P\bar{3}m1$-α, however, exhibit isotropic light absorption. The maximum absorption varies extensively across a broad range of the spectrum, from infrared to ultraviolet, where most systems absorb more light near the violet end of the spectrum.

The inclusion of excitonic effects significantly alters the absorption behavior. A decrease in maximum absorption is observed for all systems, accompanied by changes in the maximum absorption spectrum for most systems. We observe that all systems exhibit optically and fundamentally distinct excitonic states below their respective electronic band gaps, which alter the optical transitions. Only one system had a dark ground state, differing by 0.15 eV from the fundamental state. When assessing potential heterojunctions, we demonstrate that considering both the electronic band gap and the excitonic effect reveals that most systems fall under type II, a configuration desirable for various optoelectronic applications. However, the inclusion of the excitonic effect significantly modifies several possible characteristics of heterojunctions, resulting in a lower number of type II heterojunctions. Consequently, a comprehensive description of heterojunctions must incorporate excitonic effects. Moreover, we have identified a system that exhibits evidence of an excitonic insulator, wherein the exciton binding energy exceeds the electronic bandgap.

In conclusion, our work explored the transition metal halides (TMHs), a family of two-dimensional (2D) materials that have been extensively studied in recent years. We searched promising compositions and structures within the Computational 2D

Materials Database (C2DB), resulting in 24 materials with varying possible compositions, stoichiometries, and structures. Notably, some compositions exhibited a common oxidation number, suggesting their feasibility. The initial structures collected from C2DB agree with our optimized structures using state-of-the-art density functional theory (DFT). Regarding the electronic structure, the systems generally exhibit states of d-character for metal and p-character for halide near the Fermi level. In contrast to structural properties, the electronic properties presented in C2DB significantly deviate from those calculated here. Therefore, we conclude that despite C2DB being a good starting point for searching materials, careful simulations must be performed to obtain a better electronic characterization than that provided by C2DB. By parameterizing the electronic structure obtained from DFT simulations with the maximum localized Wannier functions procedure implemented in the Wannier90 software, we investigated the optical and excitonic properties, where the excitonic effects were studied by solving the Bethe-Salpeter equation (BSE). Our results show that light absorption is both isotropic and non-isotropic, with a wide range of values for the maximum absorption coefficient as a the spectral region. The exciton effects, such as binding energy, ranged from 0.23 to 1.68 eV, where almost all systems exhibited bright behavior, with only one system had a dark ground state. Furthermore, we found evidence of an excitonic insulator, specifically TiI_2 in the space group $P\bar{6}m2$. Ultimately, consideration of excitonic effects is crucial when studying these compounds for optical applications, as they alter the possible heterojunction types.

Referências

[1] Sajedeh Manzeli, Dmitry Ovchinnikov, Diego Pasquier, Oleg V. Yazyev, and Andras Kis. 2d transition metal dichalcogenides. *Nature Reviews Materials*, 2 (8):1, June 2017. ISSN 2058-8437. doi: 10.1038/natrevmats.2017.33.

[2] Standard Tables for Reference Solar Spectral Irradiances: Direct Normal and Hemispherical on 37° Tilted Surface. https://www.astm.org/g0173-03r20.html.

[3] R. Peierls. Quelques propriétés typiques des corps solides. *Annales de l'institut Henri Poincaré*, 5(3):177–222, 1935. ISSN 2400-4855.

[4] L. D. Landau. On the theory of phase transitions. *Zh. Eksp. Teor. Fiz.*, 7: 19–32, 1937. doi: 10.1016/B978-0-08-010586-4.50034-1.

[5] A. K. Geim. Graphene prehistory. *Phys. Scr.*, 2012(T146):014003, January 2012. ISSN 1402-4896. doi: 10.1088/0031-8949/2012/T146/014003.

[6] K. S. Novoselov, A. K. Geim, S. V. Morozov, D. Jiang, Y. Zhang, S. V. Dubonos, I. V. Grigorieva, and A. A. Firsov. Electric field effect in atomically thin carbon films. *Science*, 306(5696):666, October 2004. ISSN 1095-9203. doi: 10.1126/science.1102896.

[7] Enlai Gao, Shao-Zhen Lin, Zhao Qin, Markus J. Buehler, Xi-Qiao Feng, and Zhiping Xu. Mechanical exfoliation of two-dimensional materials. *Journal of the Mechanics and Physics of Solids*, 115:248–262, June 2018. ISSN 0022-5096. doi: 10.1016/j.jmps.2018.03.014.

[8] K. S. Novoselov, D. Jiang, F. Schedin, T. J. Booth, V. V. Khotkevich, S. V. Morozov, and A. K. Geim. Two-dimensional atomic crystals. *Proceedings of the National Academy of Sciences*, 102(30):10451–10453, July 2005. doi: 10.1073/pnas.0502848102.

[9] Changgu Lee, Xiaoding Wei, Jeffrey W. Kysar, and James Hone. Measurement of the Elastic Properties and Intrinsic Strength of Monolayer Graphene. *Science*, 321(5887):385–388, July 2008. doi: 10.1126/science.1157996.

[10] Alexander A. Balandin, Suchismita Ghosh, Wenzhong Bao, Irene Calizo, Desalegne Teweldebrhan, Feng Miao, and Chun Ning Lau. Superior Thermal Conductivity of Single-Layer Graphene. *Nano Lett.*, 8(3):902–907, March 2008. ISSN 1530-6984. doi: 10.1021/nl0731872.

[11] Tae-Hee Han, Hobeom Kim, Sung-Joo Kwon, and Tae-Woo Lee. Graphene-based flexible electronic devices. *Materials Science and Engineering: R: Reports*, 118:1–43, August 2017. ISSN 0927-796X. doi: 10.1016/j.mser.2017.05.001.

[12] Gianluca Fiori and Giuseppe Iannaccone. Ultralow-voltage bilayer graphene tunnel fet. *IEEE Electron Device Letters*, 30(10):1096, October 2009. ISSN 1558-0563. doi: 10.1109/LED.2009.2028248.

[13] Andrey A. Generalov, Michael A. Andersson, Xinxin Yang, Andrei Vorobiev, and Jan Stake. A 400-ghz graphene fet detector. *IEEE Transactions on Terahertz Science and Technology*, 7(5):614, September 2017. ISSN 2156-3446. doi: 10.1109/TTHZ.2017.2722360.

[14] Chun-Hua Lu, Huang-Hao Yang, Chun-Ling Zhu, Xi Chen, and Guo-Nan Chen. A graphene platform for sensing biomolecules. *Angewandte Chemie*, 121(26):4879, 2009. ISSN 1521-3757. doi: 10.1002/ange.200901479.

[15] Yong-Hui Zhang, Ya-Bin Chen, Kai-Ge Zhou, Cai-Hong Liu, Jing Zeng, Hao-Li Zhang, and Yong Peng. Improving gas sensing properties of graphene by introducing dopants and defects: a first-principles study. *Nanotechnology*, 20 (18):185504, April 2009. ISSN 0957-4484. doi: 10.1088/0957-4484/20/18/185504.

[16] Kailiang Zhang, Yulin Feng, Fang Wang, Zhengchun Yang, and John Wang. Two dimensional hexagonal boron nitride (2D-hBN): Synthesis, properties and applications. *J. Mater. Chem. C*, 5(46):11992–12022, November 2017. ISSN 2050-7534. doi: 10.1039/C7TC04300G.

[17] Alexander Kolobov and Junji Tominaga. *Two-Dimensional Transition-Metal Dichalcogenides*. Springer International Publishing Switzerland, 2016. ISBN 978-3-319-31450-1.

[18] Yury Gogotsi and Babak Anasori. The Rise of MXenes. *ACS Nano*, 13(8): 8491–8494, August 2019. ISSN 1936-0851. doi: 10.1021/acsnano.9b06394.

[19] Jason K. Ellis, Melissa J. Lucero, and Gustavo E. Scuseria. The indirect to direct band gap transition in multilayered MoS2 as predicted by screened hybrid density functional theory. *Applied Physics Letters*, 99(26):261908, December 2011. ISSN 0003-6951. doi: 10.1063/1.3672219.

[20] Andrea Splendiani, Liang Sun, Yuanbo Zhang, Tianshu Li, Jonghwan Kim, Chi-Yung Chim, Giulia Galli, and Feng Wang. Emerging Photoluminescence in Monolayer MoS2. *Nano Lett.*, 10(4):1271–1275, April 2010. ISSN 1530-6984. doi: 10.1021/nl903868w.

[21] Kin Fai Mak, Changgu Lee, James Hone, Jie Shan, and Tony F. Heinz. Atomically thin MoS_2: A new direct-gap semiconductor. *Phys. Rev. Lett.*, 105(13): 136805, September 2010. doi: 10.1103/PhysRevLett.105.136805.

[22] B. Radisavljevic, A. Radenovic, J. Brivio, V. Giacometti, and A. Kis. Single-layer mos 2 transistors. *Nature Nanotech*, 6(3):147, March 2011. ISSN 1748-3395. doi: 10.1038/nnano.2010.279.

[23] Simone Bertolazzi, Daria Krasnozhon, and Andras Kis. Nonvolatile memory cells based on mos2/graphene heterostructures. *ACS Nano*, 7(4):3246, April 2013. ISSN 1936-0851. doi: 10.1021/nn3059136.

[24] Jin Xiao, Mengqiu Long, Xinmei Li, Qingtian Zhang, Hui Xu, and K. S. Chan. Effects of van der waals interaction and electric field on the electronic structure of bilayer mos2. *J. Phys.: Condens. Matter*, 26(40):405302, September 2014. ISSN 0953-8984. doi: 10.1088/0953-8984/26/40/405302.

[25] Meng-Lin Tsai, Sheng-Han Su, Jan-Kai Chang, Dung-Sheng Tsai, Chang-Hsiao Chen, Chih-I Wu, Lain-Jong Li, Lih-Juann Chen, and Jr-Hau He. Monolayer mos2 heterojunction solar cells. *ACS Nano*, 8(8):8317, August 2014. ISSN 1936-0851. doi: 10.1021/nn502776h.

[26] Chang Woo Myung, Amir Hajibabaei, Ji-Hyun Cha, Miran Ha, Junu Kim, and Kwang S. Kim. Challenges, Opportunities, and Prospects in Metal Halide Perovskites from Theoretical and Machine Learning Perspectives. *Advanced Energy Materials*, 12(45):2202279, 2022. ISSN 1614-6840. doi: 10.1002/aenm.202202279.

[27] Ahmed Elbanna, Ksenia Chaykun, Yulia Lekina, Yuanda Liu, Benny Febriansyah, Shuzhou Li, Jisheng Pan, Ze Xiang Shen, and Jinghua Teng. Perovskite-transition metal dichalcogenides heterostructures: Recent advances and future perspectives. *OES*, 1(8):220006–40, Thu Aug 04 00:00:00 CST 2022. ISSN 2097-0382. doi: 10.29026/oes.2022.220006.

[28] Martin A. Green, Ewan D. Dunlop, Jochen Hohl-Ebinger, Masahiro Yoshita, Nikos Kopidakis, and Xiaojing Hao. Solar cell efficiency tables (version 56). *Progress in Photovoltaics: Research and Applications*, 28(7):629–638, 2020. ISSN 1099-159X. doi: 10.1002/pip.3303.

[29] Pingping Jiang, Debdipto Acharya, George Volonakis, Marios Zacharias, Mikaël Kepenekian, Laurent Pedesseau, Claudine Katan, and Jacky Even. Pb-free halide perovskites for solar cells, light-emitting diodes, and photocatalysts. *APL Materials*, 10(6):060902, June 2022. ISSN 2166-532X. doi: 10.1063/5.0095515.

[30] Lucas G. Chagas, Juarez L. F. Da Silva, and Matheus P. Lima. Role of Jahn-Teller distortion in the relative stability between the black and yellow phases of transition metal doped ${\mathrm{CsSnI}}_{3}$ perovskites. *Phys. Rev. B*, 109(1):014106, January 2024. doi: 10.1103/PhysRevB.109.014106.

[31] Jianfeng Zhang, Bin Wei, Lin Wang, and Xuyong Yang. The solution-processed fabrication of perovskite light-emitting diodes for low-cost and commercial applications. *J. Mater. Chem. C*, 9(36):12037–12045, September 2021. ISSN 2050-7534. doi: 10.1039/D1TC03385A.

[32] Riley E. Brandt, Rachel C. Kurchin, Robert L. Z. Hoye, Jeremy R. Poindexter, Mark W. B. Wilson, Soumitra Sulekar, Frances Lenahan, Patricia X. T. Yen, Vladan Stevanović, Juan C. Nino, Moungi G. Bawendi, and Tonio Buonassisi. Investigation of bismuth triiodide (bii3) for photovoltaic applications. *J. Phys. Chem. Lett.*, 6(21):4297–4302, November 2015. doi: 10.1021/acs.jpclett.5b02022.

[33] Chun-Sheng Liu, Xiao-Le Yang, Jin Liu, and Xiao-Juan Ye. Exfoliated Monolayer GeI2: Theoretical Prediction of a Wide-Band Gap Semiconductor with Tunable Half-Metallic Ferromagnetism. *J. Phys. Chem. C*, 122(38):22137–22142, September 2018. ISSN 1932-7447. doi: 10.1021/acs.jpcc.8b05529.

[34] Michael A. McGuire, Genevieve Clark, Santosh KC, W. Michael Chance, Gerald E. Jellison, Valentino R. Cooper, Xiaodong Xu, and Brian C. Sales. Magnetic behavior and spin-lattice coupling in cleavable van der waals layered $crcl_3$ crystals. *Phys. Rev. Materials*, 1(1):014001, June 2017. doi: 10.1103/PhysRevMaterials.1.014001.

[35] Mianzeng Zhong, Le Huang, Hui-Xiong Deng, Xiaoting Wang, Bo Li, Zhongming Wei, and Jingbo Li. Flexible photodetectors based on phase dependent pbi2 single crystals. *J. Mater. Chem. C*, 4(27):6492–6499, July 2016. ISSN 2050-7534. doi: 10.1039/C6TC00918B.

[36] Yaguang Wang, Lin Gan, Junnian Chen, Rui Yang, and Tianyou Zhai. Achieving highly uniform two-dimensional PbI2 flakes for photodetectors via space confined physical vapor deposition. *Science Bulletin*, 62(24):1654–1662, December 2017. ISSN 2095-9273. doi: 10.1016/j.scib.2017.11.011.

[37] Pere Miró, Martha Audiffred, and Thomas Heine. An atlas of two-dimensional materials. *Chem. Soc. Rev.*, 43(18):6537–6554, August 2014. ISSN 1460-4744. doi: 10.1039/C4CS00102H.

[38] Gregory H. Wannier. The Structure of Electronic Excitation Levels in Insulating Crystals. *Phys. Rev.*, 52(3):191–197, August 1937. doi: 10.1103/PhysRev.52.191.

[39] J. Frenkel. On the Transformation of light into Heat in Solids. I. *Phys. Rev.*, 37(1):17–44, January 1931. doi: 10.1103/PhysRev.37.17.

[40] Alexey Chernikov, Timothy C. Berkelbach, Heather M. Hill, Albert Rigosi, Yilei Li, Burak Aslan, David R. Reichman, Mark S. Hybertsen, and Tony F. Heinz. Exciton Binding Energy and Nonhydrogenic Rydberg Series in Monolayer ${\mathrm{WS}}_{2}$. *Phys. Rev. Lett.*, 113(7):076802, August 2014. doi: 10.1103/PhysRevLett.113.076802.

[41] A. C. Dias, Helena Bragança, João Paulo A. de Mendonça, and Juarez L. F. Da Silva. Excitonic Effects on Two-Dimensional Transition-Metal Dichalcogenide Monolayers: Impact on Solar Cell Efficiency. *ACS Appl. Energy Mater.*, 4(4):3265–3278, April 2021. doi: 10.1021/acsaem.0c03039.

[42] Mark S. Hybertsen and Steven G. Louie. Electron correlation in semiconductors and insulators: Band gaps and quasiparticle energies. *Phys. Rev. B*, 34 (8):5390–5413, October 1986. doi: 10.1103/PhysRevB.34.5390.

[43] Michael Rohlfing and Steven G. Louie. Electron-hole excitations and optical spectra from first principles. *Phys. Rev. B*, 62(8):4927–4944, August 2000. doi: 10.1103/PhysRevB.62.4927.

[44] Jack Deslippe, Georgy Samsonidze, David A. Strubbe, Manish Jain, Marvin L. Cohen, and Steven G. Louie. BerkeleyGW: A massively parallel computer package for the calculation of the quasiparticle and optical properties of materials and nanostructures. *Computer Physics Communications*, 183(6): 1269–1289, June 2012. ISSN 0010-4655. doi: 10.1016/j.cpc.2011.12.006.

[45] Diana Y. Qiu, Felipe H. da Jornada, and Steven G. Louie. Optical Spectrum of ${\mathrm{MoS}}_{2}$: Many-Body Effects and Diversity of Exciton States. *Phys. Rev. Lett.*, 111(21):216805, November 2013. doi: 10.1103/PhysRevLett.111.216805.

[46] J. C. G. Henriques and N. M. R. Peres. Excitons in phosphorene: A semi-analytical perturbative approach. *Phys. Rev. B*, 101(3):035406, January 2020. doi: 10.1103/PhysRevB.101.035406.

[47] G. Dresselhaus. Effective mass approximation for excitons. *Journal of Physics and Chemistry of Solids*, 1(1):14–22, September 1956. ISSN 0022-3697. doi: 10.1016/0022-3697(56)90004-X.

[48] A. B. Kunz and C. P. Flynn. A new configuration interaction method for excitons and interband processes applied to LiF. *J. Phys. C: Solid State Phys.*, 16(9):1659, March 1983. ISSN 0022-3719. doi: 10.1088/0022-3719/16/9/010.

[49] Tomislav Piteša, Severin Polonius, Leticia González, and Sebastian Mai. Excitonic Configuration Interaction: Going Beyond the Frenkel Exciton Model. *J. Chem. Theory Comput.*, 20(13):5609–5634, July 2024. ISSN 1549-9618. doi: 10.1021/acs.jctc.4c00157.

[50] Maciej Bieniek, Katarzyna Sadecka, Ludmiła Szulakowska, and Paweł Hawrylak. Theory of Excitons in Atomically Thin Semiconductors: Tight-Binding Approach. *Nanomaterials*, 12(9):1582, January 2022. ISSN 2079-4991. doi: 10.3390/nano12091582.

[51] Alexandre C. Dias, Julian F. R. V. Silveira, and Fanyao Qu. WanTiBEXOS: A Wannier based Tight Binding code for electronic band structure, excitonic and optoelectronic properties of solids. *Computer Physics Communications*, 285:108636, April 2023. ISSN 0010-4655. doi: 10.1016/j.cpc.2022.108636.

[52] Qi Wei, Jinhui Chen, Ping Ding, Bo Shen, Jiang Yin, Fei Xu, Yidong Xia, and Zhiguo Liu. Synthesis of easily transferred 2d layered bii3 nanoplates for flexible visible-light photodetectors. *ACS Appl. Mater. Interfaces*, 10(25): 21527–21533, June 2018. ISSN 1944-8244. doi: 10.1021/acsami.8b02582.

[53] Martin Grönke, Danny Pohflepp, Peer Schmidt, Martin Valldor, Steffen Oswald, Daniel Wolf, Qi Hao, Udo Steiner, Bernd Büchner, and Silke Hampel. Simulation and synthesis of α-$MoCl_3$ nanosheets on substrates by short time chemical vapor transport. *Nano-Structures & Nano-Objects*, 19:100324, July 2019. ISSN 2352-507X. doi: 10.1016/j.nanoso.2019.100324.

[54] Shaolong Jiang, Gang Wang, Hanbing Deng, Kai Liu, Qishuo Yang, Erding Zhao, Liang Zhu, Weiteng Guo, Jing Yang, Cheng Zhang, Heshen Wang, Xi Zhang, Jun-Feng Dai, Guangfu Luo, Yue Zhao, and Junhao Lin. General synthesis of 2d magnetic transition metal dihalides via trihalide reduction. *ACS Nano*, 17(1):363–371, January 2023. ISSN 1936-0851. doi: 10.1021/acsnano.2c08693.

[55] Michael A. McGuire, Jiaqiang Yan, Paula Lampen-Kelley, Andrew F. May, Valentino R. Cooper, Lucas Lindsay, Alexander Puretzky, Liangbo Liang, Santosh KC, Ercan Cakmak, Stuart Calder, and Brian C. Sales. High-temperature magnetostructural transition in van der waals-layered $\alpha = MoCl_3$. *Phys. Rev. Materials*, 1(6):064001, November 2017. doi: 10.1103/PhysRevMaterials.1.064001.

[56] Jia Li, Xun Guan, Chen Wang, Hung-Chieh Cheng, Ruoqi Ai, Kangkang Yao, Peng Chen, Zhengwei Zhang, Xidong Duan, and Xiangfeng Duan. Synthesis of 2D Layered BiI3 Nanoplates, BiI3/WSe2van der Waals Heterostructures

and Their Electronic, Optoelectronic Properties. *Small*, 13(38):1701034, 2017. ISSN 1613-6829. doi: 10.1002/smll.201701034.

[57] Qun Fan, Jiawei Huang, Ningning Dong, Song Hong, Chao Yan, Yongchao Liu, Jieshan Qiu, Jun Wang, and Zhenyu Sun. Liquid Exfoliation of Two-Dimensional PbI2 Nanosheets for Ultrafast Photonics. *ACS Photonics*, 6(4): 1051–1057, April 2019. doi: 10.1021/acsphotonics.9b00122.

[58] Zeguo Lin, Wei Zheng, and Feng Huang. Narrow band emission from layered α-HgI2 micro-/nano-sheets with high Huang-Rhys factor. *Journal of Luminescence*, 237:118161, September 2021. ISSN 0022-2313. doi: 10.1016/j.jlumin.2021.118161.

[59] Manlin Tan, Chao Hu, Yang Lan, Jahangeer Khan, Hui Deng, Xiaokun Yang, Peixiang Wang, Xiangxiang Yu, Jianjun Lai, and Haisheng Song. 2d lead dihalides for high-performance ultraviolet photodetectors and their detection mechanism investigation. *Small*, 13(47):1702024, 2017. ISSN 1613-6829. doi: 10.1002/smll.201702024.

[60] Wei Zheng, Zhaojun Zhang, Richeng Lin, Kai Xu, Jun He, and Feng Huang. High-crystalline 2d layered pbi2 with ultrasmooth surface: Liquid-phase synthesis and application of high-speed photon detection. *Advanced Electronic Materials*, 2(11):1600291, 2016. ISSN 2199-160X. doi: 10.1002/aelm.201600291.

[61] Han Ju Lee, Seonjeong Lee, Yena Ji, Kyung Gook Cho, Kyoung Soon Choi, Cheolho Jeon, Keun Hyung Lee, and Kihyon Hong. Ultrahigh-mobility and solution-processed inorganic p-channel thin-film transistors based on a transition-metal halide semiconductor. *ACS Appl. Mater. Interfaces*, 11(43): 40243–40251, October 2019. ISSN 1944-8244. doi: 10.1021/acsami.9b12654.

[62] Danrui Ni, Kasey P. Devlin, Guangming Cheng, Xin Gui, Weiwei Xie, Nan Yao, and Robert J. Cava. The honeycomb and hyperhoneycomb polymorphs of iri3. *Journal of Solid State Chemistry*, 312:123240, August 2022. ISSN 0022-4596. doi: 10.1016/j.jssc.2022.123240.

[63] Lang Peng, Jianzhou Zhao, Min Cai, Gui-Yuan Hua, Zhen-Yu Liu, Hui-Nan Xia, Yuan Yuan, Wen-Hao Zhang, Gang Xu, Ling-Xiao Zhao, Zeng-Wei Zhu,

Tao Xiang, and Ying-Shuang Fu. Mott phase in a van der waals transition-metal halide at single-layer limit. *Phys. Rev. Research*, 2(2):023264, June 2020. doi: 10.1103/PhysRevResearch.2.023264.

[64] Stefania Sandoval, Elzbieta Pach, Belén Ballesteros, and Gerard Tobias. Encapsulation of two-dimensional materials inside carbon nanotubes: Towards an enhanced synthesis of single-layered metal halides. *Carbon*, 123:129–134, October 2017. ISSN 0008-6223. doi: 10.1016/j.carbon.2017.07.031.

[65] Fakun Wang, Zhuang Zhang, Yue Zhang, Anmin Nie, Wei Zhao, Dong Wang, Fuqiang Huang, and Tianyou Zhai. Honeycomb rhi3 flakes with high environmental stability for optoelectronics. *Advanced Materials*, 32(25):2001979, 2020. ISSN 1521-4095. doi: 10.1002/adma.202001979.

[66] Xinkai Ding, Yinglu Jia, and Gaoyang Gou. Two-dimensional ferroelasticity and domain-wall flexoelectricity in hgx2 (x = br or i) monolayers. *J. Phys. Chem. Lett.*, 14(2):420–429, January 2023. doi: 10.1021/acs.jpclett.2c03605.

[67] Xingyong Huang, Liujiang Zhou, Luo Yan, You Wang, Wei Zhang, Xiumin Xie, Qiang Xu, and Hai-Zhi Song. HfX2 (X = Cl, Br, I) Monolayer and Type II Heterostructures with Promising Photovoltaic Characteristics*. *Chinese Phys. Lett.*, 37(12):127101, December 2020. ISSN 0256-307X. doi: 10.1088/0256-307X/37/12/127101.

[68] Qiang Fan, Jianhui Yang, and Ning Wang. Theoretical Prediction of the Monolayer Hf2Br4 as Promising Thermoelectric Material. *Materials*, 15(12): 4120, January 2022. ISSN 1996-1944. doi: 10.3390/ma15124120.

[69] Xingyong Huang, Luo Yan, Yong Zhou, You Wang, Hai-Zhi Song, and Liujiang Zhou. Group 11 transition-metal halide monolayers: High promises for photocatalysis and quantum cutting. *J. Phys. Chem. Lett.*, 12(1):525–531, January 2021. doi: 10.1021/acs.jpclett.0c03138.

[70] Xingyong Huang, Luo Yan, Yong Zhou, Wei Zhang, Xiumin Xie, Qiang Xu, You Wang, Liujiang Zhou, and Haizhi Song. Tix2 (x=cl, br, i) monolayer and type ii heterostructures as promising efficient solar cells. In *International Conference on Optoelectronic and Microelectronic Technology and Application*, volume 11617, pages 578–583. SPIE, December 2020. doi: 10.1117/12.2585304.

[71] Hui Tang, Yuhong Huang, Hongkuan Yuan, and Hong Chen. Layered ticl2 monolayer as an antiferromagnetic semiconductor. *SPIN*, 12(01):2250004, March 2022. ISSN 2010-3247. doi: 10.1142/S2010324722500047.

[72] Xingyong Huang, Zhiwen Zhuo, Luo Yan, You Wang, Nan Xu, Hai-Zhi Song, and Liujiang Zhou. Single-layer zirconium dihalides zrx2 (x = cl, br, and i) with abnormal ferroelastic behavior and strong anisotropic light absorption ability. *J. Phys. Chem. Lett.*, 12(32):7726–7732, August 2021. doi: 10.1021/acs.jpclett.1c01958.

[73] Ming Jia, Chuan-Lu Yang, Mei-Shan Wang, and Xiao-Guang Ma. High dimensionless figure of merit of the zri2 monolayer identified based on intrinsic carrier concentration and bipolar effect. *Appl. Phys. Lett.*, 121(12):123903, September 2022. ISSN 0003-6951. doi: 10.1063/5.0099495.

[74] Artem V. Kuklin, Lingfeng Gao, Han Zhang, and Hans Ågren. Two-dimensional gold halides: Novel semiconductors with giant spin–orbit splitting and tunable optoelectronic properties. *J. Phys. Chem. Lett.*, 11(22):9759–9765, November 2020. doi: 10.1021/acs.jpclett.0c02788.

[75] Pan Zhang, Jun-Hui Yuan, Wen-Yu Fang, Gang Li, and Jiafu Wang. Two-dimensional v-shaped pdi2: Auxetic semiconductor with ultralow lattice thermal conductivity and ultrafast alkali ion mobility. *Applied Surface Science*, 601:154176, November 2022. ISSN 0169-4332. doi: 10.1016/j.apsusc.2022.154176.

[76] Qilong Sun and Nicholas Kioussis. Prediction of manganese trihalides as two-dimensional dirac half-metals. *Phys. Rev. B*, 97(9):094408, March 2018. doi: 10.1103/PhysRevB.97.094408.

[77] Yelda Kadioglu, Ilkay Ozdemir, Olcay Üzengi Aktürk, Gökhan Gökoğlu, Ümit Akıncı, and Ethem Aktürk. Tuning the electronic structure of rhx3 (x = cl, br, i) nonmagnetic monolayers: effects of charge-injection and external strain. *Phys. Chem. Chem. Phys.*, 22(8):4561–4573, February 2020. ISSN 1463-9084. doi: 10.1039/C9CP06240H.

[78] Yaxin Gao, Menghao Wu, and Xiao Cheng Zeng. Phase transitions and ferroelasticity–multiferroicity in bulk and two-dimensional silver and copper

monohalides. *Nanoscale Horiz.*, 4(5):1106–1112, August 2019. ISSN 2055-6764. doi: 10.1039/C9NH00172G.

[79] Vadym V. Kulish and Wei Huang. Single-layer metal halides MX2 (X = Cl, Br, I): Stability and tunable magnetism from first principles and Monte Carlo simulations. *J. Mater. Chem. C*, 5(34):8734–8741, August 2017. ISSN 2050-7534. doi: 10.1039/C7TC02664A.

[80] Ling Yue, Wenyuan Jin, Ai-Jie Mao, and Xiaoyu Kuang. Single-layer mx2 (m = zn, cd and x = cl, i): Auxetic semiconductors with strain-tunable optoelectronic properties. *J. Phys. Chem. C*, 125(23):12983–12990, June 2021. ISSN 1932-7447. doi: 10.1021/acs.jpcc.1c02736.

[81] Fatih Ersan, Erol Vatansever, Sevil Sarikurt, Yusuf Yüksel, Yelda Kadioglu, H. Duygu Ozaydin, Olcay Üzengi Aktürk, Ümit Akıncı, and Ethem Aktürk. Exploring the electronic and magnetic properties of new metal halides from bulk to two-dimensional monolayer: Rux3 (x = br, i). *Journal of Magnetism and Magnetic Materials*, 476:111–119, April 2019. ISSN 0304-8853. doi: 10.1016/j.jmmm.2018.12.032.

[82] Ke Xu, Haifei Qin, Jiao Chen, Xinyong Cai, Panlong Kong, Li Liu, Bai Sun, and Yuanzheng Chen. Metal halide hgi2 monolayer with auxetic property and photocatalysis application. *Computational Materials Science*, 219:112007, February 2023. ISSN 0927-0256. doi: 10.1016/j.commatsci.2023.112007.

[83] Yuqiang Fang, Lingping Kong, Ruiqi Wang, Zhuang Zhang, Zhongyang Li, Yanhui Wu, Kejun Bu, Xuqiang Liu, Shuai Yan, Takanori Hattori, Nana Li, Kuo Li, Gang Liu, and Fuqiang Huang. Pressure engineering of van der Waals compound RhI3: Bandgap narrowing, metallization, and remarkable enhancement of photoelectric activity. *Materials Today Physics*, 34:101083, May 2023. ISSN 2542-5293. doi: 10.1016/j.mtphys.2023.101083.

[84] Zhipeng Yan, Ketao Yin, Zhenhai Yu, Xin Li, Mingtao Li, Ye Yuan, Xiaodong Li, Ke Yang, Xiaoli Wang, and Lin Wang. Pressure-induced band-gap closure and metallization in two-dimensional transition metal halide cdi2. *Applied Materials Today*, 18:100532, March 2020. ISSN 2352-9407. doi: 10.1016/j.apmt.2019.100532.

[85] Sushree Sarita Sahoo, Vineet Kumar Sharma, Mayanak K. Gupta, Ranjan Mittal, and V. Kanchana. High thermopower and birefringence in layered mercury-based halides. *Materials Today Communications*, 32:102824, August 2022. ISSN 2352-4928. doi: 10.1016/j.mtcomm.2021.102824.

[86] Swagata Acharya, Dimitar Pashov, Alexander N. Rudenko, Malte Rösner, Mark van Schilfgaarde, and Mikhail I. Katsnelson. Real- and momentum-space description of the excitons in bulk and monolayer chromium tri-halides. *npj 2D Mater Appl*, 6(1):1–10, May 2022. ISSN 2397-7132. doi: 10.1038/s41699-022-00307-7.

[87] M. Grzeszczyk, S. Acharya, D. Pashov, Z. Chen, K. Vaklinova, M. van Schilfgaarde, K. Watanabe, T. Taniguchi, K. S. Novoselov, M. I. Katsnelson, and M. Koperski. Strongly Correlated Exciton-Magnetization System for Optical Spin Pumping in CrBr3 and CrI3. *Advanced Materials*, 35(17):2209513, 2023. ISSN 1521-4095. doi: 10.1002/adma.202209513.

[88] Xiuwen Zhao, Fujun Liu, Junfeng Ren, and Fanyao Qu. Valleytronic and magneto-optical properties of janus and conventional TiBrI/Cri_3 and TiX_2/Cri_3 ($x = \mathrm{Br}, \mathrm{I}$) heterostructures. *Phys. Rev. B*, 104(8):085119, August 2021. doi: 10.1103/PhysRevB.104.085119.

[89] Sten Haastrup, Mikkel Strange, Mohnish Pandey, Thorsten Deilmann, Per S. Schmidt, Nicki F. Hinsche, Morten N. Gjerding, Daniele Torelli, Peter M. Larsen, Anders C. Riis-Jensen, Jakob Gath, Karsten W. Jacobsen, Jens Jørgen Mortensen, Thomas Olsen, and Kristian S. Thygesen. The computational 2d materials database: high-throughput modeling and discovery of atomically thin crystals. *2D Mater.*, 5(4):042002, September 2018. ISSN 2053-1583. doi: 10.1088/2053-1583/aacfc1.

[90] Morten Niklas Gjerding, Alireza Taghizadeh, Asbjørn Rasmussen, Sajid Ali, Fabian Bertoldo, Thorsten Deilmann, Nikolaj Rørbæk Knøsgaard, Mads Kruse, Ask Hjorth Larsen, Simone Manti, Thomas Garm Pedersen, Urko Petralanda, Thorbjørn Skovhus, Mark Kamper Svendsen, Jens Jørgen Mortensen, Thomas Olsen, and Kristian Sommer Thygesen. Recent progress of the computational 2d materials database (c2db). *2D Mater.*, 8(4):044002, July 2021. ISSN 2053-1583. doi: 10.1088/2053-1583/ac1059.

[91] David Sholl and Janice Steckel. Density functional theory - a practical introduction. In *Density Functional Theory: A Practical Introduction | Wiley*, page 1. John Wiley \& Sons, Inc, 2009. ISBN 978 0 470 37317 0.

[92] Feliciano Giustino. *Materials Modelling Using Density Functional Theory: Properties and Predictions*. Oxford University Press, 2014. ISBN 978-0-19-966244-9.

[93] M. Born and R. Oppenheimer. Zur Quantentheorie der Molekeln. *Annalen der Physik*, 389(20):457–484, 1927. ISSN 1521-3889. doi: 10.1002/andp.19273892002.

[94] William H. Press. *Numerical Recipes 3rd Edition: The Art of Scientific Computing*. Cambridge University Press, September 2007. ISBN 978-0-521-88068-8.

[95] Pragya Verma and Donald G. Truhlar. Status and Challenges of Density Functional Theory. *Trends in Chemistry*, 2(4):302–318, April 2020. ISSN 2589-5974. doi: 10.1016/j.trechm.2020.02.005.

[96] P. Hohenberg and W. Kohn. Inhomogeneous electron gas. *Phys. Rev.*, 136 (3B):B864, November 1964. doi: 10.1103/PhysRev.136.B864.

[97] Richard M. Martin. *Electronic Structure: Basic Theory and Practical Methods*. Cambridge University Press, August 2020. ISBN 978-1-108-42990-0.

[98] W. Kohn and L. J. Sham. Self-consistent equations including exchange and correlation effects. *Phys. Rev.*, 140(4A):A1133, November 1965. doi: 10.1103/PhysRev.140.A1133.

[99] John P. Perdew and Yue Wang. Accurate and simple analytic representation of the electron-gas correlation energy. *Phys. Rev. B*, 45(23):13244–13249, June 1992. doi: 10.1103/PhysRevB.45.13244.

[100] John P. Perdew, Kieron Burke, and Matthias Ernzerhof. Generalized gradient approximation made simple. *Phys. Rev. Lett.*, 77(18):3865, 1996. doi: 10.1103/PhysRevLett.77.3865.

[101] Hai Xiao, Jamil Tahir-Kheli, and William A. III Goddard. Accurate Band Gaps for Semiconductors from Density Functional Theory. *J. Phys. Chem. Lett.*, 2(3):212–217, February 2011. doi: 10.1021/jz101565j.

[102] Felix Bloch. Über die Quantenmechanik der Elektronen in Kristallgittern. *Z. Physik*, 52(7):555–600, July 1929. ISSN 0044-3328. doi: 10.1007/BF01339455.

[103] Neil W. Ashcroft and N. David Mermin. *Solid State Physics*. Holt, Rinehart and Winston, 1976. ISBN 978-0-03-083993-1.

[104] David Vanderbilt. Soft self-consistent pseudopotentials in a generalized eigenvalue formalism. *Phys. Rev. B*, 41(11):7892–7895, April 1990. doi: 10.1103/PhysRevB.41.7892.

[105] G. Kresse and J. Hafner. Norm-conserving and ultrasoft pseudopotentials for first-row and transition elements. *J. Phys.: Condens. Matter*, 6(40):8245, October 1994. ISSN 0953-8984. doi: 10.1088/0953-8984/6/40/015.

[106] O. Krogh Andersen. Linear methods in band theory. *Phys. Rev. B*, 12(8): 3060–3083, October 1975. doi: 10.1103/PhysRevB.12.3060.

[107] Emilia Ridolfi, Caio H. Lewenkopf, and Vitor M. Pereira. Excitonic structure of the optical conductivity in ${\mathrm{MoS}}_{2}$ monolayers. *Phys. Rev. B*, 97(20):205409, May 2018. doi: 10.1103/PhysRevB.97.205409.

[108] Chi Sin Tang, Xinmao Yin, Ming Yang, Di Wu, Muhammad Danang Birowosuto, Jing Wu, Changjian Li, Chathuranga Hettiarachchi, Xin Yu Chin, Yung-Huang Chang, Fangping Ouyang, Cuong Dang, Stephen J. Pennycook, Yuan Ping Feng, Shijie Wang, Dongzhi Chi, Mark B. H. Breese, Wenjing Zhang, Andrivo Rusydi, and Andrew T. S. Wee. Three-Dimensional Resonant Exciton in Monolayer Tungsten Diselenide Actuated by Spin–Orbit Coupling. *ACS Nano*, 13(12):14529–14539, December 2019. ISSN 1936-0851. doi: 10.1021/acsnano.9b08385.

[109] Carlos M. O. Bastos, Fernando P. Sabino, Guilherme M. Sipahi, and Juarez L. F. Da Silva. A comprehensive study of g-factors, elastic, structural and electronic properties of III-V semiconductors using hybrid-density functional theory. *Journal of Applied Physics*, 123(6):065702, February 2018. ISSN 0021-8979. doi: 10.1063/1.5018325.

[110] Soner Steiner, Sergii Khmelevskyi, Martijn Marsmann, and Georg Kresse. Calculation of the magnetic anisotropy with projected-augmented-wave methodology and the case study of disordered ${\mathrm{Fe}}_{1\ensuremath{-

}x}{\mathrm{Co}}_{x}$ alloys. *Phys. Rev. B*, 93(22):224425, June 2016. doi: 10.1103/PhysRevB.93.224425.

[111] Jose David M. Vianna, Adalberto Fazzio, and Sylvio Canuto. Teoria quântica de moléculas e sólidos: simulação computacional. In *Teoria quântica de moléculas e sólidos: simulação computacional*, page 1. Livraria da Física, 2004. ISBN 978-85-88325-16-6.

[112] Nicola Marzari and David Vanderbilt. Maximally localized generalized wannier functions for composite energy bands. *Phys. Rev. B*, 56(20):12847–12865, November 1997. doi: 10.1103/PhysRevB.56.12847.

[113] E. E. Salpeter and H. A. Bethe. A Relativistic Equation for Bound-State Problems. *Phys. Rev.*, 84(6):1232–1242, December 1951. doi: 10.1103/PhysRev.84.1232.

[114] G. Kresse and J. Furthmüller. Efficient iterative schemes for ab initio total-energy calculations using a plane-wave basis set. *Phys. Rev. B*, 54(16):11169, October 1996. doi: 10.1103/PhysRevB.54.11169.

[115] J. Hafner and G. Kresse. The Vienna AB-Initio Simulation Program VASP: An Efficient and Versatile Tool for Studying the Structural, Dynamic, and Electronic Properties of Materials. In Antonios Gonis, Annemarie Meike, and Patrice E. A. Turchi, editors, *Properties of Complex Inorganic Solids*, pages 69–82. Springer US, Boston, MA, 1997. ISBN 978-1-4615-5943-6. doi: 10.1007/978-1-4615-5943-6_10.

[116] Jochen Heyd, Gustavo E. Scuseria, and Matthias Ernzerhof. Hybrid functionals based on a screened coulomb potential. *The Journal of Chemical Physics*, 118(18):8207–8215, April 2003. ISSN 0021-9606. doi: 10.1063/1.1564060.

[117] Jochen Heyd, Gustavo E. Scuseria, and Matthias Ernzerhof. Erratum: "hybrid functionals based on a screened coulomb potential" [j. chem. phys. 118, 8207 (2003)]. *J. Chem. Phys.*, 124(21):219906, June 2006. ISSN 0021-9606. doi: 10.1063/1.2204597.

[118] Ivo Souza, Nicola Marzari, and David Vanderbilt. Maximally localized wannier functions for entangled energy bands. *Phys. Rev. B*, 65(3):035109, December 2001. doi: 10.1103/PhysRevB.65.035109.

[119] Arash A. Mostofi, Jonathan R. Yates, Giovanni Pizzi, Young-Su Lee, Ivo Souza, David Vanderbilt, and Nicola Marzari. An updated version of wannier90: A tool for obtaining maximally-localised Wannier functions. *Computer Physics Communications*, 185(8):2309–2310, August 2014. ISSN 0010-4655. doi: 10.1016/j.cpc.2014.05.003.

[120] Giovanni Pizzi, Valerio Vitale, Ryotaro Arita, Stefan Blügel, Frank Freimuth, Guillaume Géranton, Marco Gibertini, Dominik Gresch, Charles Johnson, Takashi Koretsune, Julen Ibañez-Azpiroz, Hyungjun Lee, Jae-Mo Lihm, Daniel Marchand, Antimo Marrazzo, Yuriy Mokrousov, Jamal I. Mustafa, Yoshiro Nohara, Yusuke Nomura, Lorenzo Paulatto, Samuel Poncé, Thomas Ponweiser, Junfeng Qiao, Florian Thöle, Stepan S. Tsirkin, Malgorzata Wierzbowska, Nicola Marzari, David Vanderbilt, Ivo Souza, Arash A. Mostofi, and Jonathan R. Yates. Wannier90 as a community code: new features and applications. *J. Phys.: Condens. Matter*, 32(16):165902, January 2020. ISSN 0953-8984. doi: 10.1088/1361-648X/ab51ff.

[121] J. Enkovaara, C. Rostgaard, J. J. Mortensen, J. Chen, M. Dułak, L. Ferrighi, J. Gavnholt, C. Glinsvad, V. Haikola, H. A. Hansen, H. H. Kristoffersen, M. Kuisma, A. H. Larsen, L. Lehtovaara, M. Ljungberg, O. Lopez-Acevedo, P. G. Moses, J. Ojanen, T. Olsen, V. Petzold, N. A. Romero, J. Stausholm-Møller, M. Strange, G. A. Tritsaris, M. Vanin, M. Walter, B. Hammer, H. Häkkinen, G. K. H. Madsen, R. M. Nieminen, J. K. Nørskov, M. Puska, T. T. Rantala, J. Schiøtz, K. S. Thygesen, and K. W. Jacobsen. Electronic structure calculations with GPAW: A real-space implementation of the projector augmented-wave method. *J. Phys.: Condens. Matter*, 22(25):253202, June 2010. ISSN 0953-8984. doi: 10.1088/0953-8984/22/25/253202.

[122] Ask Hjorth Larsen, Jens Jørgen Mortensen, Jakob Blomqvist, Ivano E. Castelli, Rune Christensen, Marcin Dułak, Jesper Friis, Michael N. Groves, Bjørk Hammer, Cory Hargus, Eric D. Hermes, Paul C. Jennings, Peter Bjerre Jensen, James Kermode, John R. Kitchin, Esben Leonhard Kolsbjerg, Joseph Kubal, Kristen Kaasbjerg, Steen Lysgaard, Jón Bergmann Maronsson, Tristan Maxson, Thomas Olsen, Lars Pastewka, Andrew Peterson, Carsten Rostgaard, Jakob Schiøtz, Ole Schütt, Mikkel Strange, Kristian S. Thygesen, Tejs Vegge, Lasse Vilhelmsen, Michael Walter, Zhenhua Zeng, and Karsten W. Jacobsen. The atomic simulation environment—a Python library for working with atoms.

J. Phys.: Condens. Matter, 29(27):273002, June 2017. ISSN 0953-8984. doi: 10.1088/1361-648X/aa680e.

[123] Pedro Borlido, Thorsten Aull, Ahmad W. Huran, Fabien Tran, Miguel A. L. Marques, and Silvana Botti. Large-Scale Benchmark of Exchange–Correlation Functionals for the Determination of Electronic Band Gaps of Solids. *J. Chem. Theory Comput.*, 15(9):5069–5079, September 2019. ISSN 1549-9618. doi: 10.1021/acs.jctc.9b00322.

[124] William Shockley and Hans J. Queisser. Detailed balance limit of efficiency of p-n junction solar cells. *Journal of Applied Physics*, 32(3):510–519, March 1961. ISSN 0021-8979. doi: 10.1063/1.1736034.

[125] Ioanna Pallikara, Prakriti Kayastha, Jonathan M. Skelton, and Lucy D. Whalley. The physical significance of imaginary phonon modes in crystals. *Electron. Struct.*, 4(3):033002, July 2022. ISSN 2516-1075. doi: 10.1088/2516-1075/ac78b3.

[126] Yilong Wang, Pengru Huang, Jiaxi Liu, Hongliang Peng, Yongjin Zou, Hailiang Chu, Yao He, Fen Xu, and Lixian Sun. First-principle calculations of lithium adsorption and diffusion on titanium-based monolayers. *Chemical Physics*, 539:110956, November 2020. ISSN 0301-0104. doi: 10.1016/j.chemphys.2020.110956.

[127] Y. Yekta, H. Hadipour, E. Şaşıoğlu, C. Friedrich, S. A. Jafari, S. Blügel, and I. Mertig. Strength of effective coulomb interaction in two-dimensional transition-metal halides mX_2 and mX_3 (m = Ti, v, cr, mn, fe, co, ni; x = Cl, br, i). *Phys. Rev. Mater.*, 5(3):034001, March 2021. doi: 10.1103/PhysRevMaterials.5.034001.

[128] Xiaoping Wang, Hangbo Qi, Ning Wang, Zishen Wang, Wenkai Tang, Zhihai Tan, Zhe Zhu, Meng Zhang, and Chen Shen. Unexpectedly high thermoelectric performance of anisotropic zr2cl4 monolayer. *J. Phys.: Condens. Matter*, 35 (39):394001, June 2023. ISSN 0953-8984. doi: 10.1088/1361-648X/acdb1f.

[129] Shoujian Wu, Aolin Li, Zhixiong Yang, and Fangping Ouyang. Electronic structures and magnetic properties of 3d transition metal doped monolayer rhi3. *Chemical Physics Letters*, 799:139643, July 2022. ISSN 0009-2614. doi: 10.1016/j.cplett.2022.139643.

[130] Bingke Li, Yongsheng Yang, Zhehao Sun, Hangbo Qi, Zhihui Xiong, Keliang Wu, Huanxin Li, Kenan Sun, Xiuchan Xiao, Chen Shen, and Ning Wang. First-Principles Investigation on the Significant Anisotropic Thermoelectric Transport Performance of a Hf2Cl4 Monolayer. *J. Phys. Chem. C*, 126(1): 525–533, January 2022. ISSN 1932-7447. doi: 10.1021/acs.jpcc.1c07301.

[131] Mateus B. P. Querne, Jean M. Bracht, Juarez L. F. Da Silva, Anderson Janotti, and Matheus P. Lima. Crystal structure and electrical and optical properties of two-dimensional group-IV monochalcogenides. *Phys. Rev. B*, 108(8):085409, August 2023. doi: 10.1103/PhysRevB.108.085409.

[132] Rafael Costa-Amaral, Ahmad Forhat, Naidel A. M. S. Caturello, and Juarez L. F. Da Silva. Unveiling the adsorption properties of 3d, 4d, and 5d metal adatoms on the mos2 monolayer: A dft-d3 investigation. *Surface Science*, 701: 121700, November 2020. ISSN 0039-6028. doi: 10.1016/j.susc.2020.121700.

[133] D. Meneses-Gustin, Luis Cabral, Matheus P. Lima, Juarez L. F. Da Silva, Emanuela Margapoti, Sergio E. Ulloa, Gilmar E. Marques, and Victor Lopez-Richard. Photomodulation of transport in monolayer dichalcogenides. *Phys. Rev. B*, 98(24):241403, December 2018. doi: 10.1103/PhysRevB.98.241403.

[134] Matheus P. Lima, Naidel A. M. S. Caturello, and Juarez L. F. Da Silva. Ab initio investigation of the interface between $Mo_{10}S_{24}$ nanoflakes and the Au(111) surface: Interplay between interaction energy and morphology. *Applied Surface Science*, 604:154413, December 2022. ISSN 0169-4332. doi: 10.1016/j.apsusc.2022.154413.

[135] Alexey Tal, Peitao Liu, Georg Kresse, and Alfredo Pasquarello. Accurate optical spectra through time-dependent density functional theory based on screening-dependent hybrid functionals. *Phys. Rev. Res.*, 2(3):032019, July 2020. doi: 10.1103/PhysRevResearch.2.032019.

[136] Yugui Yao, Fei Ye, Xiao-Liang Qi, Shou-Cheng Zhang, and Zhong Fang. Spin-orbit gap of graphene: First-principles calculations. *Phys. Rev. B*, 75(4): 041401, January 2007. doi: 10.1103/PhysRevB.75.041401.

[137] Kin Fai Mak, Di Xiao, and Jie Shan. Light–valley interactions in 2D semiconductors. *Nature Photon*, 12(8):451–460, August 2018. ISSN 1749-4893. doi: 10.1038/s41566-018-0204-6.

[138] Weijie Zhao, Ricardo Mendes Ribeiro, and Goki Eda. Electronic Structure and Optical Signatures of Semiconducting Transition Metal Dichalcogenide Nanosheets. *Acc. Chem. Res.*, 48(1):91–99, January 2015. ISSN 0001-4842. doi: 10.1021/ar500303m.

[139] Guilherme Ribeiro Portugal and Jeverson Teodoro Arantes. Hybrid Functional-Based Scissors Operator for Perovskite Oxide Nanostructures: A NaTaO3 Case Study. *J. Phys. Chem. C*, 127(11):5604–5612, March 2023. ISSN 1932-7447. doi: 10.1021/acs.jpcc.2c08986.

[140] Thomas Olsen. Unified Treatment of Magnons and Excitons in Monolayer ${\mathrm{CrI}}_{3}$ from Many-Body Perturbation Theory. *Phys. Rev. Lett.*, 127(16):166402, October 2021. doi: 10.1103/PhysRevLett.127.166402.

[141] Joon Young Kwak. Absorption coefficient estimation of thin MoS2 film using attenuation of silicon substrate Raman signal. *Results in Physics*, 13:102202, June 2019. ISSN 2211-3797. doi: 10.1016/j.rinp.2019.102202.

[142] Martin A. Green and Mark J. Keevers. Optical properties of intrinsic silicon at 300 K. *Progress in Photovoltaics: Research and Applications*, 3(3):189–192, 1995. ISSN 1099-159X. doi: 10.1002/pip.4670030303.

[143] D. Jérome, T. M. Rice, and W. Kohn. Excitonic Insulator. *Phys. Rev.*, 158 (2):462–475, June 1967. doi: 10.1103/PhysRev.158.462.

[144] R. L. Anderson. Germanium-Gallium Arsenide Heterojunctions [Letter to the Editor]. *IBM Journal of Research and Development*, 4(3):283–287, July 1960. ISSN 0018-8646. doi: 10.1147/rd.43.0283.

[145] Marco Bernardi, Maurizia Palummo, and Jeffrey C. Grossman. Semiconducting Monolayer Materials as a Tunable Platform for Excitonic Solar Cells. *ACS Nano*, 6(11):10082–10089, November 2012. ISSN 1936-0851. doi: 10.1021/nn303815z.

[146] Zhiyang Zhang, Lixiang Han, Zhiying Dan, Hengyi Li, Mengmeng Yang, Yiming Sun, Zhaoqiang Zheng, Nengjie Huo, Dongxiang Luo, Wei Gao, and Jingbo Li. Type II Homo-Type Bi2O2Se Nanosheet/InSe Nanoflake Heterostructures for Self-Driven Broadband Visible–Near-Infrared Photodetectors. *ACS Appl. Nano Mater.*, 6(6):4573–4583, March 2023. doi: 10.1021/acsanm.3c00054.

[147] Emek G. Durmusoglu, Sujuan Hu, Pedro Ludwig Hernandez-Martinez, Merve Izmir, Farzan Shabani, Min Guo, Huayu Gao, Furkan Isik, Savas Delikanli, Vijay Kumar Sharma, Baiquan Liu, and Hilmi Volkan Demir. High External Quantum Efficiency Light-Emitting Diodes Enabled by Advanced Heterostructures of Type-II Nanoplatelets. *ACS Nano*, 17(8):7636–7644, April 2023. ISSN 1936-0851. doi: 10.1021/acsnano.3c00046.

[148] Ralf Flückiger, Rickard Lövblom, Maria Alexandrova, Olivier Ostinelli, and Colombo R. Bolognesi. Type-II InP/GaAsSb double-heterojunction bipolar transistors with fMAX > 700 GHz. *Appl. Phys. Express*, 7(3):034105, March 2014. ISSN 1882-0786. doi: 10.7567/APEX.7.034105.

[149] C. W. Lin, D. Y. Wang, Y. Tai, Y. T. Jiang, M. C. Chen, C. C. Chen, Y. J. Yang, and Y. F. Chen. Type-II heterojunction organic/inorganic hybrid non-volatile memory based on FeS2 nanocrystals embedded in poly(3-hexylthiophene). *J. Phys. D: Appl. Phys.*, 44(29):292002, July 2011. ISSN 0022-3727. doi: 10.1088/0022-3727/44/29/292002.

[150] S. Vinoth, P. Mary Rajaitha, and A. Pandikumar. Modulating photoelectrochemical water splitting performance by constructing a type-II heterojunction between g-C3N4 and BiOI. *New J. Chem.*, 45(4):2010–2018, February 2021. ISSN 1369-9261. doi: 10.1039/D0NJ05384H.

[151] G. Kresse and J. Hafner. Ab initio molecular dynamics for open-shell transition metals. *Phys. Rev. B*, 48(17):13115, November 1993. doi: 10.1103/PhysRevB.48.13115.

[152] G. P. Francis and M. C. Payne. Finite basis set corrections to total energy pseudopotential calculations. *J. Phys.: Condens. Matter*, 2(19):4395, May 1990. ISSN 0953-8984. doi: 10.1088/0953-8984/2/19/007.

[153] Hendrik J. Monkhorst and James D. Pack. Special points for brillouin-zone integrations. *Phys. Rev. B*, 13(12):5188, June 1976. doi: 10.1103/PhysRevB.13.5188.

[154] Julian F. R. V. Silveira, Rafael Besse, A. C. Dias, Naidel A. M. S. Caturello, and Juarez L. F. Da Silva. Tailoring Excitonic and Optoelectronic Properties of Transition Metal Dichalcogenide Bilayers. *J. Phys. Chem. C*, 126(21):9173–9184, June 2022. ISSN 1932-7447. doi: 10.1021/acs.jpcc.2c02023.

[155] A. C. Dias, Matheus P. Lima, and Juarez L. F. Da Silva. Role of structural phases and octahedra distortions in the optoelectronic and excitonic properties of csgex3 (x = cl, br, i) perovskites. *J. Phys. Chem. C*, 125(35):19142–19155, September 2021. ISSN 1932-7447. doi: 10.1021/acs.jpcc.1c05245.

[156] Mailde S. Ozório, A. C. Dias, Julian F. R. V. Silveira, and Juarez L. F. Da Silva. Theoretical Investigation of the Role of Anion and Trivalent Cation Substitution in the Physical Properties of Lead-Free Zero-Dimensional Perovskites. *J. Phys. Chem. C*, 126(16):7245–7255, April 2022. ISSN 1932-7447. doi: 10.1021/acs.jpcc.2c00494.

[157] Carlo A. Rozzi, Daniele Varsano, Andrea Marini, Eberhard K. U. Gross, and Angel Rubio. Exact Coulomb cutoff technique for supercell calculations. *Phys. Rev. B*, 73(20):205119, May 2006. doi: 10.1103/PhysRevB.73.205119.

Appendix A

Python Code to Navigate Through C2DB

This appendix shows the Python code used to navigate in the c2db database file (c2db.db). Listing A.1 shows the full code used here. Additionally, listing A.2 presents the use of this code for each step presented in section 3.1.

Listing A.1: c2db.py

```
# External Packages
from ase.db import connect
from operator import itemgetter
from collections import Counter

from ase.spacegroup import get_spacegroup # Function to get
    spacegroup of structure

import argparse # Parse command line arguments
import itertools
import numpy as np # Numpy for math operations
import os # Interact with operating system

# List of transition metals
trans_metals = [ 'Sc', 'Ti', 'V', 'Cr', 'Mn', 'Fe', 'Co', 'Ni', 'Cu
    ', 'Zn', 'Y', 'Zr', 'Nb', 'Mo', 'Tc', 'Ru', 'Rh', 'Pd', 'Ag', '
    Cd', 'La', 'Hf', 'Ta', 'W', 'Re', 'Os', 'Ir', 'Pt', 'Au', 'Hg',
    'Ac', 'Rf', 'Db', 'Sg', 'Bh', 'Hs', 'Mt', 'Ds', 'Rg' ]

# List of properties in C2DB
```

```
list_of_properties = [
  'A', 'E_B', 'E_x', 'E_y', 'E_z', 'J', 'N_nn', 'Topology', 'age', 'alphax', 'alphax_el',
   'alphax_lat', 'alphay', 'alphay_el', 'alphay_lat', 'alphaz', 'alphaz_el', 'alphaz_lat',
   'asr_id', 'c_11', 'c_12', 'c_13', 'c_21', 'c_22', 'c_23', 'c_31', 'c_32', 'c_33',
   'calculator', 'cbm', 'cbm_gw', 'cbm_hse', 'cell_area', 'charge', 'class', 'cod_id',
   'crystal_type', 'dE_zx', 'dE_zy', 'dim_nclusters_0D', 'dim_nclusters_1D', 'dim_nclusters_2D',
   'dim_nclusters_3D', 'dim_primary', 'dim_primary_score', 'dim_score_0123D', 'dim_score_012D',
   'dim_score_013D', 'dim_score_01D', 'dim_score_023D', 'dim_score_02D', 'dim_score_03D',
   'dim_score_0D', 'dim_score_123D', 'dim_score_12D', 'dim_score_13D', 'dim_score_1D',
   'dim_score_23D', 'dim_score_2D', 'dim_score_3D', 'dim_threshold_0D', 'dim_threshold_1D',
   'dim_threshold_2D', 'dipz', 'doi', 'dos_at_ef_nosoc', 'dos_at_ef_soc',
   'dynamic_stability_phonons', 'dynamic_stability_stiffness', 'efermi', 'ehull', 'emass_cb_dir1',
   'emass_cb_dir2', 'emass_vb_dir1', 'emass_vb_dir2', 'energy', 'etot', 'evac', 'evacdiff',
   'first_class_material', 'fmax', 'folder', 'formula', 'gap', 'gap_dir', 'gap_dir_gw',
   'gap_dir_hse', 'gap_dir_nosoc', 'gap_gw', 'gap_hse', 'gap_nosoc', 'has_inversion_symmetry',
   'hform', 'icsd_id', 'id', 'is_magnetic', 'lam', 'magmom', 'magstate', 'mass', 'minhessianeig',
   'natoms', 'nspins', 'pbc', 'plasmafrequency_x', 'plasmafrequency_y', 'pointgroup', 'smax',
   'spacegroup', 'speed_of_sound_x', 'speed_of_sound_y', 'spgnum',
   'spin', 'spin_axis',
   'stoichiometry', 'thermodynamic_stability_level', 'uid', 'unique_id', 'user', 'vbm', 'vbm_gw',
   'vbm_hse', 'volume', 'workfunction'
   ]

# Get command-line arguments
def get_arguments():
  parser = argparse.ArgumentParser(description=
```

```
42                                      'C2DB parser\n\n'
43
44                                      'This script is design to read
    and retrieve cell vectors and atomic cartesian '
45                                      'coordinates from the
    compounds of the c2db database. There are 5 arguments that '
46                                      'can be provided to the script
    in order to configure the desirable query and to '
47                                      'also manage the outputs:\n\n'
48
49              '-- tm: It\'s a options for selected only compound
    with transition metals'
50              'The mode true selected only compounds with transition
    metal.'
51              'The option False select materials that correspond
    with the query'
52
53                                      '-- query: It\'s the query for
    which the database will be parsed. The query '
54                                      'should be presented as a
    single string of text with different parse arguments '
55                                      'being separated by a comma
    and inside quotation marks. For example: '
56                                      '\'stoichiometry=AB2, 0.5<
    gap_hse<3.5\', will retrieve the compounds with '
57                                      'stoichiometry equals to AB2
    and with band gap HSE06 between 0.5 and 3.5 eV.\n\n'
58
59                                      '-- database: The name of the
    database to be parsed. The default name is '
60                                      '\'c2db.db\', but a new name
    can be provided to match the name of the database in '
61                                      'the working folder.\n\n '
62
63                                      '-- key: Property to be
    retrieved from the compounds parsed by the query argument. '
64                                      'The list of possible keys to
    be used can be found in '
65                                      '\'https://cmr.fysik.dtu.dk/
    c2db/c2db.html\'. If a particular compound does not '
66                                      'have the desired property, a
    value of NaN will be assigned to it. The resulting '
```

```
67                                      'values will be saved in a
    folder named after the property and in a text file '
68                                      'also named after the property
    . The text file will have the chemical formula of '
69                                      'the respective compound and
    its property value in a two column scheme:\n\n'
70                                      'Fe2Te2 \tproperty value\n'
71                                      'Ag2O2  \tproperty value\n '
72                                      '...\n\n'
73
74                                      '-- folder: Name of the folder
     to save the results\n\n'
75
76                                      '-- mode: The configuration of
     the saved file with cell vector and cartesian'
77                                      'coordinates information. If
    mode = True (default), the chemical symbols will be'
78                                      'written in the same line as
    its cartesian coordinates:\n\n'
79                                      'Ag    x    y    z\n'
80                                      'Ag    x    y    z\n'
81                                      'O     x    y    z\n'
82                                      'O     x    y    z\n\n'
83                                      'If mode = False, the chemical
     symbol, along with its quantity, will be written '
84                                      'first, followed by the
    cartesian coordinates:\n\n'
85                                      'Ag  O\n'
86                                      '2   2\n'
87                                      '\tx    y    z\n'
88                                      '\tx    y    z\n'
89                                      '\tx    y    z\n'
90                                      '\tx    y    z\n'
91                                      ,
92                                      formatter_class=argparse.
    RawDescriptionHelpFormatter
93                                      )
94
95  parser.add_argument('--query', nargs='+', help='Queries to select
      the compounds in the database')
96  parser.add_argument('--tm', type=str, default='True', help='
     Select materials with transition metals')
```

```
97    parser.add_argument('--database', type=str, default='c2db.db',
       help='The name of the database')
98    parser.add_argument('--key', type=str, default=None, help='
       Property to select among the compounds '
99                                                                 '
       returned by the query')
100   parser.add_argument('--folder', type=str, default='query', help='
       Folder to save the archives with information '
101
        'on the material cell, cartesian coordinates and '
102
        'selected property')
103   parser.add_argument('--mode', type=str, default='True', help='The
        formatting of the final files')
104   return parser.parse_args()
105
106 # Main function
107 def main():
108     args = get_arguments() # Get command-line arguments
109
110     # Check iq query is provide
111     if args.query is None:
112         raise ValueError('A query value should be provided to parse
       the database. For example: '
113                          '\'stoichiometry=AB2, 0.5<gap_hse<3.5\'')
114
115   # connecting to the database
116   db = connect(args.database)
117   # querying the compounds
118   db_select = db.select(args.query[0])
119
120   i=0
121   for row in db_select: # iteract through selected compounds
122     for trans_m in trans_metals: # interact through transition
       metal list
123       if trans_m in row.formula: # Check if the selected halide has
       a transition metal
124         print(row.formula, row.uid, row.spacegroup)
125         i=i+1
126       else:
127         idr = row.id
128   print('number:',i)
129   print("==============")
```

```
130
131 # creates the folder to save the results if it does not exists
132 path = args.folder
133 if not os.path.exists(path):
134   os.mkdir(path)
135
136 # creates a folder to save the coordinates files
137 coordinates_folder = os.path.join(path, 'coordinates')
138 if not os.path.exists(coordinates_folder):
139   os.mkdir(coordinates_folder)
140
141   # creates ase.Atom object
142   atoms = []
143   for row in db_select:
144     atoms.append(row.toatoms())
145
146   # retrieving cell and coordinates
147   for atom in atoms:
148     symbols = atom.get_chemical_symbols()  # chemical symbols
149     positions = atom.get_positions()  # cartesian coordinates
150     cell = atom.get_cell().todict()['array']  # cell
151
152     # sorting chemical symbols
153     symbols_array = np.array(symbols)
154     symbols_array = symbols_array[:, np.newaxis]
155     sym_pos = np.concatenate([symbols_array, positions], axis=1)
156     sym_pos = sorted(sym_pos, key=itemgetter(0))
157
158     i=0
159     for el in str(get_spacegroup(atom)).split()[:]:
160       if el=="setting":
161         break
162       i+=1
163
164     #archive_name = atom.get_chemical_formula()
165     archive_name = "{}_{}".format(atom.get_chemical_formula(),"".
 join(str(get_spacegroup(atom)).split()[1:i]).replace("/", "!"))
166
167     with open(os.path.join(coordinates_folder, archive_name + '.
 txt'), 'w') as file:
168       file.write(str(len(symbols)) + '\n\n')  # number of atoms
169
170       for row in cell:
```

```
171             file.write(f'\t{row[0]:<30} {row[1]:<30} {row[2]}\n')  # cell vectors
172
173         if args.mode.lower() == 'true':
174             file.write('\n\n')
175
176             for row in sym_pos:
177                 file.write(f'{row[0]:<5} {row[1]:<25} {row[2]:<25} {row[3]}\n')  # cartesian coordinates
178
179         elif args.mode.lower() == 'false':
180             file.write('\n\n')
181
182             symbols_dict = sorted(Counter(symbols).most_common())
183             file.write('  '.join([x[0] for x in symbols_dict]))
184             file.write('\n')
185             file.write('   '.join([str(x[1]) for x in symbols_dict]))
186             file.write('\n\n')
187             for row in sym_pos:
188                 file.write(f'{row[1]:<25} {row[2]:<25} {row[3]}\n')  # cartesian coordinates
189
190         else:
191             raise ValueError('The "mode" argument should either be "True" or "False"')
192
193 if args.key is None:
194     print('\nNo property was selected')
195 else:
196     if args.key not in list_of_properties:
197         print(f'\nProperty "{args.key}" not found. The value should be one of the keys in the table '
198               '"key-values pairs" in https://cmr.fysik.dtu.dk/c2db/c2db.html')
199         args.key = None
200
201     else:
202         # creates a folder to save the property file
203         properties_folder = os.path.join(path, args.key)
204
205         if not os.path.exists(properties_folder):
206             os.mkdir(properties_folder)
207
```

```
208         labels = []
209         key_property = []
210 
211         db_select = db.select(args.query[0])
212         for row in db_select:
213           tmp = dict(Counter(row.symbols))
214           tmp = list(itertools.chain(*tmp.items()))
215           labels.append(''.join([str(x) for x in tmp]))
216 
217           try:
218             property_value = eval('row.' + args.key)
219           except:
220             property_value = np.nan
221 
222           key_property.append(property_value)
223 
224 
225           with open(properties_folder + '/' + args.key + '.txt', 'w
    ') as file:
226             for atom, prop in zip(labels, key_property):
227               file.write(f'{atom:<10} {prop}\n')
228 
229 if __name__ == '__main__':
230   main()
```

Listing A.2: run.sh

```
1 #!/bin/bash
2 
3 ##############################
4 ## Query the stoichiometry ##
5 ##############################
6 
7 ## AB:
8 python3 c2db.py --query "stoichiometry=AB, Cl" --tm=True --database
     "c2db-first-class-20210125-nodata.db" --key "stoichiometry" --
    folder="AB-Cl" --mode=False >> out.out
9 python3 c2db.py --query "stoichiometry=AB, Br" --tm=True --database
     "c2db-first-class-20210125-nodata.db" --key "stoichiometry" --
    folder="AB-Br" --mode=False >> out.out
10 python3 c2db.py --query "stoichiometry=AB, I" --tm=True --database
    "c2db-first-class-20210125-nodata.db" --key "stoichiometry" --
    folder="AB-I" --mode=False >> out.out
```

```
11
12 ## AB2:
13 python3 c2db.py --query "stoichiometry=AB2, Cl" --tm=True --
      database "c2db-first-class-20210125-nodata.db" --key "
      stoichiometry" --folder="AB2-Cl" --mode=False >> out.out
14 python3 c2db.py --query "stoichiometry=AB2, Br" --tm=True --
      database "c2db-first-class-20210125-nodata.db" --key "
      stoichiometry" --folder="AB2-Br" --mode=False >> out.out
15 python3 c2db.py --query "stoichiometry=AB2, I" --tm=True --database
       "c2db-first-class-20210125-nodata.db" --key "stoichiometry" --
      folder="AB2-I" --mode=False >> out.out
16
17 ## AB3:
18 python3 c2db.py --query "stoichiometry=AB3, Cl" --tm=True --
      database "c2db-first-class-20210125-nodata.db" --key "
      stoichiometry" --folder="AB3-Cl" --mode=False >> out.out
19 python3 c2db.py --query "stoichiometry=AB3, Br" --tm=True --
      database "c2db-first-class-20210125-nodata.db" --key "
      stoichiometry" --folder="AB3-Br" --mode=False >> out.out
20 python3 c2db.py --query "stoichiometry=AB3, I" --tm=True --database
       "c2db-first-class-20210125-nodata.db" --key "stoichiometry" --
      folder="AB3-I" --mode=False >> out.out
21
22 mkdir 1-Stoichiometry
23 mv AB-Cl AB-Br AB-I AB2-Cl AB2-Br AB2-I AB3-Cl AB3-Br AB3-I 1-
      Stoichiometry
24
25 ####################
26 ## Query bandgap ##
27 ####################
28
29 ## AB:
30 python3 c2db.py --query "stoichiometry=AB, Cl, 0.65<gap_hse<2.12"
      --tm=True --database "c2db-first-class-20210125-nodata.db" --key
       "gap_hse" --folder="AB-Cl" --mode=False >> out.out
31 python3 c2db.py --query "stoichiometry=AB, Br, 0.65<gap_hse<2.12"
      --tm=True --database "c2db-first-class-20210125-nodata.db" --key
       "gap_hse" --folder="AB-Br" --mode=False >> out.out
32 python3 c2db.py --query "stoichiometry=AB, I, 0.65<gap_hse<2.12" --
      tm=True --database "c2db-first-class-20210125-nodata.db" --key "
      gap_hse" --folder="AB-I" --mode=False >> out.out
33
34 ## AB2:
```

```
python3 c2db.py --query "stoichiometry=AB2, Cl, 0.65<gap_hse<2.12" --tm=True --database "c2db-first-class-20210125-nodata.db" --key "gap_hse" --folder="AB2-Cl" --mode=False >> out.out
python3 c2db.py --query "stoichiometry=AB2, Br, 0.65<gap_hse<2.12" --tm=True --database "c2db-first-class-20210125-nodata.db" --key "gap_hse" --folder="AB2-Br" --mode=False >> out.out
python3 c2db.py --query "stoichiometry=AB2, I, 0.65<gap_hse<2.12" --tm=True --database "c2db-first-class-20210125-nodata.db" --key "gap_hse" --folder="AB2-I" --mode=False >> out.out

## AB3:
python3 c2db.py --query "stoichiometry=AB3, Cl, 0.65<gap_hse<2.12" --tm=True --database "c2db-first-class-20210125-nodata.db" --key "gap_hse" --folder="AB3-Cl" --mode=False >> out.out
python3 c2db.py --query "stoichiometry=AB3, Br, 0.65<gap_hse<2.12" --tm=True --database "c2db-first-class-20210125-nodata.db" --key "gap_hse" --folder="AB3-Br" --mode=False >> out.out
python3 c2db.py --query "stoichiometry=AB3, I, 0.65<gap_hse<2.12" --tm=True --database "c2db-first-class-20210125-nodata.db" --key "gap_hse" --folder="AB3-I" --mode=False >> out.out

mkdir 2-gap_hse
mv AB-Cl AB-Br AB-I AB2-Cl AB2-Br AB2-I AB3-Cl AB3-Br AB3-I 2-gap_hse

############################
## Stability to phonons ##
############################

## AB:
python3 c2db.py --query "stoichiometry=AB, Cl, 0.65<gap_hse<2.12, dynamic_stability_phonons=high" --tm=True --database "c2db-first-class-20210125-nodata.db" --key "dynamic_stability_phonons" --folder="AB-Cl" --mode=False >> out.out
python3 c2db.py --query "stoichiometry=AB, Br, 0.65<gap_hse<2.12, dynamic_stability_phonons=high" --tm=True --database "c2db-first-class-20210125-nodata.db" --key "dynamic_stability_phonons" --folder="AB-Br" --mode=False >> out.out
python3 c2db.py --query "stoichiometry=AB, I, 0.65<gap_hse<2.12, dynamic_stability_phonons=high" --tm=True --database "c2db-first-class-20210125-nodata.db" --key "dynamic_stability_phonons" --folder="AB-I" --mode=False >> out.out

```

```
## AB2:
python3 c2db.py --query "stoichiometry=AB2, Cl, 0.65<gap_hse<2.12,
    dynamic_stability_phonons=high" --tm=True --database "c2db-first
    -class-20210125-nodata.db" --key "dynamic_stability_phonons" --
    folder="AB2-Cl" --mode=False >> out.out
python3 c2db.py --query "stoichiometry=AB2, Br, 0.65<gap_hse<2.12,
    dynamic_stability_phonons=high" --tm=True --database "c2db-first
    -class-20210125-nodata.db" --key "dynamic_stability_phonons" --
    folder="AB2-Br" --mode=False >> out.out
python3 c2db.py --query "stoichiometry=AB2, I, 0.65<gap_hse<2.12,
    dynamic_stability_phonons=high" --tm=True --database "c2db-first
    -class-20210125-nodata.db" --key "dynamic_stability_phonons" --
    folder="AB2-I" --mode=False >> out.out

## AB3:
python3 c2db.py --query "stoichiometry=AB3, Cl, 0.65<gap_hse<2.12,
    dynamic_stability_phonons=high" --tm=True --database "c2db-first
    -class-20210125-nodata.db" --key "dynamic_stability_phonons" --
    folder="AB3-Cl" --mode=False >> out.out
python3 c2db.py --query "stoichiometry=AB3, Br, 0.65<gap_hse<2.12,
    dynamic_stability_phonons=high" --tm=True --database "c2db-first
    -class-20210125-nodata.db" --key "dynamic_stability_phonons" --
    folder="AB3-Br" --mode=False >> out.out
python3 c2db.py --query "stoichiometry=AB3, I, 0.65<gap_hse<2.12,
    dynamic_stability_phonons=high" --tm=True --database "c2db-first
    -class-20210125-nodata.db" --key "dynamic_stability_phonons" --
    folder="AB3-I" --mode=False >> out.out

mkdir 3-phonons
mv AB-Cl AB-Br AB-I AB2-Cl AB2-Br AB2-I AB3-Cl AB3-Br AB3-I 3-
    phonons

###################
## Non magnetic ##
###################

## AB:
python3 c2db.py --query "stoichiometry=AB, Cl, 0.65<gap_hse<2.12,
    dynamic_stability_phonons=high, is_magnetic=False" --tm=True --
    database "c2db-first-class-20210125-nodata.db" --key "
    is_magnetic" --folder="AB-Cl" --mode=False >> out.out
python3 c2db.py --query "stoichiometry=AB, Br, 0.65<gap_hse<2.12,
    dynamic_stability_phonons=high, is_magnetic=False" --tm=True --
```

```
    database "c2db-first-class-20210125-nodata.db" --key "
    is_magnetic" --folder="AB-Br" --mode=False >> out.out
python3 c2db.py --query "stoichiometry=AB, I, 0.65<gap_hse<2.12,
    dynamic_stability_phonons=high, is_magnetic=False" --tm=True --
    database "c2db-first-class-20210125-nodata.db" --key "
    is_magnetic" --folder="AB-I" --mode=False >> out.out

## AB2:
python3 c2db.py --query "stoichiometry=AB2, Cl, 0.65<gap_hse<2.12,
    dynamic_stability_phonons=high, is_magnetic=False" --tm=True --
    database "c2db-first-class-20210125-nodata.db" --key "
    is_magnetic" --folder="AB2-Cl" --mode=False >> out.out
python3 c2db.py --query "stoichiometry=AB2, Br, 0.65<gap_hse<2.12,
    dynamic_stability_phonons=high, is_magnetic=False" --tm=True --
    database "c2db-first-class-20210125-nodata.db" --key "
    is_magnetic" --folder="AB2-Br" --mode=False >> out.out
python3 c2db.py --query "stoichiometry=AB2, I, 0.65<gap_hse<2.12,
    dynamic_stability_phonons=high, is_magnetic=False" --tm=True --
    database "c2db-first-class-20210125-nodata.db" --key "
    is_magnetic" --folder="AB2-I" --mode=False >> out.out

## AB3:
python3 c2db.py --query "stoichiometry=AB3, Cl, 0.65<gap_hse<2.12,
    dynamic_stability_phonons=high, is_magnetic=False" --tm=True --
    database "c2db-first-class-20210125-nodata.db" --key "
    is_magnetic" --folder="AB3-Cl" --mode=False >> out.out
python3 c2db.py --query "stoichiometry=AB3, Br, 0.65<gap_hse<2.12,
    dynamic_stability_phonons=high, is_magnetic=False" --tm=True --
    database "c2db-first-class-20210125-nodata.db" --key "
    is_magnetic" --folder="AB3-Br" --mode=False >> out.out
python3 c2db.py --query "stoichiometry=AB3, I, 0.65<gap_hse<2.12,
    dynamic_stability_phonons=high, is_magnetic=False" --tm=True --
    database "c2db-first-class-20210125-nodata.db" --key "
    is_magnetic" --folder="AB3-I" --mode=False >> out.out

mkdir 4-magnetic
mv AB-Cl AB-Br AB-I AB2-Cl AB2-Br AB2-I AB3-Cl AB3-Br AB3-I 4-
    magnetic
```

Appendix B

Complementary Details of Selected Structures

Table B.1 presents a summary of selected systems in C2DB. Other details are treated alongside with this manuscript.

Table B.1: Summary of selected structures from C2DB. SG stands for space group, and C2DB_{UID} is the C2DB unique identifier. The formulas are presented with the number of atoms of each chemical species in the structure.

Formula	SG	Stoichiometry	C2DB_{UID}
Ti_2Cl_4	$P2_1\|m$	AB_2	Ti2Cl4-66087709613c
$TiCl_2$	$P\bar{6}m2$	AB_2	TiCl2-95688ba68ca1
$TiBr_2$	$P\bar{6}m2$	AB_2	TiBr2-57116f9a9a4e
TiI_2	$P\bar{6}m2$	AB_2	TiI2-088e8488f895
Co_2I_6	$P\bar{3}1m$	AB_3	Co2I6-04fd9e7d4375
Zr_2Cl_4	$P2_1\|m$	AB_2	Zr2Cl4-78bf3c7e79be
$ZrCl_2$	$P\bar{6}m2$	AB_2	ZrCl2-dc09b7c396eb
Zr_2Br_4	$P2_1\|m$	AB_2	Zr2Br4-112846d9ccdd
$ZrBr_2$	$P\bar{6}m2$	AB_2	ZrBr2-7897c7cc2491
Zr_2I_4	$P2_1\|m$	AB_2	Zr2I4-a5233adfb04f
ZrI_2	$P\bar{6}m2$	AB_2	ZrI2-9c024b5a2e89
Mo_2Cl_6	$P\bar{6}2m$	AB_3	Mo2Cl6-61d74efeaeeb
Rh_2I_6	$P\bar{3}1m$	AB_3	Rh2I6-cead7a19c832

Continued on next page

Table B.1 – continued from previous page

Formula	SG	Stoichiometry	$C2DB_{UID}$
Pd_4I_8	$P2_1\|c$	AB_2	Pd4I8-4ad713ff946b
Hf_2Cl_4	$P2_1\|m$	AB_2	Hf2Cl4-ddc64205f942
$HfCl_2$	$P\bar{6}m2$	AB_2	HfCl2-864f8b497185
Hf_2Br_4	$P2_1\|m$	AB_2	Hf2Br4-69aac3df8db3
$HfBr_2$	$P\bar{6}m2$	AB_2	HfBr2-84e9162c0c53
Hf_2I_4	$P2_1\|m$	AB_2	Hf2I4-236ec74b0662
HfI_2	$P\bar{6}m2$	AB_2	HfI2-05a69240794c
W_2Cl_6	$P\bar{3}1m$	AB_3	W2Cl6-de9b6fb4fc55
W_2Cl_6	$P\bar{6}2m$	AB_3	W2Cl6-eea8aee9e120
HgI_2	$P\bar{3}m1$-α	AB_2	Hg2I2-f7e70d2b90ad
Hg_2I_2	$P\bar{3}m1$-β	AB	Hg2I2-f7e70d2b90ad

Appendix C

Computational Parameters and Implementations

This appendix presents the computational parameters and computational implementations used in the present work. Section C.1 show the main parameters and computational convergence of parameters to implement the density functional theory. Then, section C.2 presents some details of the wannierization procedure. And, lastly, in section C.3 discuss the parameters and implementations for optical and excitonic calculations.

C.1 Density Functional Theory Calculations

The electronic and structural calculations of the present work are based on the DFT framework using the Vienna Ab initio Simulation Package[151,114] (VASP) version 5.4.4. with KS equations solved by the PAW method, where the cutoff energy for plane wave expansions is selected by the largest recommended (`ENMAX`) of the chemical species in each structure, presented in table C.1. Furthermore, we adopted an energy criterion of 10^{-6} eV for the self-consistent cycle of KS.

Table C.1: PAW-PBE projectors selected for this work. The minimum and maximum recommended cutoff energy for the plane-wave basis set, `ENMIN` and `ENMAX`, the number of valence electrons, Z_{val}, and the valence electronic configuration.

Element	PAW projector	`ENMIN` (eV)	`ENMAX` (eV)	Z_{val}	Valence
Cl	Cl_GW 19Mar2012	196.854	262.472	7	$3s^2 3p^5$
Br	Br_GW 20Mar2012	162.214	216.285	7	$4s^2 4p^5$
I	I_GW 12Mar2012	131.735	175.647	7	$5s^2 5p^5$
Ti	Ti_sv_GW 05Dec2013	287.830	383.774	12	$3s^2 3p^6 3d^4$
Co	Co_GW 31Mar2010	242.550	323.400	9	$3d^8 4s^1$
Zr	Zr_sv_GW 05Dec2013	259.773	346.364	12	$4s^2 4p^6 4s^4$
Mo	Mo_sv_GW 05Dec2013	258.686	344.914	14	$4s^2 4p^6 4d^6$
Rh	Rh_GW 06Mar2008	185.556	247.408	9	$4d^8 5s^1$
Pd	Pd_GW 06Mar2008	188.194	250.925	10	$4d^9 5s^2$
Hf	Hf_sv_GW 16Jan2015	212.223	282.964	12	$5s^2 5p^6 5d^4$
W	W_sv_GW 23Mar2010	237.849	317.132	14	$5s^2 5p^6 5d^6$
Hg	Hg_sv_GW 16Apr2014	234.021	312.028	20	$5s^2 5p^6 5d^{10} 6s^2$

Stress tensor calculations optimize the strain and forces to generate fully optimized structures using the PBE functional and the conjugate gradient algorithm[94]. The optimized structures are obtained when the forces are lower than 0.01 eV/Å in all atoms. Structural optimizations use a plane wave cutoff energy of `ENCUT` = 2×`ENMAX` to minimize the Pulay stress[152] in volume optimizations, whereas static calculations use a cutoff energy of `ENCUT` = 1.125 × `ENMAX` as the Pulay stress is absent. Those parameters were defined from computational convergence, as detailed in section **??**.

The reciprocal space is sampled using the Monkhorst-Pack scheme[153] with subdivisions in each reciprocal vector determined by equation C.1, where for structural optimizations is used $R_{\mathbf{k}} = 25$Å, while for electronic calculations is used $R_{\mathbf{k}} = 50$Å for better describe the electronic density, with convergence of this parameter presented in appendix **??**. The integration in BZ employs Gaussian smearing of 0.05 eV for structural calculations and 0.01 eV for electronic calculations.

$$N_i = \mathrm{int}(\max(1, R_{\mathbf{k}}|\mathbf{b}_i| + 0.5)) \text{ , } \mathbf{b}_i \text{ is the reciprocal vectors .} \tag{C.1}$$

C.1.1 Computational Convergence

Here, the convergence for cutoff energy and sampling in reciprocal space is presented. We choose Rh_2I_6 with spacegroup $P\bar{3}1m$ to perform those tests. The first test consists of changing the largest value of the cutoff energy ($\texttt{ENMAX}_{\text{MAX}}$) recommended for chemical species in the structure (table C.1) keeping the $R_{\mathbf{k}}$ fixed at 25 Å^{-1} while changing the cutoff energy. Here, the value of $\texttt{ENMAX}_{\text{MAX}}$ is multiplied by a factor range from 0.625 to 3.0 in steps of -0.125. Then the structure is fully optimized with the remaining parameters as in the previous section. The second test consists of changing the $R_{\mathbf{k}}$ by the values 5, 10, 20, 25, 30, 40, 50 and 60 Å^{-1}. with a fixed cutoff energy of $1.5 \times \texttt{ENMAX}_{\text{MAX}}$, fully optimizing the structure. All tests kept the number of $\mathbf{k}-$points at 1 in the vacuum direction of the monolayer.

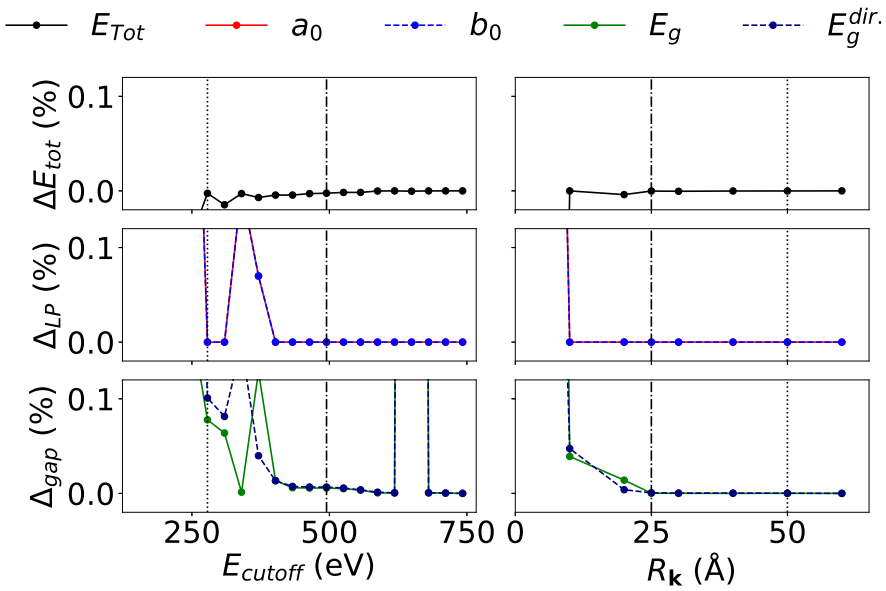

Figure C.1: Convergence tests for cutoff energy and mesh in reciprocal space. The vertical dotted-dashed line depicts the values used for volume optimization calculations while the vertical dashed line depicts the value for static calculation.

Table C.1 depicts the results obtained. First, we should note that for the cutoff energy greater than $1.125 \times \texttt{ENMAX}_{\text{MAX}}$ almost all properties analyzed have a perceptual deviation less than 0.1 %. The values also do not deviate from $R_{\mathbf{k}} = 25\text{Å}^{-1}$.

C.2 Wannierization

The Wannier parameterization is performed using the Wannier90 software[120] version 3 based on the electronic structure calculated with VASP with SOC. It is important to turn on the spinons in the Wannier90 input to ensure a single-state occupation of the Wannier functions. The number of Wannier functions is determined according to the number of orbitals selected and the number of species, according to table C.2. We selected at least 10 bands more than the number of Wannier functions and at least the number twice the number of electrons from the DFT calculation to activate the disentanglement routine. The interface of Wannier90 with VASP uses version 2 of Wannier90[119] to generate the projections of the Bloch functions on the relevant projectors and the overlap matrices and complete information on the Wannier90 input, such as the structure and the mesh of **k** points, which is generated using $R_{\mathbf{k}} = 25$ Å$^{-}1$. The inner window for the disentanglement procedure is chosen to be 4 eV below and above the Fermi level. In addition, the minimization procedure for the spread of Wannier functions is performed 1000 times.

Orbital	N
s	2
p	6
d	10
f	14

Table C.2: Number of Wannier functions according to the orbital.

C.3 Optical and Excitonic Calculations

From the parameterized Hamiltonian with Wannier90, the Wannier-based tight-binding code for electronic band structure (WanTiBEXOS) software[51] calculates the optical and excitonic properties. Other studies have successfully applied the same methodology to investigate various 2D materials[41,154] and low-dimensional perovskites[155,156].

The optical properties in both independent electron approximations (IPA) and the Bethe-Salpeter equation (BSE) were calculated from the dielectric tensor at the direct band-gap point. Additionally, the full band-spectrum of some materials were also presented. Here, the mesh of **k**-points of 120 Å^{-1} is used for calculating the

dielectic tensor, while a tolerance factor of $0.001\,\text{Å}^{-1}$ is used to avoid singularities of coulomb matrix. This work uses a two-dimensional truncated Coulomb matrix, as proposed by Rozzi *et al.*[157] which is presented in equation C.2.

$$W(\mathbf{Q}) = -\frac{e^2}{2\Omega_{UC}\epsilon_0\mathbf{Q}^2}[1 - e^{C_2}(C_1 sin(C_3) - cos(C_3))] \ , \tag{C.2}$$

where, Ω_{UC} is the volume of unit cell, and, $C_{1,2,3}$ are defined as:

$$C_1 = \frac{|Q_z|}{\sqrt{Q_x^2 + Q_y^2}} \ , C_2 = \frac{\mathbf{c_0}}{2}\sqrt{Q_x^2 + Q_y^2} \ C_3 = \frac{c_0}{2}|Q_z| \ , \tag{C.3}$$

with c_0 being the size of lattice vector perpendicular to monolayer, and $Q_{x,y,z}$ the cartesian components of center-or-mass of the excitons pair. Finally, the number of conduction and valence states vary according to the system, and will be defined in the proper section.

Appendix D

Additional Structural Parameters

Table D.1 presents the main lattice parameters calculated here, which are consistent with those presented in C2DB. Other lattice parameters and atomic coordinates do not exhibit significant changes compared to those found in C2 DB, since the space group remains unchanged. Our calculations constrain the lattice parameter perpendicular to the monolayer to be identical to the initial structure collected from C2DB.

Table D.1: Comparison of our calculated lattice parameters with C2DB. In parentheses are shown the deviation in % using equation D.1. a_0 and, b_0 are the lattice parameter and, γ_0 is the angle between a_0 and, b_0.

System	Source	a_0 (Å)	b_0 (Å)	γ_0 (°)
Ti_2Cl_4 ($P2_1\|m$)	This work	3.25	5.91	90.00
	C2DB	3.25 (0.1)	5.91 (0.1)	90.00 (0.0)
$TiCl_2$ ($P\bar{6}m2$)	This work	3.28	3.28	120.00
	C2DB	3.28 (0.1)	3.28 (0.1)	120.00 (0.0)
$TiBr_2$ ($P\bar{6}m2$)	This work	3.47	3.47	120.00
	C2DB	3.47 (0.2)	3.47 (0.2)	120.00 (0.0)
TiI_2 ($P\bar{6}m2$)	This work	3.76	3.76	120.00
	C2DB	3.77 (0.3)	3.77 (0.3)	120.00 (0.0)
Co_2I_6 ($P\bar{3}1m$)	This work	6.72	6.72	120.00

Continued on next page

Table D.1 – continued from previous page

System	Source	a_0 (Å)	b_0 (Å)	γ_0 (°)
	C2DB	6.74 (0.3)	6.74 (0.3)	120.00 (0.0)
Zr_2Cl_4 ($P2_1\|m$)	This work	3.33	6.24	90.00
	C2DB	3.33 (0.0)	6.23 (0.1)	90.00 (0.0)
$ZrCl_2$ ($P\bar{6}m2$)	This work	3.41	3.41	120.00
	C2DB	3.41 (0.1)	3.41 (0.1)	120.00 (0.0)
Zr_2Br_4 ($P2_1\|m$)	This work	3.49	6.50	90.00
	C2DB	3.49 (0.1)	6.50 (0.0)	90.00 (0.0)
$ZrBr_2$ ($P\bar{6}m2$)	This work	3.56	3.56	120.00
	C2DB	3.56 (0.0)	3.56 (0.0)	120.00 (0.0)
Zr_2I_4 ($P2_1\|m$)	This work	3.76	6.91	90.00
	C2DB	3.77 (0.3)	6.91 (0.0)	90.00 (0.0)
ZrI_2 ($P\bar{6}m2$)	This work	3.82	3.82	120.00
	C2DB	3.83 (0.2)	3.83 (0.2)	120.00 (0.0)
Mo_2Cl_6 ($P\bar{6}2m$)	This work	5.59	5.59	120.00
	C2DB	5.59 (0.0)	5.59 (0.0)	120.00 (0.0)
Rh_2I_6 ($P\bar{3}1m$)	This work	6.90	6.90	120.00
	C2DB	6.93 (0.4)	6.93 (0.4)	120.00 (0.0)
Pd_4I_8 ($P2_1\|c$)	This work	7.13	9.03	90.00
	C2DB	7.17 (0.5)	9.10 (0.8)	90.00 (0.0)
Hf_2Cl_4 ($P2_1\|m$)	This work	3.27	6.16	90.00
	C2DB	3.28 (0.2)	6.16 (0.1)	90.00 (0.0)
$HfCl_2$ ($P\bar{6}m2$)	This work	3.35	3.35	120.00
	C2DB	3.35 (0.1)	3.35 (0.1)	120.00 (0.0)
Hf_2Br_4 ($P2_1\|m$)	This work	3.43	6.42	90.00
	C2DB	3.44 (0.2)	6.43 (0.2)	90.00 (0.0)
$HfBr_2$ ($P\bar{6}m2$)	This work	3.49	3.49	120.00
	C2DB	3.50 (0.2)	3.50 (0.2)	120.00 (0.0)

Continued on next page

Table D.1 – continued from previous page

System	Source	a_0 (Å)	b_0 (Å)	γ_0 (°)
Hf_2I_4 ($P2_1\|m$)	This work	3.70	6.81	90.00
	C2DB	3.72 (0.3)	6.83 (0.2)	90.00 (0.0)
HfI_2 ($P\overline{6}m2$)	This work	3.76	3.76	120.00
	C2DB	3.77 (0.3)	3.77 (0.3)	120.00 (0.0)
W_2Cl_6 ($P\overline{3}1m$)	This work	5.56	5.56	120.00
	C2DB	5.56 (0.0)	5.56 (0.0)	120.00 (0.0)
W_2Cl_6 ($P\overline{6}2m$)	This work	5.52	5.52	120.00
	C2DB	5.52 (0.0)	5.52 (0.0)	120.00 (0.0)
HgI_2 ($P\overline{3}m1$-α)	This work	4.37	4.37	120.00
	C2DB	4.39 (0.3)	4.39 (0.3)	120.00 (0.0)
Hg_2I_2 ($P\overline{3}m1$-β)	This work	4.46	4.47	119.94
	C2DB	4.46 (0.1)	4.48 (0.3)	119.80 (0.1)

$$\Delta_X = \left(\frac{|X_{\text{C2DB}} - X_{\text{This work}}|}{X_{\text{This Work}}} \right) 100\% \tag{D.1}$$

Appendix E

Complementary details of Electronic Properties

E.1 Density of States

This section provides additional details on density of states (DOS) calculations. Figures E.1 and E.2 show the total DOS (TDOS), the total local DOS (TLDOS), which includes the local DOS (LDOS) for the halides (B) and transition metal (A) atoms, calculated using the PBE XC functional and including spin-orbit coupling (SOC). Figures E.3 and E.4 depict the local DOS projected on atoms and orbitals for TDOS and TLDOS, respectively, in both PBE and PBE+SOC calculations.

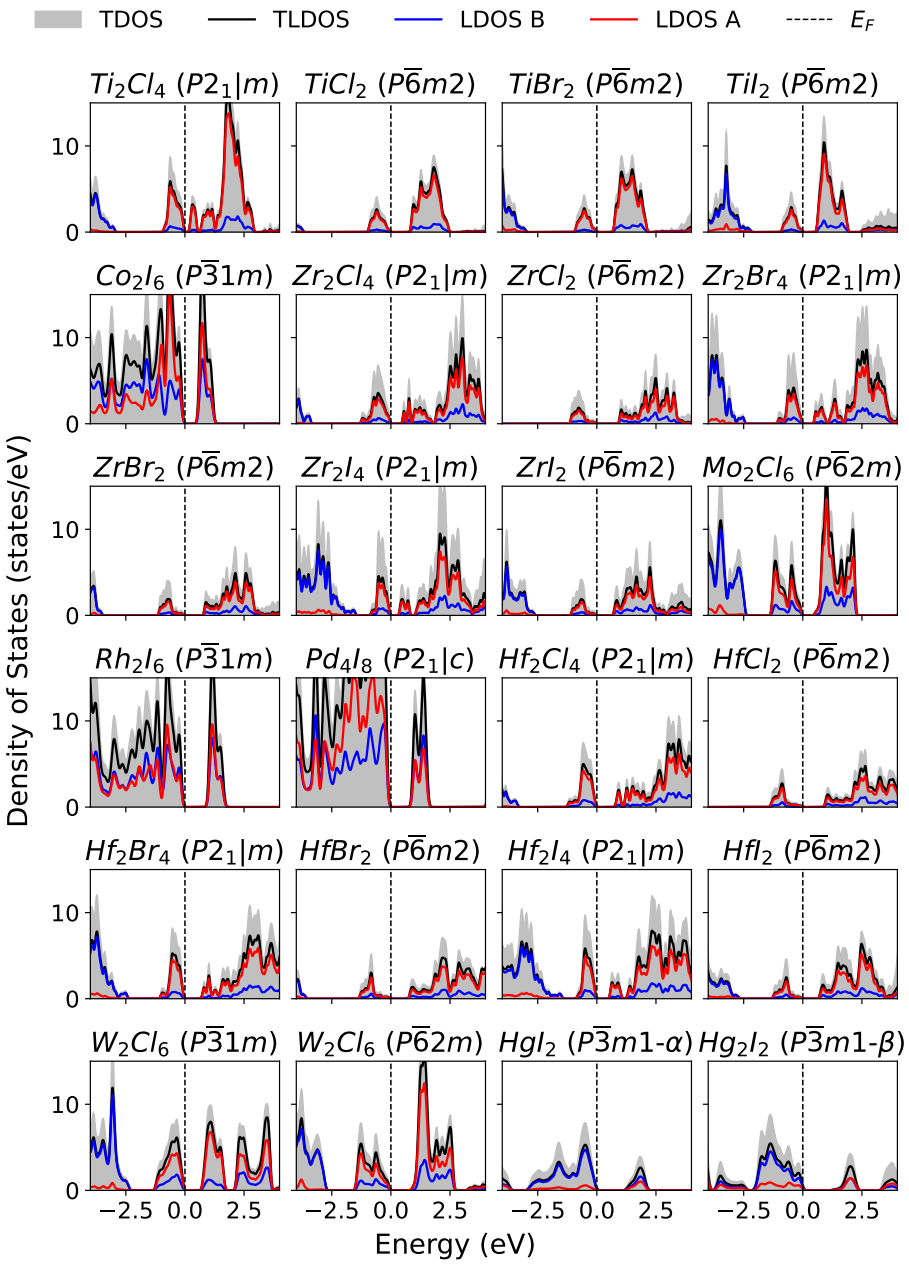

Figure E.1: TDOS (grey fill curve), TLDOS (black line), LDOS on halide atoms B (blue line) and in transition metal atoms A (red line) calculated using the PBE functional.

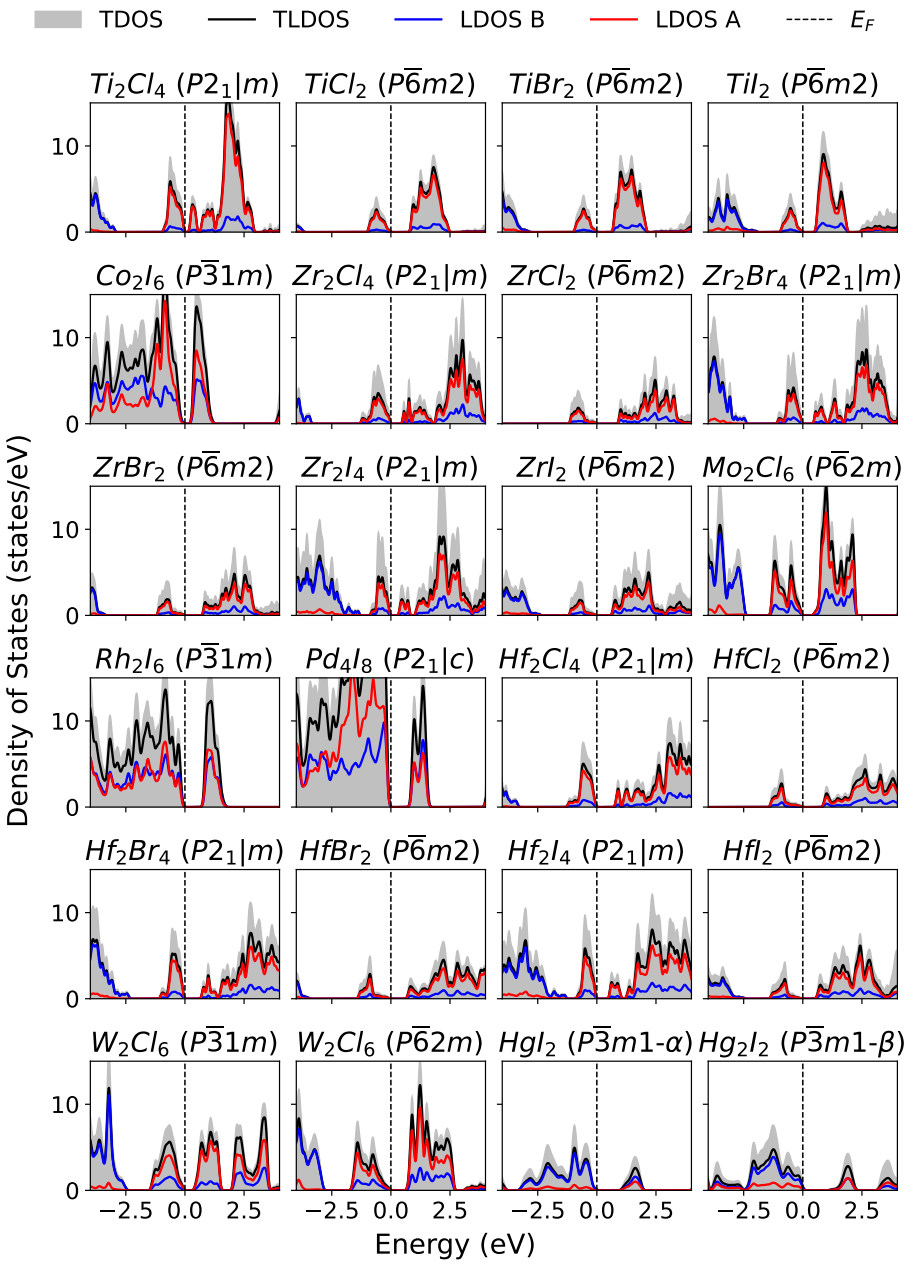

Figure E.2: TDOS (grey fill curve), TLDOS (black line), LDOS on halide atoms B (blue line) and in transition metal atoms A (red line) calculated using the PBE functional including SOC.

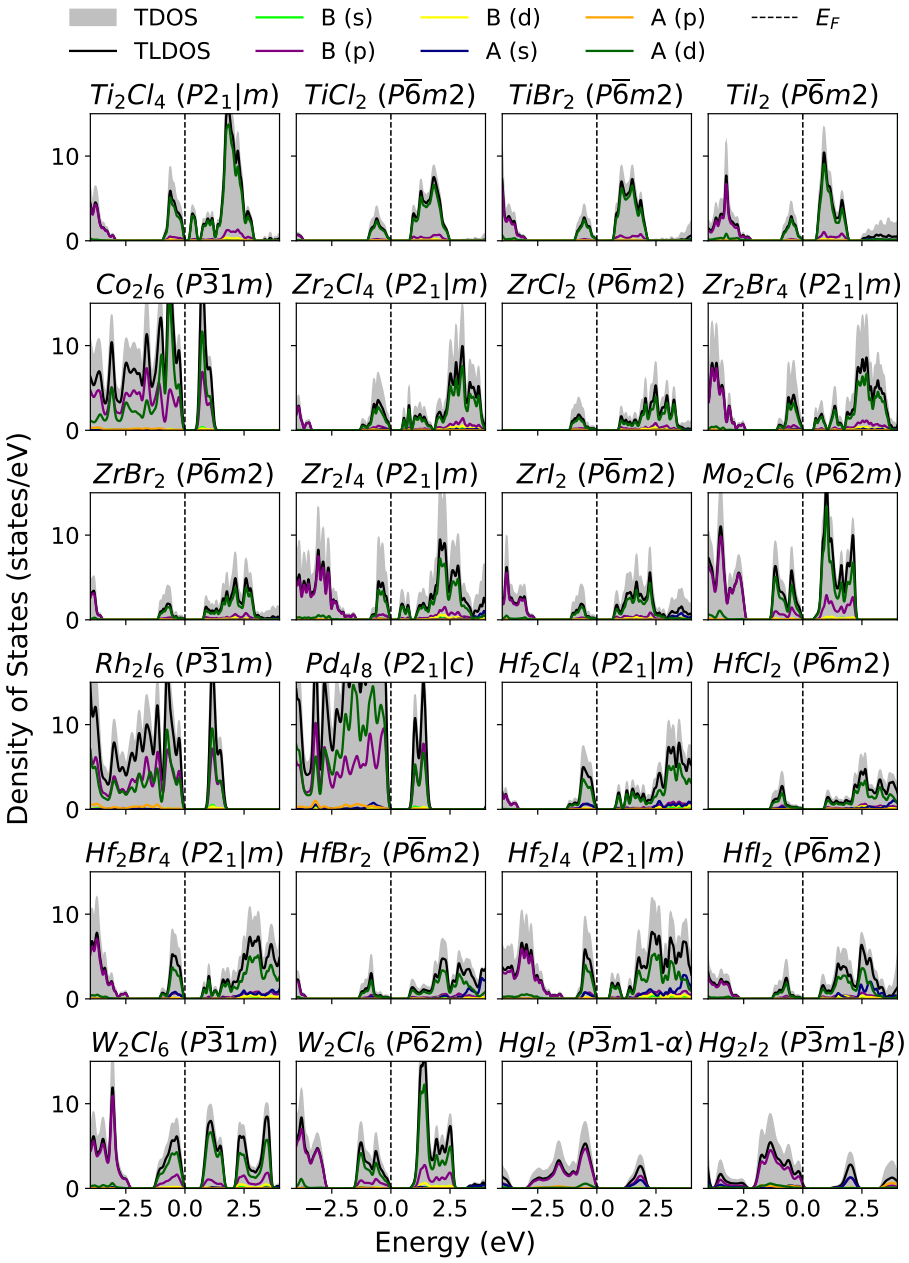

Figure E.3: TDOS (grey fill curve), TLDOS (black line), Halide (B) orbital s, p, d states (lime, purple and yellow, respectively) and in transition metal A orbital s, p, d states (dark-blue, orange and dark green, respectively) calculated using the PBE functional.

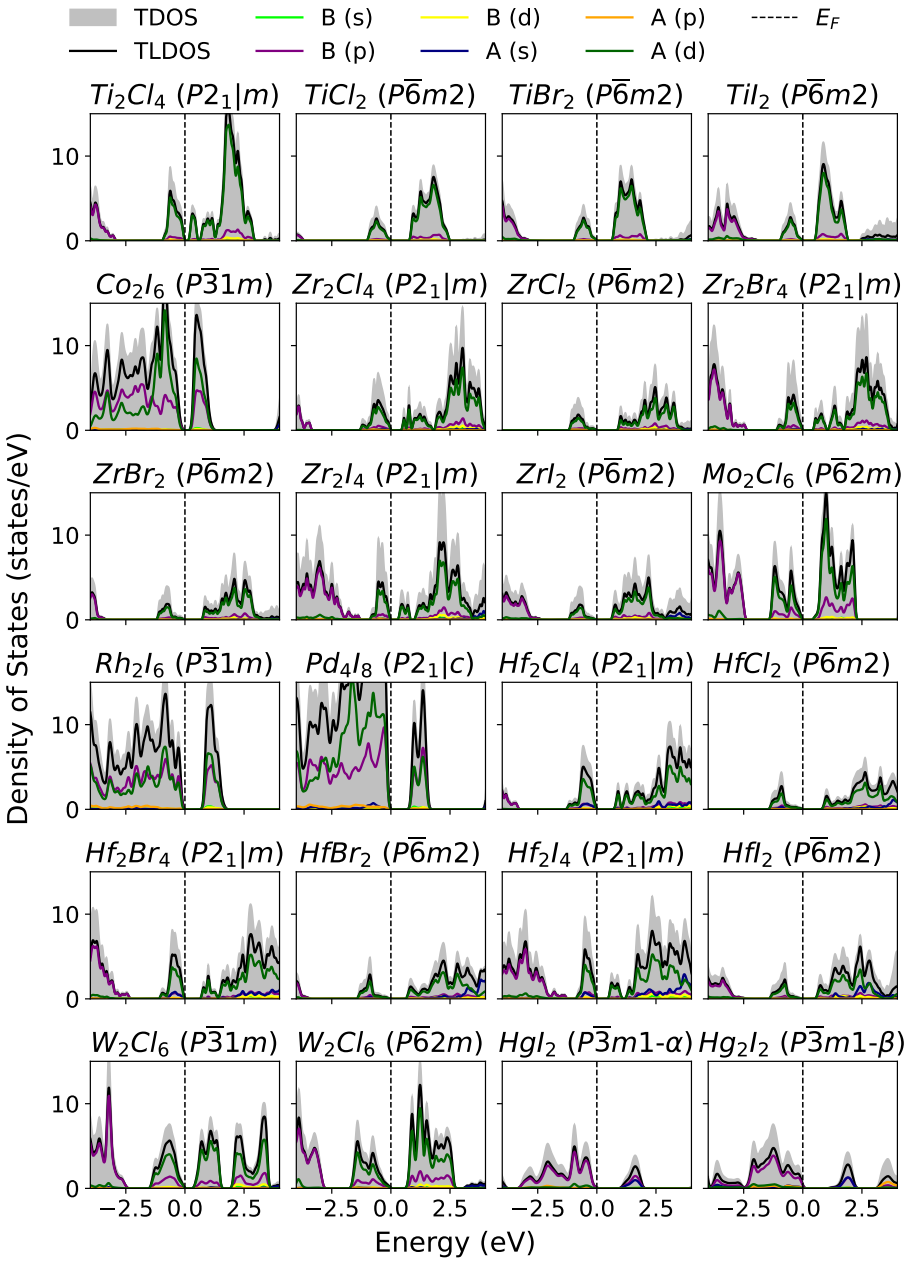

Figure E.4: TDOS (grey fill curve), TLDOS (black line), Halide (B) orbital s, p, d states (lime, purple and yellow, respectively) and in transition metal A orbital s, p, d states (dark-blue, orange and dark green, respectively) calculated using the PBE functional inclusing SOC.

E.2 Electronic Band Strutures

This section provides additional details on electronic band structures. Figure E.5 shows the PBE band structure, including spin-orbit coupling (PBE+SOC). Figure E.6 depicts the HSE06 functional-based band structure. Tables E.1, E.2, and E.3 present the details of band gaps, including comparisons with C2DB for PBE and PBE+SOC, respectively. In tables E.1, E.2, and E.3, the type of fundamental band gap, which was either indirect (direct), is calculated considering a threshold value of 0.01 eV in the difference between the direct and fundamental gaps.

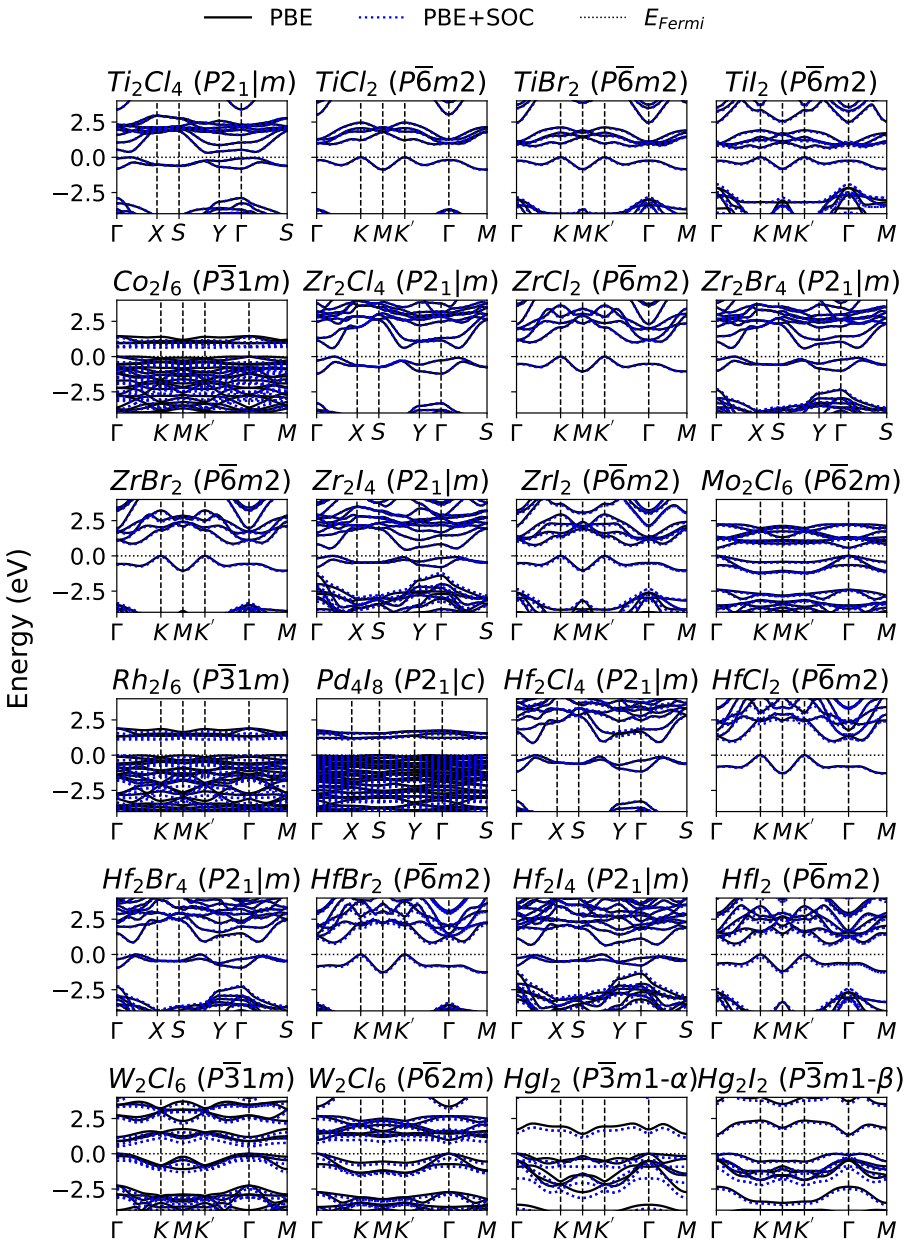

Figure E.5: The band structure with the PBE functional (solid black line) and including spin-orbit coupling (PBE+SOC) (blue solid line) is depicted. The Fermi level (E_{Fermi}) is shifted to zero, as shown by the black dotted line. Vertical black dashed lines indicate special points in the Brillouin zone.

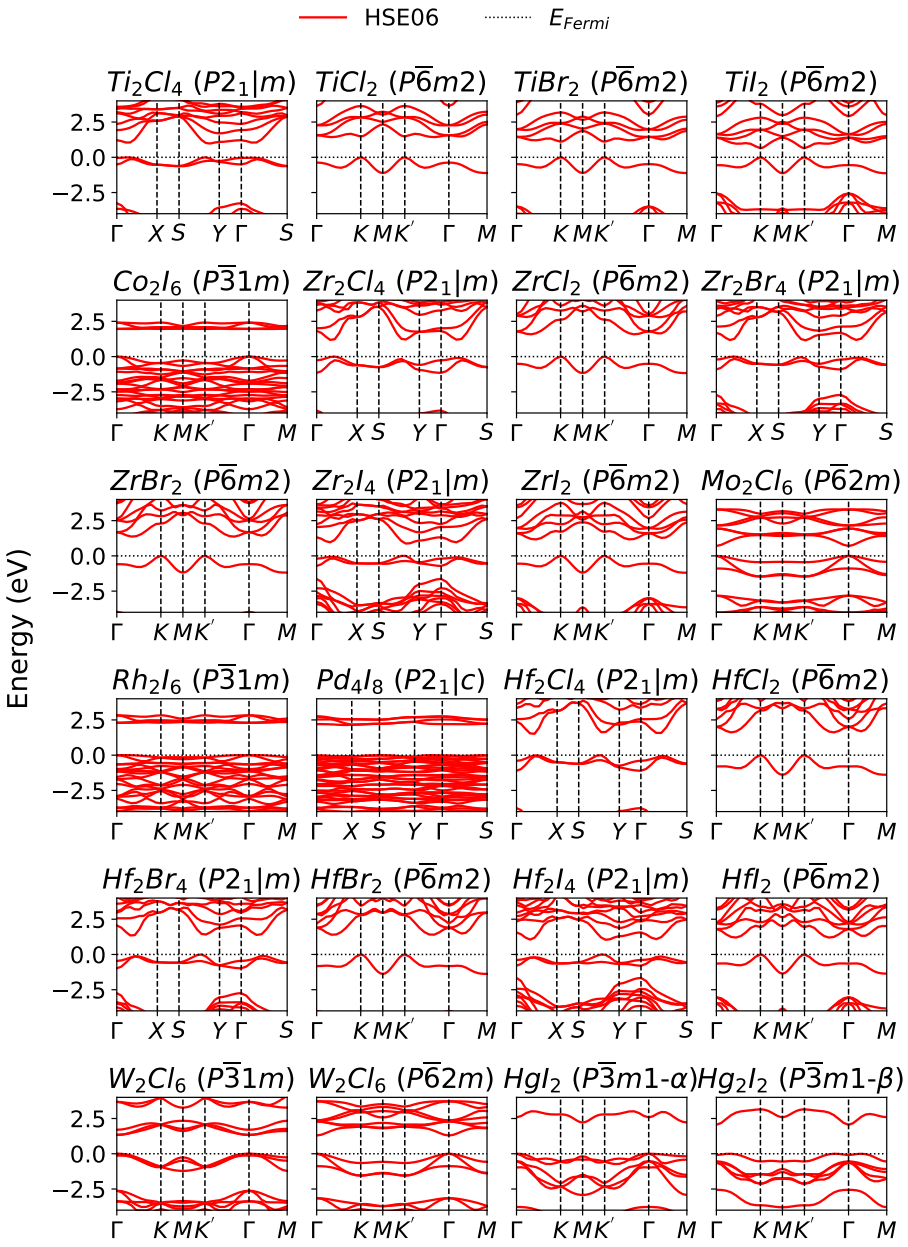

Figure E.6: The band structure with the HSE06 functional is depicted. The Fermi level (E_{Fermi}) is shifted to zero, as shown by the black dotted line. Vertical black dashed lines indicate special points in the Brillouin zone.

Table E.1: The fundamental band gap (E_g), which is defined by the difference between the valence band maximum (VBM) and conduction band minimum (CBM), was calculated in this work using the PBE functional, where type refer if the fundamental bandgap is direct or indirect. The direct band gap (E_g^{dir}) was also determined. These values were compared with those presented in C2DB, and the percentage deviation is shown in parentheses, as calculated according to equation D.1.

System	Source	E_g (eV)	Type	$E_g^{\text{dir.}}$ (eV)
Ti_2Cl_4 ($P2_1\|m$)	This work	0.32	Indirect	0.38
	C2DB	0.32 (1.0)	Indirect	0.39 (1.7)
$TiCl_2$ ($P\bar{6}m2$)	This work	0.93	Indirect	1.19
	C2DB	0.92 (0.6)	Indirect	1.18 (0.5)
$TiBr_2$ ($P\bar{6}m2$)	This work	0.80	Indirect	0.98
	C2DB	0.79 (0.5)	Indirect	0.97 (1.2)
TiI_2 ($P\bar{6}m2$)	This work	0.68	Direct	0.69
	C2DB	0.67 (1.3)	Direct	0.67 (2.0)
Co_2I_6 ($P\bar{3}1m$)	This work	0.95	Direct	0.96
	C2DB	0.87 (8.8)	Indirect	0.88 (8.0)
Zr_2Cl_4 ($P2_1\|m$)	This work	0.59	Direct	0.60
	C2DB	0.61 (3.1)	Direct	0.61 (2.3)
$ZrCl_2$ ($P\bar{6}m2$)	This work	1.01	Indirect	1.58
	C2DB	1.01 (0.6)	Indirect	1.59 (0.5)
Zr_2Br_4 ($P2_1\|m$)	This work	0.59	Indirect	0.62
	C2DB	0.58 (0.8)	Indirect	0.64 (2.7)
$ZrBr_2$ ($P\bar{6}m2$)	This work	0.86	Indirect	1.48
	C2DB	0.87 (0.6)	Indirect	1.48 (0.0)
Zr_2I_4 ($P2_1\|m$)	This work	0.43	Indirect	0.54
	C2DB	0.43 (1.0)	Indirect	0.53 (1.0)
ZrI_2 ($P\bar{6}m2$)	This work	0.77	Indirect	1.36
	C2DB	0.77 (0.0)	Indirect	1.36 (0.3)
Mo_2Cl_6 ($P\bar{6}2m$)	This work	0.58	Direct	0.58

Continued on next page

Table E.1 – continued from previous page

System	Source	E_g (eV)	Type	$E_g^{\text{dir.}}$ (eV)
	C2DB	0.56 (2.6)	Direct	0.56 (2.6)
Rh_2I_6 ($P\bar{3}1m$)	This work	1.34	Indirect	1.37
	C2DB	1.25 (6.7)	Indirect	1.29 (6.1)
Pd_4I_8 ($P2_1\|c$)	This work	1.19	Indirect	1.24
	C2DB	1.14 (4.1)	Indirect	1.18 (4.4)
Hf_2Cl_4 ($P2_1\|m$)	This work	0.88	Indirect	0.90
	C2DB	0.87 (0.5)	Indirect	0.89 (1.2)
$HfCl_2$ ($P\bar{6}m2$)	This work	1.00	Indirect	1.80
	C2DB	1.01 (1.1)	Indirect	1.79 (0.5)
Hf_2Br_4 ($P2_1\|m$)	This work	0.86	Indirect	0.90
	C2DB	0.88 (2.9)	Indirect	0.90 (0.5)
$HfBr_2$ ($P\bar{6}m2$)	This work	0.84	Indirect	1.62
	C2DB	0.85 (0.8)	Indirect	1.62 (0.0)
Hf_2I_4 ($P2_1\|m$)	This work	0.65	Indirect	0.70
	C2DB	0.66 (1.3)	Indirect	0.71 (1.5)
HfI_2 ($P\bar{6}m2$)	This work	0.77	Indirect	1.43
	C2DB	0.78 (1.1)	Indirect	1.41 (1.0)
W_2Cl_6 ($P\bar{3}1m$)	This work	0.90	Direct	0.90
	C2DB	0.90 (0.2)	Direct	0.90 (0.2)
W_2Cl_6 ($P\bar{6}2m$)	This work	0.98	Direct	0.98
	C2DB	0.97 (0.9)	Direct	0.97 (0.9)
HgI_2 ($P\bar{3}m1$-α)	This work	1.41	Indirect	1.58
	C2DB	1.51 (7.2)	Indirect	1.67 (6.0)
Hg_2I_2 ($P\bar{3}m1$-β)	This work	1.36	Indirect	1.46
	C2DB	1.43 (5.0)	Indirect	1.52 (4.7)

Table E.2: The fundamental band gap (E_g), which is defined by the difference between the valence band maximum (VBM) and conduction band minimum (CBM), was calculated in this work using the PBE+SOC functional, where type refer if the fundamental bandgap is direct or indirect. The direct band gap (E_g^{dir}) was also determined. These values were compared with those presented in C2DB, and the percentage deviation is shown in parentheses, as calculated according to equation D.1.

System	Source	E_g (eV)	Type	$E_g^{\text{dir.}}$ (eV)
Ti_2Cl_4 ($P2_1\|m$)	This work	0.32	Indirect	0.38
	C2DB	0.32 (0.9)	Indirect	0.39 (1.6)
$TiCl_2$ ($P\bar{6}m2$)	This work	0.91	Indirect	1.19
	C2DB	0.90 (0.6)	Indirect	1.18 (0.5)
$TiBr_2$ ($P\bar{6}m2$)	This work	0.76	Indirect	0.94
	C2DB	0.76 (0.4)	Indirect	0.93 (1.3)
TiI_2 ($P\bar{6}m2$)	This work	0.61	Indirect	0.64
	C2DB	0.60 (2.3)	Indirect	0.62 (3.2)
Co_2I_6 ($P\bar{3}1m$)	This work	0.64	Indirect	0.67
	C2DB	0.53 (17.4)	Indirect	0.58 (13.8)
Zr_2Cl_4 ($P2_1\|m$)	This work	0.59	Direct	0.60
	C2DB	0.61 (3.0)	Direct	0.61 (2.1)
$ZrCl_2$ ($P\bar{6}m2$)	This work	0.97	Indirect	1.57
	C2DB	0.98 (0.7)	Indirect	1.58 (0.6)
Zr_2Br_4 ($P2_1\|m$)	This work	0.59	Indirect	0.62
	C2DB	0.58 (1.0)	Indirect	0.64 (2.7)
$ZrBr_2$ ($P\bar{6}m2$)	This work	0.82	Indirect	1.48
	C2DB	0.83 (0.7)	Indirect	1.48 (0.0)
Zr_2I_4 ($P2_1\|m$)	This work	0.42	Indirect	0.54
	C2DB	0.42 (0.1)	Indirect	0.53 (1.0)
ZrI_2 ($P\bar{6}m2$)	This work	0.70	Indirect	1.30
	C2DB	0.69 (1.3)	Indirect	1.27 (2.0)
Mo_2Cl_6 ($P\bar{6}2m$)	This work	0.53	Direct	0.53

Continued on next page

Table E.2 – continued from previous page

System	Source	E_g (eV)	Type	$E_g^{\text{dir.}}$ (eV)
	C2DB	0.51 (3.3)	Direct	0.51 (3.3)
Rh_2I_6 ($P\bar{3}1m$)	This work	1.11	Indirect	1.12
	C2DB	0.99 (10.8)	Indirect	1.02 (9.5)
Pd_4I_8 ($P2_1\|c$)	This work	1.13	Indirect	1.18
	C2DB	1.07 (5.1)	Indirect	1.10 (6.1)
Hf_2Cl_4 ($P2_1\|m$)	This work	0.86	Indirect	0.88
	C2DB	0.84 (2.3)	Indirect	0.86 (2.9)
$HfCl_2$ ($P\bar{6}m2$)	This work	0.91	Indirect	1.74
	C2DB	0.91 (0.3)	Indirect	1.72 (0.8)
Hf_2Br_4 ($P2_1\|m$)	This work	0.84	Indirect	0.88
	C2DB	0.85 (1.2)	Indirect	0.87 (1.0)
$HfBr_2$ ($P\bar{6}m2$)	This work	0.74	Indirect	1.56
	C2DB	0.73 (1.3)	Indirect	1.55 (0.5)
Hf_2I_4 ($P2_1\|m$)	This work	0.63	Indirect	0.67
	C2DB	0.63 (0.2)	Indirect	0.67 (0.1)
HfI_2 ($P\bar{6}m2$)	This work	0.63	Indirect	1.32
	C2DB	0.63 (0.1)	Indirect	1.28 (3.1)
W_2Cl_6 ($P\bar{3}1m$)	This work	0.52	Direct	0.52
	C2DB	0.49 (6.1)	Direct	0.49 (6.1)
W_2Cl_6 ($P\bar{6}2m$)	This work	0.75	Direct	0.75
	C2DB	0.71 (5.8)	Direct	0.71 (5.8)
HgI_2 ($P\bar{3}m1$-α)	This work	1.15	Indirect	1.42
	C2DB	1.20 (4.5)	Indirect	1.47 (3.2)
Hg_2I_2 ($P\bar{3}m1$-β)	This work	1.26	Indirect	1.28
	C2DB	1.28 (1.4)	Indirect	1.30 (1.3)

Table E.3: The fundamental band gap (E_g), which is defined by the difference between the valence band maximum (VBM) and conduction band minimum (CBM), was calculated in this work using the HSE06 functional, where type refer if the fundamental bandgap is direct or indirect. The direct band gap (E_g^{dir}) was also determined.

System	E_g (eV)	Type	$E_g^{\text{dir.}}$ (eV)
Ti_2Cl_4 ($P2_1\|m$)	0.98	Indirect	1.01
$TiCl_2$ ($P\bar{6}m2$)	1.43	Indirect	1.48
$TiBr_2$ ($P\bar{6}m2$)	1.11	Direct	1.11
TiI_2 ($P\bar{6}m2$)	0.64	Direct	0.64
Co_2I_6 ($P\bar{3}1m$)	1.96	Direct	1.96
Zr_2Cl_4 ($P2_1\|m$)	1.19	Indirect	1.21
$ZrCl_2$ ($P\bar{6}m2$)	1.58	Indirect	2.19
Zr_2Br_4 ($P2_1\|m$)	1.15	Indirect	1.20
$ZrBr_2$ ($P\bar{6}m2$)	1.37	Indirect	2.06
Zr_2I_4 ($P2_1\|m$)	0.87	Direct	0.87
ZrI_2 ($P\bar{6}m2$)	1.17	Indirect	1.71
Mo_2Cl_6 ($P\bar{6}2m$)	0.70	Direct	0.70
Rh_2I_6 ($P\bar{3}1m$)	2.30	Direct	2.30
Pd_4I_8 ($P2_1\|c$)	2.14	Indirect	2.21
Hf_2Cl_4 ($P2_1\|m$)	1.52	Indirect	1.54
$HfCl_2$ ($P\bar{6}m2$)	1.62	Indirect	2.46
Hf_2Br_4 ($P2_1\|m$)	1.35	Indirect	1.46
$HfBr_2$ ($P\bar{6}m2$)	1.40	Indirect	2.22
Hf_2I_4 ($P2_1\|m$)	1.04	Indirect	1.07
HfI_2 ($P\bar{6}m2$)	1.20	Indirect	1.93
W_2Cl_6 ($P\bar{3}1m$)	1.34	Direct	1.34
W_2Cl_6 ($P\bar{6}2m$)	1.29	Direct	1.29
HgI_2 ($P\bar{3}m1$-α)	2.22	Indirect	2.40
Hg_2I_2 ($P\bar{3}m1$-β)	2.06	Indirect	2.15

E.3 Band Gap Corrections

The scissors operator in this work correct the bandgap by using the equation E.1. It was chosen because of its ability to provide a more realistic single-particle band gap while maintaining an affordable computational cost. Table E.4 presents the correct band gaps as the scissors operator (χ) for the fundamental and direct band gap.

$$E_g^{\text{HSE06+SOC}} = E_g^{PBE+SOC} + (\overbrace{E_g^{HSE06} - E_g^{PBE}}^{\chi}) \ . \tag{E.1}$$

Table E.4: The scissors operator ($\chi_{\text{dir.}}$) and the corrected band gaps ($E_g^{\text{HSE06+SOC, dir.}}$) were calculated using equation E.1, considering the direct band gap. The corrected band gap values are also compared with those presented in C2DB.

System	Source	$\chi_{\text{dir.}}$ (eV)	$E_g^{\text{HSE06+SOC, dir.}}$ (eV)	
Ti_2Cl_4 ($P2_1\|m$)	This work	0.63	1.01	
	C2DB	-	1.01	(0.0)
$TiCl_2$ ($P\bar{6}m2$)	This work	0.29	1.48	
	C2DB	-	1.65	(11.3)
$TiBr_2$ ($P\bar{6}m2$)	This work	0.13	1.07	
	C2DB	-	1.28	(19.9)
TiI_2 ($P\bar{6}m2$)	This work	−0.04	0.59	
	C2DB	-	0.83	(39.6)
Co_2I_6 ($P\bar{3}1m$)	This work	1.01	1.68	
	C2DB	-	1.98	(18.1)
Zr_2Cl_4 ($P2_1\|m$)	This work	0.62	1.21	
	C2DB	-	1.15	(5.4)
$ZrCl_2$ ($P\bar{6}m2$)	This work	0.61	2.18	
	C2DB	-	2.16	(1.0)
Zr_2Br_4 ($P2_1\|m$)	This work	0.57	1.19	
	C2DB	-	1.17	(1.8)

Continued on next page

Table E.4 – continued from previous page

System	Source	$\chi_{\text{dir.}}$ (eV)	$E_g^{\text{HSE06+SOC, dir.}}$ (eV)	
$ZrBr_2$ ($P\bar{6}m2$)	This work	0.58	2.05	
	C2DB	-	2.00	(2.9)
Zr_2I_4 ($P2_1\|m$)	This work	0.33	0.87	
	C2DB	-	0.89	(2.2)
ZrI_2 ($P\bar{6}m2$)	This work	0.34	1.64	
	C2DB	-	1.68	(2.4)
Mo_2Cl_6 ($P\bar{6}2m$)	This work	0.13	0.65	
	C2DB	-	0.82	(24.8)
Rh_2I_6 ($P\bar{3}1m$)	This work	0.92	2.05	
	C2DB	-	2.02	(1.2)
Pd_4I_8 ($P2_1\|c$)	This work	0.97	2.15	
	C2DB	-	2.06	(4.0)
Hf_2Cl_4 ($P2_1\|m$)	This work	0.64	1.52	
	C2DB	-	1.46	(4.4)
$HfCl_2$ ($P\bar{6}m2$)	This work	0.66	2.39	
	C2DB	-	2.34	(2.2)
Hf_2Br_4 ($P2_1\|m$)	This work	0.56	1.44	
	C2DB	-	1.42	(1.6)
$HfBr_2$ ($P\bar{6}m2$)	This work	0.60	2.15	
	C2DB	-	2.10	(2.4)
Hf_2I_4 ($P2_1\|m$)	This work	0.37	1.04	
	C2DB	-	1.05	(1.0)
HfI_2 ($P\bar{6}m2$)	This work	0.50	1.82	
	C2DB	-	1.77	(2.9)
W_2Cl_6 ($P\bar{3}1m$)	This work	0.44	0.96	
	C2DB	-	0.88	(7.7)
W_2Cl_6 ($P\bar{6}2m$)	This work	0.31	1.06	

Continued on next page

Table E.4 – continued from previous page

System	Source	$\chi_{\text{dir.}}$ (eV)	$E_g^{\text{HSE06+SOC, dir.}}$ (eV)	
	C2DB	-	1.16	(9.6)
HgI_2 ($P\bar{3}m1$-α)	This work	0.82	2.24	
	C2DB	-	2.22	(0.9)
Hg_2I_2 ($P\bar{3}m1$-β)	This work	0.69	1.98	
	C2DB	-	1.95	(1.6)

E.4 Work Function

The work function, defined as the energy necessary to remove an electron from the Fermi level and bring it to infinity, is presented in table E.5. The calculation of the work function was performed using equation E.2 for the PBE and PBE+SOC functionals.

$$\Phi = V(\mathbf{r}_{vac}) - E_{Fermi} \ , \tag{E.2}$$

where, $V(\mathbf{r}_{vac})$ is the vacuum potential, i.e. far away from the structure and E_{Fermi} the Fermi level.

Table E.5: Summary of data and calculated value of workfunction for PBE and PBE+SOC functionals.

System	Functional	$V(\mathbf{r}_{vac.})$ (eV)	E_{Fermi} (eV)	Φ (eV)
Ti_2Cl_4 ($P2_1\|m$)	PBE	3.43	−1.22	4.65
	PBE+SOC	3.43	−1.22	4.65
$TiCl_2$ ($P\bar{6}m2$)	PBE	3.51	−0.75	4.26
	PBE+SOC	3.51	−0.73	4.24
$TiBr_2$ ($P\bar{6}m2$)	PBE	3.36	−0.54	3.90
	PBE+SOC	3.36	−0.51	3.87
TiI_2 ($P\bar{6}m2$)	PBE	4.06	0.39	3.67

Continued on next page

Table E.5 – continued from previous page

System	Functional	$V(\mathbf{r}_{vac.})$ (eV)	E_{Fermi} (eV)	Φ (eV)
	PBE+SOC	4.06	0.45	3.61
Co_2I_6 ($P\bar{3}1m$)	PBE	3.33	−2.12	5.45
	PBE+SOC	3.33	−1.81	5.14
Zr_2Cl_4 ($P2_1\|m$)	PBE	3.57	−0.99	4.56
	PBE+SOC	3.57	−0.99	4.56
$ZrCl_2$ ($P\bar{6}m2$)	PBE	3.65	−0.39	4.04
	PBE+SOC	3.65	−0.37	4.02
Zr_2Br_4 ($P2_1\|m$)	PBE	3.45	−0.89	4.34
	PBE+SOC	3.45	−0.89	4.34
$ZrBr_2$ ($P\bar{6}m2$)	PBE	3.54	−0.17	3.70
	PBE+SOC	3.53	−0.12	3.66
Zr_2I_4 ($P2_1\|m$)	PBE	4.10	−0.02	4.13
	PBE+SOC	4.10	0.00	4.10
ZrI_2 ($P\bar{6}m2$)	PBE	4.20	0.73	3.47
	PBE+SOC	4.20	0.80	3.40
Mo_2Cl_6 ($P\bar{6}2m$)	PBE	3.39	−1.70	5.10
	PBE+SOC	3.39	−1.66	5.05
Rh_2I_6 ($P\bar{3}1m$)	PBE	3.39	−2.20	5.58
	PBE+SOC	3.39	−1.99	5.37
Pd_4I_8 ($P2_1\|c$)	PBE	1.55	−4.32	5.86
	PBE+SOC	1.54	−4.23	5.78
Hf_2Cl_4 ($P2_1\|m$)	PBE	3.58	−0.90	4.49
	PBE+SOC	3.58	−0.91	4.49
$HfCl_2$ ($P\bar{6}m2$)	PBE	3.69	−0.04	3.72
	PBE+SOC	3.69	−0.02	3.70
Hf_2Br_4 ($P2_1\|m$)	PBE	3.47	−0.81	4.28
	PBE+SOC	3.47	−0.81	4.28

Continued on next page

Table E.5 – continued from previous page

System	Functional	$V(\mathbf{r}_{vac.})$ (eV)	E_{Fermi} (eV)	Φ (eV)
$HfBr_2$ ($P\bar{6}m2$)	PBE	3.58	0.17	3.41
	PBE+SOC	3.58	0.22	3.36
Hf_2I_4 ($P2_1\|m$)	PBE	4.16	0.13	4.02
	PBE+SOC	4.15	0.15	4.00
HfI_2 ($P\bar{6}m2$)	PBE	4.26	1.04	3.22
	PBE+SOC	4.26	1.15	3.11
W_2Cl_6 ($P\bar{3}1m$)	PBE	3.47	−1.63	5.10
	PBE+SOC	3.47	−1.43	4.90
W_2Cl_6 ($P\bar{6}2m$)	PBE	3.48	−1.23	4.71
	PBE+SOC	3.48	−1.08	4.55
HgI_2 ($P\bar{3}m1$-α)	PBE	3.20	−3.00	6.20
	PBE+SOC	3.19	−2.68	5.87
Hg_2I_2 ($P\bar{3}m1$-β)	PBE	3.83	−2.25	6.08
	PBE+SOC	3.82	−2.11	5.93

Appendix F

Complementary Details of Tight Binding Calculations

This appendix provides additional details on the Wannier interpolation. Table F.1 shows the fine energy interval, which was calculated to be 4 eV above ($E_{\text{frozen, max}}$) and below ($E_{\text{frozen, min}}$) the Fermi level. This table also presents the orbital states considered for the Wannier interpolation, determined from the density of states presented in section E, as well as the number of target Wannier functions (calculated considering table C.2) and the DFT functions used to calculate the overlap and hopping matrices. Figure F.1 shows the results of the interpolated band, compared to the PBE+SOC DFT band structures, ensuring the quality of the parameterized band structure and the corresponding tight-binding Hamiltonian (TB).

Table F.1: Summary of parameters used to perform the Wannier interpolation. Fine energy interval ($E_{frozen,min}$ and $E_{frozen,max}$), state considered in the halide (Orb. B) and metal (Orb. A), number of Wannier projections (N_{wann}) and number of DFT bands (N_{bands}).

System	$E_{\text{frozen, min.}}$ (eV)	$E_{\text{frozen, max.}}$ (eV)	Orb. B	Orb. A	N_{wann}	N_{bands}
Ti_2Cl_4 ($P2_1\|m$)	−5.22	2.78	s,p,d	s,p,d	108	120
$TiCl_2$ ($P\bar{6}m2$)	−4.73	3.27	s,p,d	s,p,d	54	66
$TiBr_2$ ($P\bar{6}m2$)	−4.51	3.49	s,p,d	s,p,d	54	66
TiI_2 ($P\bar{6}m2$)	−3.55	4.45	s,p,d	s,p,d	54	66

Continued on next page

Table F.1 – continued from previous page

System	$E_{\text{frozen, min}}$ (eV)	$E_{\text{frozen, max}}$ (eV)	Orb. B	Orb. A	N_{wann}	N_{bands}
Co_2I_6 ($P\bar{3}1m$)	−5.81	2.19	s,p,d	p,d	140	150
Zr_2Cl_4 ($P2_1\|m$)	−4.99	3.01	s,p,d	s,p,d	108	120
$ZrCl_2$ ($P\bar{6}m2$)	−4.37	3.63	s,p,d	s,p,d	54	66
Zr_2Br_4 ($P2_1\|m$)	−4.89	3.11	s,p,d	s,p,d	108	120
$ZrBr_2$ ($P\bar{6}m2$)	−4.12	3.88	s,p,d	s,p,d	54	66
Zr_2I_4 ($P2_1\|m$)	−4.00	4.00	s,p,d	s,p,d	108	120
ZrI_2 ($P\bar{6}m2$)	−3.20	4.80	s,p,d	s,p,d	54	66
Mo_2Cl_6 ($P\bar{6}2m$)	−5.66	2.34	s,p,d	p,d	140	150
Rh_2I_6 ($P\bar{3}1m$)	−5.99	2.01	s,p,d	s,p,d	144	156
Pd_4I_8 ($P2_1\|c$)	−8.23	−0.23	s,p,d	s,p,d	216	228
Hf_2Cl_4 ($P2_1\|m$)	−4.91	3.09	s,p,d	s,p,d	108	120
$HfCl_2$ ($P\bar{6}m2$)	−4.02	3.98	s,p,d	s,p,d	54	66
Hf_2Br_4 ($P2_1\|m$)	−4.81	3.19	s,p,d	s,p,d	108	120
$HfBr_2$ ($P\bar{6}m2$)	−3.78	4.22	s,p,d	s,p,d	54	66
Hf_2I_4 ($P2_1\|m$)	−3.85	4.15	s,p,d	s,p,d	108	120
HfI_2 ($P\bar{6}m2$)	−2.85	5.15	s,p,d	s,p,d	54	66
W_2Cl_6 ($P\bar{3}1m$)	−5.43	2.57	s,p,d	s,p,d,f	172	183
W_2Cl_6 ($P\bar{6}2m$)	−5.08	2.92	s,p,d	s,d	132	142
Hg_2I_2 ($P\bar{3}m1$)	−6.11	1.89	s,p,d	s,p,d	72	108
HgI_2 ($P\bar{3}m1$)	−6.68	1.32	s,p,d	s,p,d	54	68

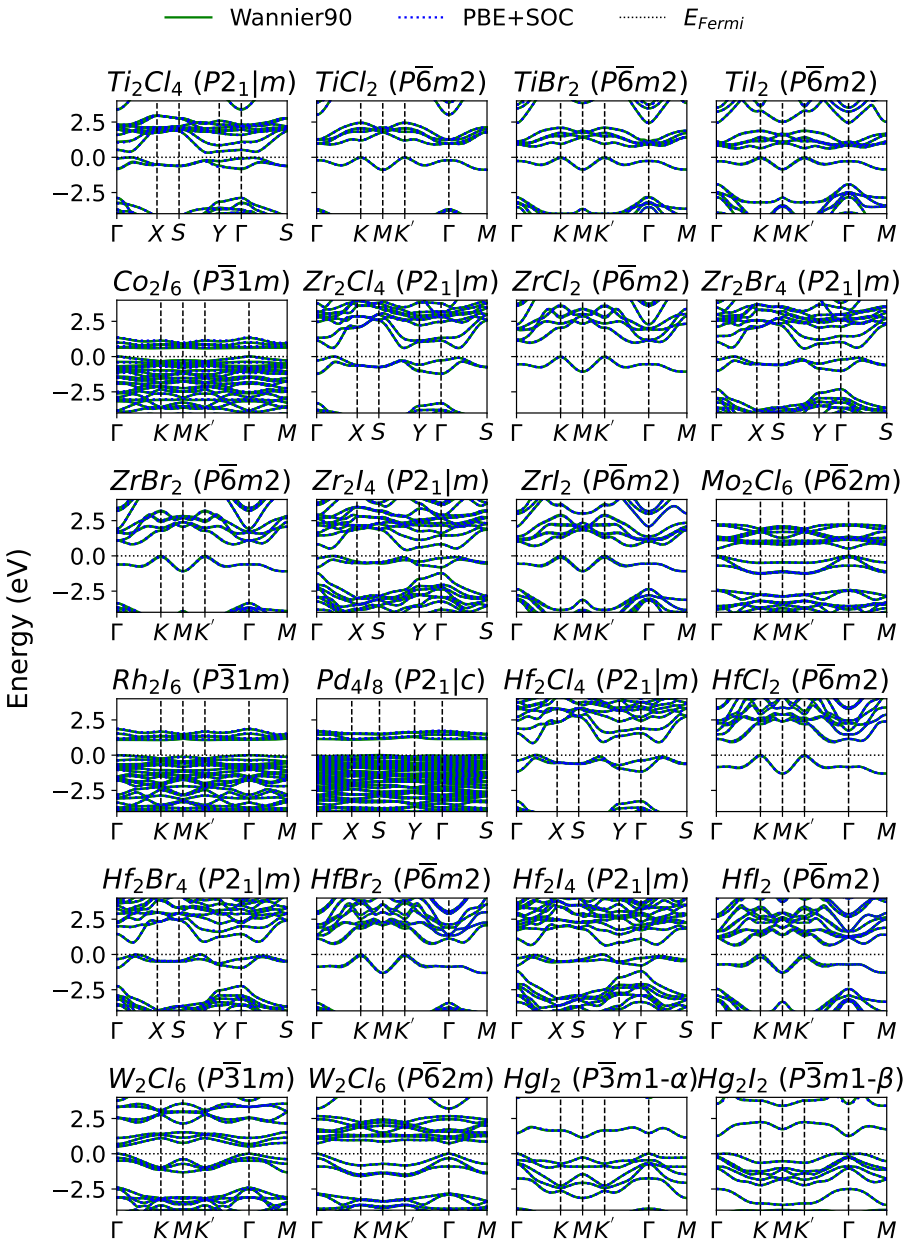

Figure F.1: Compassion between the interpolated Wannier (green dashed line) and PBE+SOC (blue solid line) band structures. In both the Fermi level was shifted to zero, as depicted by the black dotted line.

Appendix G

Complementary Details on Excitonic and Optical Properties

This appendix provides additional details on optical and excitonic properties. The main input parameters for the optical and excitonic calculations are presented in table G.1, where N_c (N_v) is the number of conduction (valence) bands considered determined as all bands in the limit below (above) the value δ_E, calculated as:

$$\delta_E \;=\; 4 \;-\; E_g^{\text{dir.}} \;.$$

Table G.2 presents numerical values describing the fundamental and bright excitonic states.

Table G.1: Main parameters used in optical and excitonic properties.

System	E_{Fermi} (eV)	χ (eV)	N_c	N_v
Ti_2Cl_4 ($P2_1\|m$)	−1.215 661	0.631 912	16	4
$TiCl_2$ ($P\bar{6}m2$)	−0.732 228	0.290 663	10	2
$TiBr_2$ ($P\bar{6}m2$)	−0.506 608	0.127 103	8	2
TiI_2 ($P\bar{6}m2$)	0.449 083	−0.042 635	12	4
Co_2I_6 ($P\bar{3}1m$)	−1.799 567	1.006 066	8	24
Zr_2Cl_4 ($P2_1\|m$)	−0.980 476	0.615 728	16	4
$ZrCl_2$ ($P\bar{6}m2$)	−0.371 960	0.607 743	8	2

Continued on next page

Table G.1 – continued from previous page

System	E_{Fermi} (eV)	χ (eV)	N_c	N_v
Zr_2Br_4 ($P2_1\|m$)	−0.877 769	0.573 006	16	4
$ZrBr_2$ ($P\bar{6}m2$)	−0.122 395	0.579 346	8	2
Zr_2I_4 ($P2_1\|m$)	−0.000 212	0.334 049	18	12
ZrI_2 ($P\bar{6}m2$)	0.801 903	0.344 732	10	2
Mo_2Cl_6 ($P\bar{6}2m$)	−1.647 362	0.128 032	14	10
Rh_2I_6 ($P\bar{3}1m$)	−1.976 262	0.924 157	8	24
Pd_4I_8 ($P2_1\|c$)	−4.214 038	0.971 300	8	42
Hf_2Cl_4 ($P2_1\|m$)	−0.868 948	0.638 656	10	4
$HfCl_2$ ($P\bar{6}m2$)	−0.006 799	0.658 829	6	2
Hf_2Br_4 ($P2_1\|m$)	−0.795 579	0.558 834	14	4
$HfBr_2$ ($P\bar{6}m2$)	0.232 020	0.595 437	8	2
Hf_2I_4 ($P2_1\|m$)	0.169 341	0.370 419	16	10
HfI_2 ($P\bar{6}m2$)	1.147 826	0.498 712	10	2
W_2Cl_6 ($P\bar{3}1m$)	−1.420 471	0.437 913	14	10
W_2Cl_6 ($P\bar{6}2m$)	−1.076 117	0.313 908	16	10
Hg_2I_2 ($P\bar{3}m1$)	−2.093 684	0.693 407	2	10
HgI_2 ($P\bar{3}m1$)	−2.666 591	0.821 306	2	6

Table G.2: Exciton ground state (E_X^{GS}), excitons binding energy (E_b), exction bright state (E_X^{br}) and, the type of fundamental excitonic state. The excitons binding energy was also shown for some system when the value is present in C2DB.

System	Source	E_X^{GS} (eV)	E_b (eV)	E_X^{br} (eV)	Type
Ti_2Cl_4 ($P2_1\|m$)	This work	0.25	0.78	0.40	Dark
	C2DB	-	-	-	-
$TiCl_2$ ($P\bar{6}m2$)	This work	0.65	0.81	0.65	Bright
	C2DB	-	0.83	-	-
$TiBr_2$ ($P\bar{6}m2$)	This work	0.34	0.73	0.34	Bright

Continued on next page

Table G.2 – continued from previous page

System	Source	E_X^{GS} (eV)	E_b (eV)	E_X^{br} (eV)	Type
	C2DB	-	0.59	-	-
TiI_2 ($P\bar{6}m2$)	This work	−1.07	1.68	0.03	EI
	C2DB	-	0.44	-	-
Co_2I_6 ($P\bar{3}1m$)	This work	0.90	0.73	0.90	Bright
	C2DB	-	-	-	-
Zr_2Cl_4 ($P2_1\|m$)	This work	0.67	0.55	0.67	Bright
	C2DB	-	-	-	-
$ZrCl_2$ ($P\bar{6}m2$)	This work	1.43	0.74	1.43	Bright
	C2DB	-	0.91	-	-
Zr_2Br_4 ($P2_1\|m$)	This work	0.63	0.59	0.63	Bright
	C2DB	-	-	-	-
$ZrBr_2$ ($P\bar{6}m2$)	This work	1.30	0.75	1.30	Bright
	C2DB	-	0.83	-	-
Zr_2I_4 ($P2_1\|m$)	This work	0.30	0.58	0.30	Bright
	C2DB	-	-	-	-
ZrI_2 ($P\bar{6}m2$)	This work	0.96	0.68	0.96	Bright
	C2DB	-	0.64	-	-
Mo_2Cl_6 ($P\bar{6}2m$)	This work	0.36	0.29	0.36	Bright
	C2DB	-	-	-	-
Rh_2I_6 ($P\bar{3}1m$)	This work	1.26	0.74	1.26	Bright
	C2DB	-	-	-	-
Pd_4I_8 ($P2_1\|c$)	This work	1.62	0.47	1.62	Bright
	C2DB	-	-	-	-
Hf_2Cl_4 ($P2_1\|m$)	This work	1.05	0.45	1.05	Bright
	C2DB	-	-	-	-
$HfCl_2$ ($P\bar{6}m2$)	This work	1.67	0.73	1.67	Bright
	C2DB	-	0.91	-	-

Continued on next page

Table G.2 – continued from previous page

System	Source	E_X^{GS} (eV)	E_b (eV)	E_X^{br} (eV)	Type
Hf_2Br_4 ($P2_1\|m$)	This work	0.92	0.52	0.92	Bright
	C2DB	-	-	-	-
$HfBr_2$ ($P\bar{6}m2$)	This work	1.44	0.71	1.44	Bright
	C2DB	-	0.81	-	-
Hf_2I_4 ($P2_1\|m$)	This work	0.53	0.51	0.53	Bright
	C2DB	-	-	-	-
HfI_2 ($P\bar{6}m2$)	This work	1.19	0.64	1.19	Bright
	C2DB	-	0.57	-	-
W_2Cl_6 ($P\bar{3}1m$)	This work	0.59	0.36	0.59	Bright
	C2DB	-	-	-	-
W_2Cl_6 ($P\bar{6}2m$)	This work	0.84	0.23	0.84	Bright
	C2DB	-	-	-	-
HgI_2 ($P\bar{3}m1$-α)	This work	1.59	0.65	1.59	Bright
	C2DB	-	0.98	-	-
Hg_2I_2 ($P\bar{3}m1$-β)	This work	1.69	0.28	1.69	Bright
	C2DB	-	-	-	-